

## Abstract

JANG, WONHOON. Modeling asymmetric distortion in multichannel radio frequency communication systems. (Under the direction of Dr. Michael B. Steer).

A multi-slice behavioral model is used to capture baseband memory effects in multichannel communication circuits and systems. The model is composed of two slices. Each slice includes a static nonlinear function box and linear filters. The first slice captures short-term memory effects and the second slice captures baseband memory effects. A robust extraction procedure for the model is developed with a physically realistic baseband slice. An efficient measurement method for the extraction is used. A 2.4 GHz power amplifier is modeled as an example. The performance of the extracted model is verified by showing that it captures baseband effects when the power amplifier is excited with a two-channel WCDMA signal. One of the advantages of the model is that it can be used in various established simulation schemes such as envelope transient simulation and transient (time-marching or SPICE-like) simulation. The model is shown to be compatible with both. In the transient simulation, the model supports the use of a much lower carrier frequency. This results in enhanced computational efficiency and the same results are achieved. This opens up a new contribution for RF system simulation where complex signals comprise of signals that can be of general form including signals that cannot be represented as modulated carriers. While envelope transient simulation is restricted to slowly modulated carriers, there is no restriction on the type of drive signal so that single tone, multi-tone, CDMA, chirp and noise signals can be combined.

**Modeling asymmetric distortion in multichannel radio frequency  
communication systems**

by

**Wonhoon Jang**

A dissertation submitted to the Graduate Faculty of  
North Carolina State University  
in partial fulfillment of the  
requirements for the Degree of  
Doctor of Philosophy

**Electrical Engineering**

Raleigh

2006

**Approved By:**

---

Dr. Griff L. Bilbro

---

Dr. W. Rhett Davis

---

Dr. Michael B. Steer  
Chair of Advisory Committee

---

Dr. Douglas W. Barlage

This dissertation is dedicated to my son, Inyoung A. Jang, and my wife, Eunjung Park, and also to my parents in Korea . . .

## Biography

Wonhoon Jang received the B.S. degree in electronics from Kyungpook National University in Daegu, Korea, in 1997. He is presently working toward Ph.D. degree in electrical engineering at North Carolina State University in Raleigh. From 1997 to 1999, he was with LG Precision Co., Kumi, Korea, where he was involved with military radios. His current research interests include nonlinear RF/microwave system analysis and modeling.

## Acknowledgements

I would like to thank Dr. Michael B. Steer for serving as my academic advisor and supporting me during my study. His great help made it possible for me to come this far. I also like to thank Dr. Griff L. Bilbro, Dr. W. Rhett Davis and Dr. Douglas W. Barlage for serving on my committee and would like to thank Dr. Jon-Paul Maria for serving as a graduate representative. Many thanks go to Dr. Kevin Gard, to Dr. Steer's present and past graduate students, Aaron Walker, Frank Heart, Jayesh Nath, Mark Buff, Nikhil Kriplani, Ramya Mohan, Sonali Luniya, and to Dr. Wael Fathelbab for sharing valuable talks and fun. Special thanks go to Stephen Bruss for sharing his harmonic balance codes in MATLAB at [www.uaf.edu/asgp/spbruss/other/em](http://www.uaf.edu/asgp/spbruss/other/em). I extensively used his code in my envelope transient codes attached in Appendix A.

# Contents

<b>List of Figures</b>	<b>vii</b>
<b>List of Tables</b>	<b>xi</b>
<b>1 Introduction</b>	<b>1</b>
1.1 Motivation . . . . .	1
1.2 Structure of Dissertation . . . . .	3
1.3 Statement of Originality . . . . .	3
1.4 Publications . . . . .	4
<b>2 Nonlinear Modeling of RF System</b>	<b>5</b>
2.1 Introduction . . . . .	5
2.2 Nonlinearities with Memory Effects . . . . .	6
2.2.1 Nonlinear RF Effects . . . . .	10
2.2.2 Nonlinear Baseband Effects . . . . .	13
2.3 Behavioral Modeling . . . . .	20
2.3.1 Memoryless Nonlinear Model . . . . .	22
2.3.2 Memory Polynomial Model . . . . .	24
2.3.3 Wiener-Hammerstein (3 box) Model . . . . .	30
2.4 Simulating RF models . . . . .	35
2.4.1 Transient Analysis . . . . .	35
2.4.2 Harmonic Balance Analysis . . . . .	36
2.4.3 Conventional Envelope Transient Analysis . . . . .	37
2.5 Summary . . . . .	42
<b>3 Multi-Slice Behavioral Model</b>	<b>44</b>
3.1 Introduction . . . . .	44
3.2 Model Architecture . . . . .	45
3.3 Extraction Procedure . . . . .	46
3.4 Verification . . . . .	47

3.5	Summary . . . . .	56
<b>4</b>	<b>Multichannel Envelope Transient Analysis</b>	<b>57</b>
4.1	Introduction . . . . .	57
4.2	Theoretical Formulation . . . . .	58
4.3	Formulation for Circuit Simulation . . . . .	60
4.4	Baseband Effects . . . . .	63
4.5	Harmonic Balance vs. Envelope Transient . . . . .	64
4.6	Single vs. Multi Envelope Transient . . . . .	68
4.7	Summary . . . . .	69
<b>5</b>	<b>Multichannel Communication Systems</b>	<b>71</b>
5.1	Introduction . . . . .	71
5.2	Modeling of a Power Amplifier Using a Multi-Slice Behavioral Model	72
5.3	Enhanced Envelope Transient Simulation in MATLAB . . . . .	91
5.4	Multichannel Envelope Transient Simulation Using a Multi-Slice Model	94
5.5	Time-Marching Simulation Using a Multi-Slice Model . . . . .	97
5.6	Summary . . . . .	103
<b>6</b>	<b>Conclusion and Future Work</b>	<b>105</b>
6.1	Conclusion and Discussion . . . . .	105
6.2	Suggestions for Future Work . . . . .	108
	<b>Bibliography</b>	<b>110</b>
<b>A</b>	<b>MATLAB Code of Multichannel Envelope Transient</b>	<b>118</b>
<b>B</b>	<b>Power Amplifier Circuits Used in Section 4.5</b>	<b>134</b>

# List of Figures

2.1	Typical frequency-dependent responses of an RF system: (a) AM-AM responses; (b) AM-PM responses. . . . .	8
2.2	Typical asymmetric spectral regrowth of a digitally modulated signal . . . . .	9
2.3	Frequency-dependent small-signal gain and saturated gain . . . . .	11
2.4	Frequency spectra: (a) a single-tone input swept in frequency and amplitude; and (b) the corresponding output. . . . .	12
2.5	Structure of the model being able to capture baseband effects. . . . .	14
2.6	Demonstration of the asymmetry mechanism based on (2.4) and (2.5). . . . .	15
2.7	Frequency spectra of (a) a two tone input swept in frequency and amplitude, and (b) the corresponding output. . . . .	18
2.8	Frequency spectra of (a) a digitally-modulated signal swept in amplitude, and (b) the corresponding output. . . . .	19
2.9	Structure of bandpass-type behavioral model . . . . .	21
2.10	Structure of the memory polynomial model . . . . .	25
2.11	System identification of the memory polynomial model . . . . .	27
2.12	Sequential implementation of the memory polynomial model . . . . .	28
2.13	Structure of the Wiener-Hammerstein model . . . . .	30
2.14	AM-PM responses of the Wiener-Hammerstein model . . . . .	32
2.15	AM-AM responses of the Wiener-Hammerstein model . . . . .	34
2.16	Partition of a circuit in harmonic balance . . . . .	36
2.17	Frequency domain representations of a single-channel digitally-modulated signal: (a) its spectrum; (b) its representation as a phasor with amplitude and phase varying slowly in time; (c) envelope signal; (d) the phasor presentation of the envelope; and (e) its windowed spectrum of the modulated RF signal in (a). . . . .	40
2.18	(a) spectrum of the electrical variable; (b) its transfer function; (c) down-converted spectrum and (d) down-converted transfer function. . . . .	41
3.1	A two-slice nonlinear system behavioral model. . . . .	45

3.2	A block diagram showing extraction procedure of the two-slice nonlinear system behavioral model. . . . .	47
3.3	Measured and modelled AM-AM characteristics of the amplifier at 2.5 GHz. (The measured and modelled characteristics overlap.) . . .	48
3.4	Measured and modelled AM-PM characteristics of the amplifier at 2.5 GHz. (The measured and modelled characteristics overlap.) . . .	49
3.5	Normalized magnitude of $H(f)$ which is used directly in the model. .	50
3.6	Modelled phase characteristics of $H(f)$ which is used directly in the model. . . . .	50
3.7	Measured and modelled output frequency spectra of the WLAN amplifier. . . . .	51
3.8	Error computed between measured and modelled spectral regrowth.	52
3.9	Expansion of Figure 3.7 with clearer depiction of spectral regrowth asymmetry and comparison of the modeled and measured results. . .	52
3.10	Asymmetries of measured and modelled spectral regrowth. . . . .	53
3.11	Real part of the modelled and measured output complex envelopes in the time domain. . . . .	54
3.12	Imaginary part of the modelled and measured output complex envelopes in the time domain. . . . .	54
3.13	Output frequency spectra of the model with and without memory, and measurements. . . . .	55
4.1	Input and output of a nonlinear system in the complex envelope expression view: (a) time-varying input signal; and (b) time-varying internal and output signals. . . . .	59
4.2	Spectrum of signals in a nonlinear system considered in MET analysis: (a) spectra of source signals; and (b) spectra of internal circuit and output signals. . . . .	61
4.3	Input and output spectra of the PCS amplifier with an IS-95 signal modelled using the time-varying HB and ET method. Center frequency is 1.9 GHz. (The output spectra of the time-varying HB and ET overlap.) . . . . .	65
4.4	Magnitude differences between lower and upper IM3 products of the PCS amplifier with two tones separated by 200 KHz. . . . .	66
4.5	Input and output spectra of the modified PCS amplifier with an IS-95 signal modelled using the time-varying HB and ET method. Center frequency is 1.9 GHz. . . . .	66
4.6	Expansion of Figure 4.5 with clearer depiction of spectral regrowth asymmetry. . . . .	67
4.7	Magnitude differences between lower and upper IM3 products of the modified PCS amplifier with two tones separated by 200 KHz. . . .	67

4.8	Normalized simulation time of SET and MET with respect to channel separation. . . . .	68
5.1	A two-slice nonlinear system behavioral model for multichannel applications. . . . .	72
5.2	A block diagram of the extraction for the linear filters in the first slice. . . . .	74
5.3	A block diagram of the extraction for: (a) the complex gain block; and (b) the baseband filter in the second slice. . . . .	76
5.4	Measured and modeled (a) AM to AM response; and (b) AM to PM response of the amplifier at 2.4 GHz. . . . .	79
5.5	Modeled (a) magnitude response; and (b) phase response of H1 and H2. . . . .	80
5.6	(a) Measured AM-AM responses; and (b) modeled AM-AM responses over the operating frequency band. . . . .	81
5.7	(a) Measured AM-PM responses; and (b) modeled AM-PM responses over the operating frequency band. . . . .	82
5.8	(a) The amplitude response; and (b) The phase response of the baseband $K(f)$ . . . . .	83
5.9	Measured and modeled magnitude of $\Delta\text{IM3}$ as a function of frequency separation. . . . .	84
5.10	Measured output of a two-channel WCDMA signal and modeled output without the filter $M(f)$ . . . . .	85
5.11	Modeled phase response of H1 and H2. . . . .	86
5.12	(a) The modeled amplitude responses with and without baseband effects to a single-channel WCDMA; and (b) the modeled response with baseband effects compared with the measurement. . . . .	87
5.13	(a) The modeled phase responses with and without baseband effects to a single-channel WCDMA; and (b) the modeled response with baseband effects compared with the measurement. . . . .	89
5.14	(a) The modeled amplitude responses with and without baseband effects to a two-channel WCDMA; and (b) the modeled response with baseband effects compared with the measurement. . . . .	90
5.15	The circuit model of the amplifier. . . . .	91
5.16	The circuit divided into the linear and nonlinear sub-circuits. . . . .	91
5.17	The flow chart of the multichannel envelope transient simulations. . . . .	93
5.18	The results of the multichannel envelope transient simulations. . . . .	94
5.19	The baseband circuit for the multichannel envelope transient simulations. . . . .	95
5.20	Measured and modeled IM3 asymmetries. . . . .	95
5.21	(a) The modeled amplitude responses with and without baseband effects to a two-channel WCDMA; and (b) the modeled response with baseband effects compared with the measurement. . . . .	96

5.22	Generation of a WCDMA input signal with 20 MHz of the carrier frequency. . . . .	98
5.23	A frequency spectrum of the linearly interpolated input signal. . . . .	99
5.24	Multi-slice behavioral model in transient simulation. . . . .	99
5.25	A SPICE model for computation of a complex coefficient $a$ . . . . .	100
5.26	Input and output frequency spectra of the multi-slice model. . . . .	101
5.27	Measured and modeled output frequency spectrum. . . . .	102
5.28	A part of the modeled and measured time-domain signal. . . . .	103
B.1	The circuit of the PCS power amplifier from ADS. . . . .	135
B.2	The same circuit as in B.1 with modified parameters of the bias circuit elements. . . . .	136

## List of Tables

2.1	The angles in Figure 2.6 . . . . .	16
2.2	The vectors in Figure 2.6 . . . . .	16
3.1	Discrepancies (in dB) between the measured and modeled spectral regrowth. . . . .	55
5.1	The extracted values of the complex gain $g$ . . . . .	78
5.2	The extracted poles and zeros of the baseband filter $K(f)$ . . . . .	84
5.3	Discrepancies (in dB) between the measured and modeled spectral regrowth without the filter $M(f)$ . . . . .	85
5.4	Discrepancies (in dB) between the measured and modeled spectral regrowth. . . . .	86
5.5	Discrepancies between the measured and modeled phase. . . . .	88
5.6	Discrepancies (in dB) between the measured and modeled (without baseband effects) spectral regrowth. . . . .	88
5.7	Discrepancies (in dB) between the measured and modeled (with baseband effects) spectral regrowth. . . . .	88
5.8	Discrepancies (in dB) between the measured and modeled (without baseband effects) spectral regrowth. . . . .	97
5.9	Discrepancies (in dB) between the measured and modeled (with baseband effects) spectral regrowth. . . . .	97
5.10	Discrepancies (in dB) between the measured and modeled spectral regrowth. . . . .	101

# Chapter 1

## Introduction

### 1.1 Motivation

In narrowband and single-channel RF systems, memory effects are small and can be ignored. However it becomes more important to model memory effects as signal bandwidths increase as in recent RF systems such as wideband and/or multichannel RF systems because increases of memory effects degrade linearization or performance of communication systems. Memory effects can be partitioned into short-term and long-term memory effects. Short-term memory effects are relatively easy to model but long-term memory effects (or baseband effects) are more challenging. Thus capturing baseband effects becomes an issue in RF system modeling. These effects are up-converted from the baseband to the fundamental frequency band and contribute to distortion at the output. The contribution can be observed in the form of asymmetric spectral regrowth. In multichannel RF system modeling, baseband effects are more complex to model due to cross-modulation of the channels [1] and the relatively wide range of low frequency components generated.

There are two concerns on modeling baseband effects. First, we need to have accurate models as a basic requirement of simulation. Depending on accuracy re-

quirement, we can choose circuit-level or system-level models (or behavioral models). Second, due to long time constants of baseband effects, we must simulate an RF system for a relatively long time interval so computational efficiency becomes an issue. If we use circuit-level models and use time-marching simulation, this demands a lot of computational resources. To circumvent this kind of problem, envelope-following and envelope transient analysis have been developed. Envelope-following reduces computational demands by skipping many periods of the RF carrier since the envelope changes relatively slowly; however this analysis is not suitable for multichannel applications when sum of the RF carriers is no longer periodic [2]–[4]. On the other hand, envelope transient can be extended easily for multichannel applications but there is an ambiguity in capturing baseband effects in the previously reported methods [5]–[10]. An alternative to circuit-level modeling is to model baseband effects by using behavioral models. Now an issue is not computational efficiency but how to establish accurate models to capture baseband effects. Usually behavioral models of RF systems are extracted from measurements. Since it is not possible to measure baseband effects directly, a method must be developed to indirectly measure the effects and then to use the measurements to extract parameters of a model. This is the first time that a behavioral model is reported to systemically capture baseband effects.

In this dissertation, a multi-slice behavioral model [11] is used to model baseband effects in multichannel RF systems. As an example, asymmetric spectral regrowth in a multichannel amplifier is modeled accurately by using a baseband filter in a multi-slice model. Newly developed are a measurement method and an extraction method to accurately generate baseband parameters of the model. Also in this dissertation, an implementation scheme of a multichannel envelope transient (MET) analysis suitable for modeling distortion in an RF circuit excited with a multichannel digitally-modulated signal is developed. This analysis can model arbitrary baseband effects by using the constituent equations of the linear resistor, inductor and capacitor. This clarifies the ambiguity of capturing baseband effects that has previously been reported [5]–[10]. By comparing envelope transient and harmonic balance analyses, the mechanism of capturing baseband effects is explained. Finally it is demonstrated that multi-slice models can be used in other established circuit analyses such as envelope

transient and transient (time-marching or SPICE-like) simulation. After synthesizing a baseband circuit of the extracted multi-slice model, the modified model is used in multichannel envelope transient simulation and also in transient simulation. In transient simulation a significant decrease in the carrier frequency of the drive signal makes it possible to use the model in the time domain while resulting in the same results. Since the model can be used in the time domain, it can handle virtually any excitations including noise. This provides a new concept in RF system simulation.

## 1.2 Structure of Dissertation

This dissertation consists of six chapters. All chapters except Chapter 1 and Chapter 6 include an introduction section and a summary section. Chapter 1 is an introduction and Chapter 6 includes a conclusion. In Chapter 2 introductory subjects are discussed. Some of the sections are reviews of literatures and some establish the basis for later chapters. Chapter 3 to Chapter 5 discuss main subjects: multi-slice behavioral modeling; multichannel envelope transient analysis; and applications of a multi-slice model. Appendix A includes the MATLAB codes developed to implement multichannel envelope transient analysis of an amplifier circuit.

## 1.3 Statement of Originality

Section 2.2 establishes the new approach to multi-slice behavioral modeling. Section 2.3 and Section 2.4 include critical reviews. In Section 3.2, the basic structure of the multi-slice model was adapted from [11]. The extraction and application of the model with a digitally-modulated signal are original contributions in Section 3.3 and Section 3.4. Section 4.2 was independently developed from the single-channel envelope transient analysis originally presented in [6]–[8]. Theoretical clarification of the modeling of general baseband effects presented in other sections of Chapter 4 is an original contribution. Extension of the model to multichannel applications in

Section 5.2; implementation of the multichannel envelope transient in Section 5.3; application of the multichannel envelope transient to a baseband circuit in Section 5.4; and application of transient simulation to a multi-slice model in Section 5.5 are original contributions.

## 1.4 Publications

Three journal and one conference papers have been accepted for publication.

1. W. Jang, A. Walker, K. Gard and M. Steer, “Capturing asymmetrical spectral regrowth in RF systems using a multi-slice behavioral model and enhanced envelope transient analysis,” *Int. J. RF Microwave CAE*, In press.
2. N. Carvalho, J. Pedro, W. Jang and M. Steer, “Nonlinear RF circuit and systems simulation when driven by several modulated signals,” *IEEE Trans. Microwave Theory Techn.*, Vol. 54, No. 2, Feb. 2006, pp. 572–579.
3. N. Carvalho, J. Pedro, W. Jang and M. Steer, “Nonlinear simulation of mixers for assessing system-level performance,” *Int. J. RF Microwave CAE*, Vol. 15, No. 4, July 2005. pp. 350–361.
4. N. Carvalho, J. Pedro, W. Jang and M. Steer, “Simulation of nonlinear RF circuits driven by multi-carrier modulated signals,” in *IEEE MTT-S Int. Microwave Symp. Dig.*, June 2005, pp. 801–804.

## Chapter 2

# Nonlinear Modeling of RF System

### 2.1 Introduction

The ultimate goal of nonlinear RF system modeling is to accurately and efficiently capture distortion as well as the desired responses at the output of the system. Causes of distortions include nonlinearities and memory effects, which are essential features to be captured in modern nonlinear RF system modeling. When the excitation of a nonlinear RF system is a narrowband signal, nonlinearities are the main causes of distortion and memory effects do not contribute much to distortion. However, memory effects play a more significant role as the excitation bandwidth increases. This is common in recent wireless communications. In Section 2.2, nonlinearities with memory effects are reviewed in the perspective of what is nonlinear memory effects and how to measure them. Also, introduced is a new classification of memory effects for the purpose of behavioral modeling strategy.

Section 2.3 reviews various behavioral models: a memoryless model; a memory polynomial model; and the Wiener-Hammerstein model. These models are analyzed in the perspective of model structure and functionality related to capturing RF responses and baseband memory effects. Also, included in this section is a discussion

of how to extract the models from measurements.

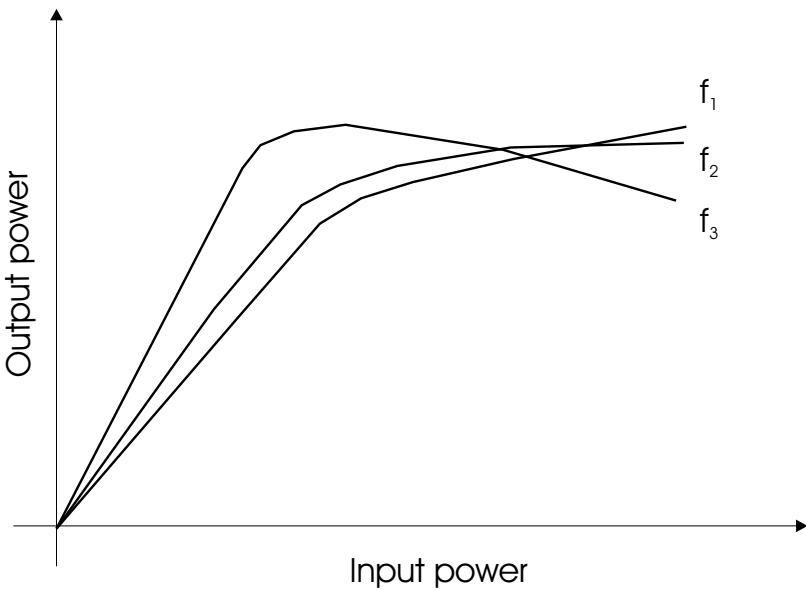
When a digitally-modulated signal is used as an input to a nonlinear RF system with memory, significant contributions to distortion at the output of the system are made by memory effects, especially baseband memory effects. In RF system simulation, system-level models or behavioral models are usually idealized too much to accurately account for baseband memory effects so they are subject to poor accuracy compared to circuit-level models. At the circuit level, Envelope Transient (ET) [5]–[10] analysis can be used to simulate RF circuits excited by digitally-modulated signals and captures baseband memory effects. In contrast time-marching simulation (TMS) (SPICE-like analysis) discussed in Subsection 2.4.1 cannot simulate RF circuits excited by digitally-modulated signals and Harmonic Balance (HB) [12, 13] analysis discussed in Subsection 2.4.2 cannot capture the relatively slow baseband effects. Although ET is not suitable for simulation of a whole system represented with circuit-level models due to great computational demands, it can be used for parts of the system whose accuracy is a critical factor of the simulation. In Subsection 2.4.3, the conventional ET analysis is reviewed. The most popular circuit and system simulation method is to use a time-marching scheme implemented as a SPICE-like analysis for circuits or in a MATLAB-like simulator for systems. However time-marching schemes are considered to be too slow to simulate the very large number of time steps required to capture both memory effects and RF signals.

## 2.2 Nonlinearities with Memory Effects

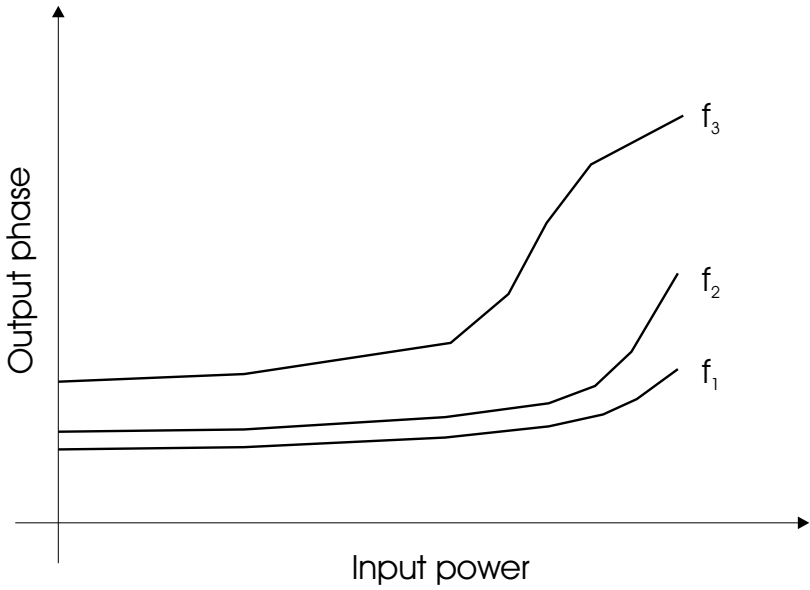
When the input of a nonlinear RF system is a narrowband signal, nonlinearities of the system are the major concerns in modeling. In the case of a sinusoidal input, nonlinearities of the system generate harmonic frequency components at the output of the system and, at the same time, these components affect the fundamental frequency component by the mechanism of frequency conversion. The harmonic components are significantly reduced by bandpass-filtering at the output of the system so these are not of interest; however, the distortions mixed back on to the fundamental components

appear as gain compression or expansion and are of great interest in modeling since they cannot be filtered out. This kind of distortion is observed as input amplitude to output amplitude modulation (AM-AM) and input amplitude to output phase modulation (AM-PM).

A nonlinear RF system exhibits significant frequency-dependent characteristics or memory effects. This can be observed when the input of the system is a wideband signal such as a multi-tone signal or a digitally-modulated signal. When a multi-tone signal is applied to the system, memory effects are observed as frequency dependent AM-AM and AM-PM responses as typically shown in Figure 2.1. The AM-AM and AM-PM responses in Figure 2.1 suggest that a static nonlinear function cannot account for the frequency dependency of the responses so there are memory effects. When a digitally-modulated signal such as WCDMA or OFDM is applied to the RF system, asymmetric spectral regrowth is observed at the output of the system. Spectral regrowth at one side of the channel is higher than at the other side as shown in Figure 2.2. This asymmetrical phenomenon is caused by memory effects. Memory effects are not simply frequency-dependent characteristics themselves of an RF system but appear as pass-band distortions produced not only by frequency-dependent characteristics at the pass-band of the system but also by frequency components that are affected by frequency-dependent characteristics at other frequency bands such as baseband and harmonic bands and then up- or down-converted in frequency to the pass-band by nonlinearities. Hence, memory effects of an RF system imply nonlinear memory effects. By the way, baseband is a frequency band arranging from DC to a relatively low frequency that is relatively close to DC and its frequency products generated by even-order nonlinearities contribute to distortion at the fundamental frequency band when being up-converted by odd-order nonlinearities of an RF system. Why are we concerned about memory effects? As frequency bandwidths of input signals increase in modern communication systems, memory effects become a significant contribution to distortion. Thus behavioral models must account for these effects for accurate simulations. Also, memory effects must be modeled in order to design sophisticated pre-distorters because these effects make static pre-distorters ineffective.



(a)



(b)

Figure 2.1: Typical frequency-dependent responses of an RF system: (a) AM-AM responses; (b) AM-PM responses.

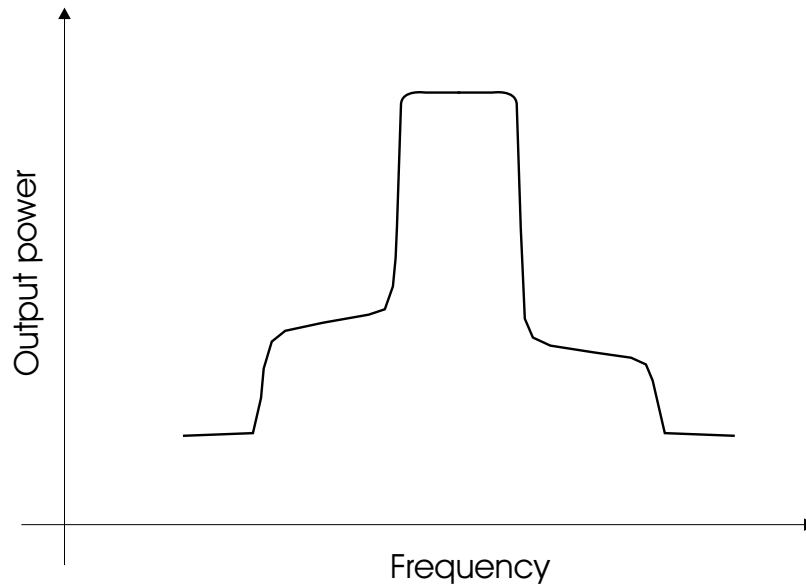


Figure 2.2: Typical asymmetric spectral regrowth of a digitally modulated signal

The physical causes of memory effects can be divided into electrical and thermal memory effects. Electrical memory effects are caused by frequency-dependent characteristics of reactive components in bias and matching circuits forming feedback loops with active devices. Meanwhile thermal memory effects are mainly attributed to temperature changes from heat generated by collisions of electrons to lattices inside active devices. If we consider memory effects in the time domain, outputs of RF systems are not only dependent on instantaneous inputs but also on previous inputs. In terms of memory duration, memory effects are generally classified into short-term and long-term memory effects. Thermal memory has relatively long-time constants since temperature changes are very slow compared to a period of an RF signal, while electrical memory has both short- and long-time constants since frequency-dependent characteristics of reactive components change over the entire frequency domain from DC to infinity. In this dissertation, only electrical memory effects are considered; however, the work could be extended to handle thermal effects. Short-term memory effects are attributed to characteristics of a system at radio frequencies so they affect output distortion in almost immediate response to the RF signal, while long-term

memory effects are attributed to baseband characteristics of a system so they affect output relatively for a long time, say milli-seconds.

In nonlinear RF system modeling, memory effects of an RF system are usually captured by measurements. Unfortunately, distortions caused by memory effects cannot be bandpass-filtered at the output of the system and neither can be measured directly since the phenomenon that causes memory effects usually isolated from the external ports by filters and other frequency-selective circuits. If memory effects could be filtered out, then we would not need to model the effects, and if they could be probed directly, then it would be very easy to model these effects. Since it is difficult to model or quantify memory effects of an RF system so a modeling strategy should be established in conjunction with convenient measurement methods. The first step of the strategy used in this dissertation is that memory effects are divided for modeling purposes into two categories: nonlinear RF effects and nonlinear baseband effects. These categories are considered separately in the following subsections. The classification is done according to principle modeling considerations: what needs to be captured (which determines model structure); and what can be measured (which determines model extraction). Nonlinear RF effects and nonlinear baseband effects are mainly caused by nonlinearities with short-term and long-term memory respectively. These new terms are used to indicate that there is a subtle difference such that both nonlinear RF and baseband effects include distortions caused by DC characteristics of an RF system due to measurement limitation. This is elaborated on in the following subsections.

### **2.2.1 Nonlinear RF Effects**

If we assume that the maximum order of nonlinearity of a nonlinear RF system is limited, discrete and finite frequency bands of the RF system such as the baseband, pass-band and harmonic bands are used when a band-limited input is applied to the RF system. For example, if an input with a modulation bandwidth of 10 MHz at the carrier frequency of 2 GHz is applied to an RF system with up to third-order nonlinearities, the frequency bands of the system involved are from DC to 10 MHz,

from 1.985 GHz to 2.015 GHz, from 3.99 GHz to 4.01 GHz, and from 5.985 GHz to 6.015 GHz. System characteristics at all the used frequency bands are involved in memory effects observed in the pass-band around the carrier frequency. Among the various memory effects, nonlinear RF effects are confined to the memory effects that are attributed to pass-band and harmonic-band characteristics of an RF system. These effects can be observed if we compare frequency-dependent small-signal and saturated gain responses of a power amplifier as typically shown in Figure 2.3. If the

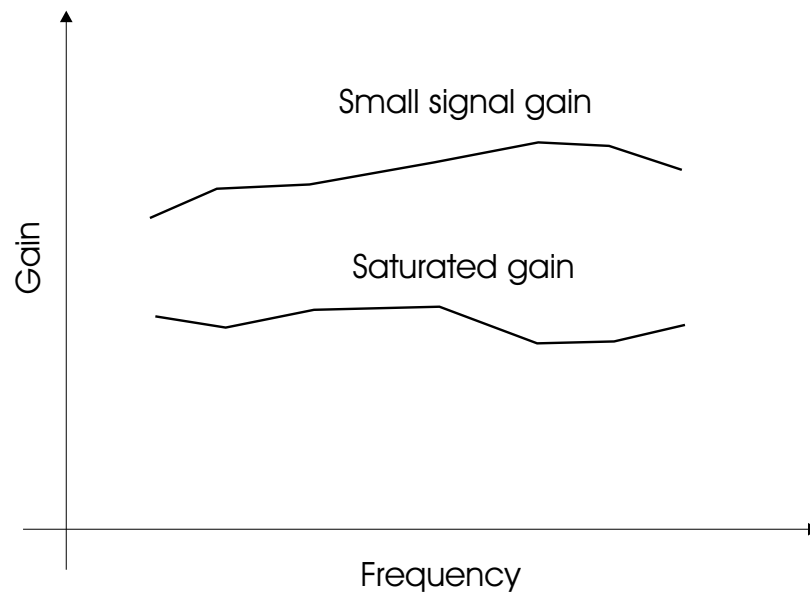


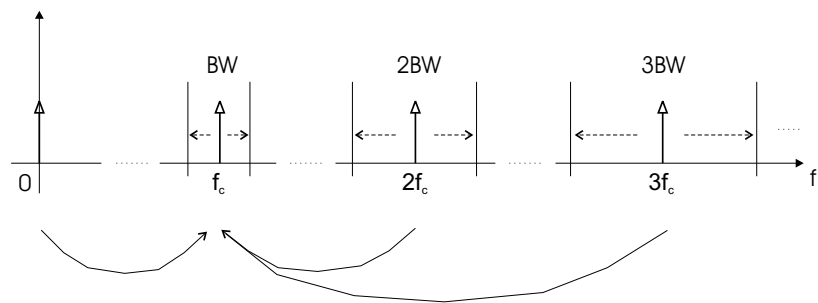
Figure 2.3: Frequency-dependent small-signal gain and saturated gain

amplifier did not exhibit nonlinear RF effects, the saturated gain response would be a vertically displaced version of the small-signal gain response.

Nonlinear RF effects cannot be quantified by direct measurements so they should be extracted from measurements with inputs that produce outputs that include these effects. Such measurements can be obtained from single-tone tests. As shown in Figure 2.4(a), a single-tone input is swept in two dimensions; frequency and amplitude while  $S_{21}$  data are collected by a network analyzer. The  $S_{21}$  data are converted to amplitude and phase responses of an RF system at the carrier frequencies. The results are AM-AM and AM-PM responses over an operating frequency band. These



(a)



(b)

Figure 2.4: Frequency spectra: (a) a single-tone input swept in frequency and amplitude; and (b) the corresponding output.

responses exclude baseband memory effects because no component exists in the baseband as shown in Figure 2.4(b). Note that responses include memory information at DC as well as at the RF bands. Since the DC memory information cannot be separated from these measurements, it should be post-processed when a behavioral model is constructed. Excluding baseband memory effects, nonlinear RF effects are the same as electrical short-term memory effects. In most RF behavioral models AM-AM and AM-PM responses at the reference frequency, usually chosen to be the center frequency of the pass-band, is modeled as a static nonlinear function. Then the residual AM-AM and AM-PM responses at other frequencies are modelled based on the static nonlinear function. Nonlinear RF effects cause the AM-AM and AM-PM responses at frequencies other than the reference frequency to deviate from the reference AM-AM and AM-PM response. Modeling the deviations is achieved by cascading linear filters to the reference static nonlinear function. The input and output linear filters function as a pre-distorter and a post-distorter respectively. An application of modeling nonlinear RF effects to a real power amplifier is in Section 5.3.

A typical wideband single-channel digitally-modulated signal such as WCDMA has a modulation bandwidth of around 5 MHz. Compared to the carrier frequency that normally is of the order of one or two gigahertz, the modulation bandwidth is relatively narrow. Hence, frequency-dependent nonlinear RF effects are likely to be significantly small. However, in a multichannel case where a nonlinear system is used to amplify signals widely separated in frequency (eg. two WCDMA channels with frequency separation of 100 MHz) frequency-dependent nonlinear RF effects are likely to be significant. Thus, frequency-dependent nonlinear RF effects are essential features to be modeled in multichannel applications.

### 2.2.2 Nonlinear Baseband Effects

Electrical long-term memory effects are referred to as nonlinear baseband effects. As the words imply, nonlinear baseband effects are memory effects that are attributed to low-frequency or long-time-constant characteristics of an RF system. As the input signal bandwidth increases, as in recent communication systems, nonlinear baseband

effects become more significant because a wide baseband is involved in contributions to the pass-band distortions. Thus, it is now more essential to capture these effects in nonlinear RF system modeling. Nonlinear baseband effects can be observed in a two-tone test as asymmetrical third-order intermodulation products at the output of a power amplifier. The amplitude of the third-order intermodulation product at one side is higher than at the other side [14]–[19]. This will be demonstrated mathematically based on the presentation in [19]. Assume a model that can produce nonlinear baseband effects as shown in Figure 2.5.  $F(\cdot)$  of the model represents a

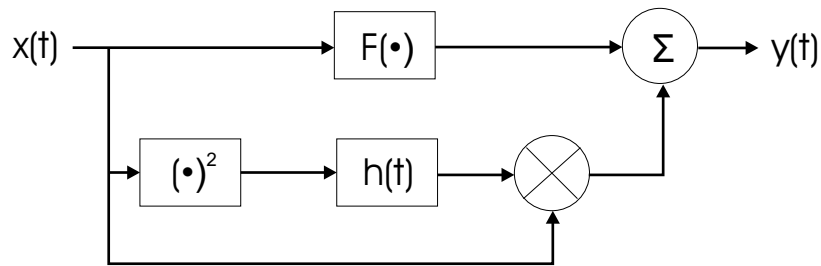


Figure 2.5: Structure of the model being able to capture baseband effects.

static nonlinear function such as

$$F(\cdot) = g_1x(t) + g_3x^3(t) \quad (2.1)$$

where  $g_1$  and  $g_3$  are gain terms, and  $x(t)$  is the input of the model. The output of the model then can be written as

$$y(t) = g_1x(t) + h(t)x^2(t) + g_3x^3(t) \quad (2.2)$$

where  $h(t)$  is the impulse response of the baseband. If the input  $x(t)$  is two tones with the same amplitudes, it can be written as

$$x(t) = A\cos(\omega_1t + \theta_1) + A\cos(\omega_2t + \theta_2). \quad (2.3)$$

The same input amplitudes are enforced in order to show asymmetry caused only by system characteristics. Consequently, the third-order intermodulation products at

the output of the model are derived as

$$\begin{aligned}
 y(t)_{-2\omega_1-\omega_2} &= A^3 \left[ \frac{2}{3} g_3 \cos \left( (2\omega_1 - \omega_2)t + (2\theta_1 - \theta_2) \right) \right. \\
 &+ \frac{1}{4} |H(2\omega_1)| \cos \left( (2\omega_1 - \omega_2)t + (2\theta_1 - \theta_2) + \angle H(2\omega_1) \right) \\
 &\left. + \frac{1}{2} |H(\omega_2 - \omega_1)| \cos \left( (2\omega_1 - \omega_2)t + (2\theta_1 - \theta_2) - \angle H(\omega_2 - \omega_1) \right) \right]
 \end{aligned} \tag{2.4}$$

and

$$\begin{aligned}
 y(t)_{-2\omega_2-\omega_1} &= A^3 \left[ \frac{2}{3} g_3 \cos \left( (2\omega_2 - \omega_1)t + (2\theta_2 - \theta_1) \right) \right. \\
 &+ \frac{1}{4} |H(2\omega_2)| \cos \left( (2\omega_2 - \omega_1)t + (2\theta_2 - \theta_1) + \angle H(2\omega_2) \right) \\
 &\left. + \frac{1}{2} |H(\omega_2 - \omega_1)| \cos \left( (2\omega_2 - \omega_1)t + (2\theta_2 - \theta_1) + \angle H(\omega_2 - \omega_1) \right) \right]
 \end{aligned} \tag{2.5}$$

where  $H(\omega)$  is the Fourier transform of the impulse response  $h(t)$ . In (2.4) and (2.5), it can be assumed that  $H(2\omega_1) \approx H(2\omega_2)$  if the frequency separation,  $\omega_2 - \omega_1$ , is small. Accordingly, each corresponding amplitude is the same so the amplitudes do not affect the asymmetry. As well the phase changes of the input phases,  $\theta_1$  and  $\theta_2$ , do not affect the asymmetry because all terms in (2.4) or (2.5) have the same phase changes of  $2\theta_1 - \theta_2$  or  $2\theta_2 - \theta_1$  respectively. Now, the only factor that can

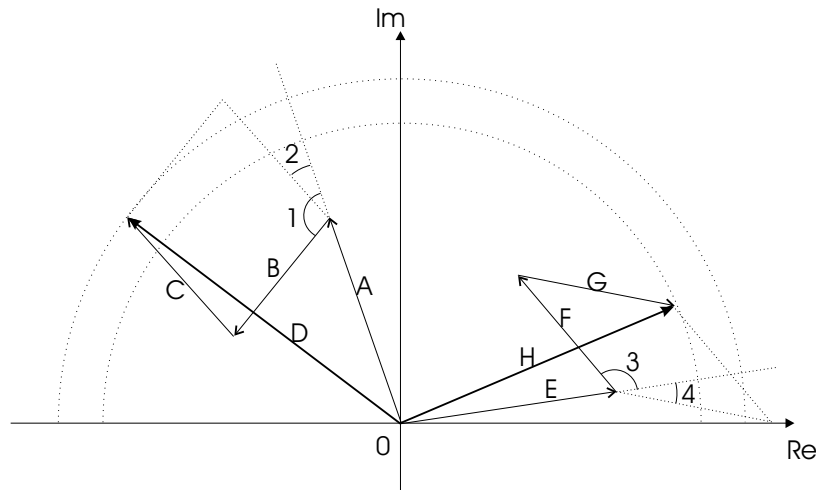


Figure 2.6: Demonstration of the asymmetry mechanism based on (2.4) and (2.5).

be responsible for the asymmetry is  $\angle H(\omega_2 - \omega_1)$  in the last terms of both (2.4)

and (2.5), which come from the frequency up-conversion of the baseband products. In Figure 2.6, the mechanism of the asymmetry is demonstrated according to (2.4) and (2.5). The resulting vectors showing the asymmetry are designated as D and H. All the angles and vectors designated in Figure 2.6 are listed in Table 2.1 and Table 2.2. When an input is a digitally-modulated signal, nonlinear baseband effects

Table 2.1: The angles in Figure 2.6

1	$\angle H(2\omega_1)$
2	$-\angle H(\omega_2 - \omega_1)$
3	$\angle H(2\omega_2)$
4	$\angle H(\omega_2 - \omega_1)$

Table 2.2: The vectors in Figure 2.6

Vector	Magnitude	Angle
A	$\frac{2}{3}g_3A^3$	$2\theta_1 - \theta_2$
B	$\frac{1}{4} H(2\omega_1) $	$2\theta_1 - \theta_2 + \angle H(2\omega_1)$
C	$\frac{1}{2} H(\omega_2 - \omega_1) $	$2\theta_1 - \theta_2 - \angle H(\omega_2 - \omega_1)$
D	$ A+B+C $	$\angle(A+B+C)$
E	$\frac{2}{3}g_3A^3$	$2\theta_2 - \theta_1$
F	$\frac{1}{4} H(2\omega_2) $	$2\theta_2 - \theta_1 + \angle H(2\omega_2)$
G	$\frac{1}{2} H(\omega_2 - \omega_1) $	$2\theta_2 - \theta_1 + \angle H(\omega_2 - \omega_1)$
H	$ E+F+G $	$\angle(E+F+G)$

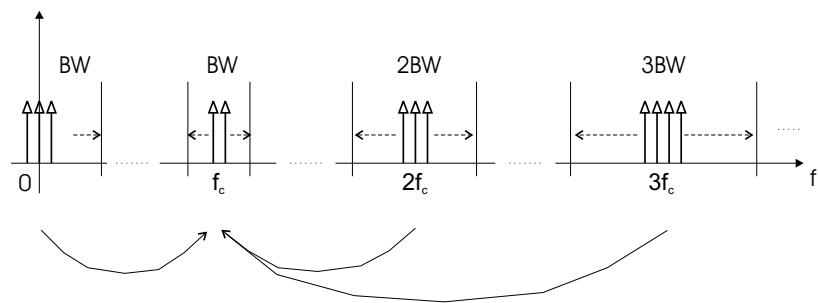
make asymmetric spectral regrowth due to contributions from similar frequency up-conversions of baseband components.

Nonlinear baseband effects can be indirectly measured in a two-tone test [20]–[22] or by using digitally-modulated signals. The idea of these measurements is to have measured outputs include distortions from baseband memory effects by choosing input signals that can stimulate baseband characteristics of the RF system. In a two-tone test, frequency components down-converted to the baseband by nonlinearities are affected by baseband characteristics before they are up-converted to the pass-band and contribute to pass-band frequency components. By measuring and post-processing the amplitude and phase of the pass-band frequency components,

distortions caused by the baseband frequency components can be extracted. Note that the input power level should be low enough that third-order distortion dominates higher-order distortion terms. We accordingly know in post-processing that the up-converted contributions come from baseband components caused by second-order nonlinearities. This kind of measurements provides baseband information of an RF system only at DC and the difference frequency of two input tones. For example, if one of the input tones is at 2 GHz and the other one is at 1.9998 GHz, baseband frequency components exist only at  $-200$  kHz, DC and  $200$  kHz. These components are up-converted to the pass-band and affect frequency components at  $1.9996$  GHz,  $1.9998$  GHz,  $2$  GHz and  $2.0002$  GHz. Thus, measurements of the pass-band frequency components provide information at DC and  $200$  kHz only. To characterize all of the desired baseband, the frequency separation of the input tones needs to be swept to cover the operation bandwidth as shown in Figure 2.7 while measuring amplitudes and phases of fundamental components or third-order intermodulation components at the output. We can either use measurements of fundamental components or third-order intermodulation components to model nonlinear baseband effects because all these components possess contributions of baseband components. However, modeling results will be more accurate if we use third-order intermodulation components. The reason is that powers of fundamental components are much higher than contributions from baseband; thus, extraction of baseband effects tends to suffer from greater measurement error. In post-processing to extract nonlinear baseband effects, measured data are compared with memoryless output data, which can be obtained from a memoryless model discussed in Subsection 2.3.1. After modeling nonlinear baseband effects caused by second-order nonlinearities, higher-order contributions can be modeled similarly by sweeping the amplitudes of the input tones in addition to the frequency sweep. In the two-tone tests, the amplitude and relative phase responses must be measured together. Measuring amplitudes by using a spectrum analyzer is simple but measuring phases is not. Usually a feed-forward cancellation technique is used but this method is cumbersome and time-consuming. The feed-forward technique is beyond the scope of the dissertation. An alternative is to use a single-channel digitally-modulated signal as an input. To circumvent difficulties of phase measure-



(a)



(b)

Figure 2.7: Frequency spectra of (a) a two tone input swept in frequency and amplitude, and (b) the corresponding output.

ment and many times of measurements with different frequency separations of two tones, we can use a vector signal analyzer, which can measure amplitude and phase responses to a digitally-modulated signal. In this scheme, nonlinear baseband effects are indirectly captured by measuring an output spectrum of the fundamental channel as shown in Figure 2.8. Similarly, second-order baseband contributions are

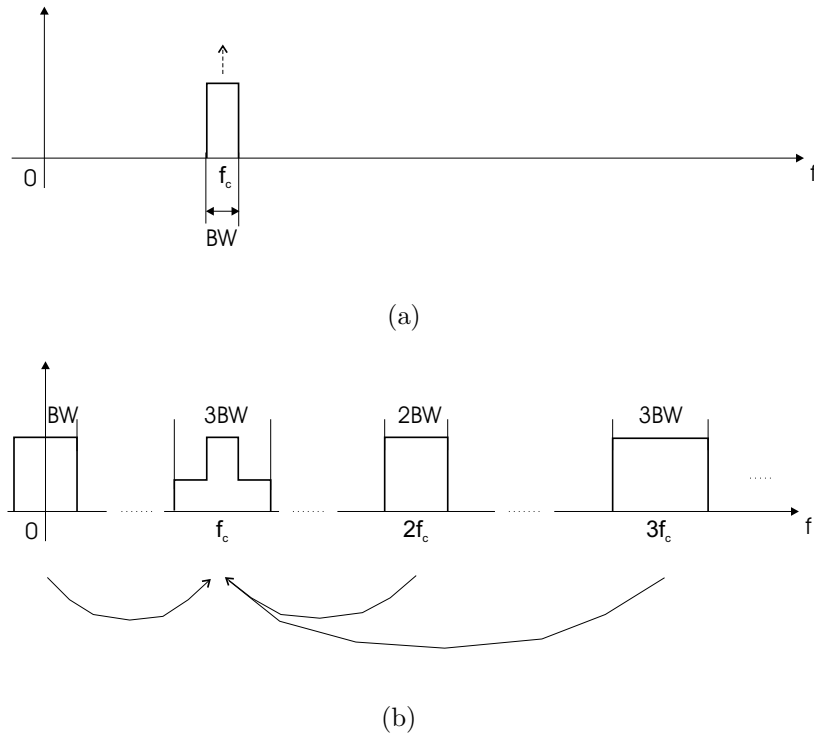


Figure 2.8: Frequency spectra of (a) a digitally-modulated signal swept in amplitude, and (b) the corresponding output.

measured by keeping an input power low enough to maintain third-order nonlinearities to be dominant and then the input power is increased to measure higher-order baseband contributions. At each input power level, nonlinear baseband effects are captured with a one-time measurement. Extracting baseband contributions is somewhat similar to the process with the two-tone case previously discussed but using a digitally-modulated signal as an excitation greatly simplifies measurement. This is demonstrated with a multi-slice behavioral model in Chapter 3 and Chapter 5.

## 2.3 Behavioral Modeling

As the words implies, a behavioral model is an abstraction that approximately relates the input and output of a real subsystem or system. In behavioral modeling, we treat a subsystem or system to be modeled as a black box that has only input and output terminals. Whatever happens inside the box locally is not of interest as long as the modeled output closely matches the output of the real subsystem or system. Compared to low-level models such as analytical models that are represented by nonlinear differential equations, behavioral models have simpler structures and are less computationally demanding in system simulations although they are likely to be less accurate. Hence, behavioral models are extensively used in simulation to estimate performance of large and complex systems since simplicity and computational efficiency are more important than accuracy in large system simulations. A behavioral model (sometimes called block model) consists of one block or more that represent analytical functions and/or filters in the time domain and/or the frequency domain. Each block is intended to capture specific physical phenomena of a system. For example, a block of a static nonlinear function such as a polynomial is used to capture nonlinearities of a system and a block of a frequency domain or z-domain filter is used to capture memory effects of a system. Examples of behavioral models are found in many literatures [23]–[27].

If we consider nonlinear RF systems in the frequency domain, inputs are band-limited signals at the carrier frequencies and the resulting outputs are bandpass-filtered around the carrier frequencies so essential features of nonlinear RF systems that need to be modeled appear around the carrier frequencies. Hence it is usually assumed that a behavioral model of a nonlinear RF system is followed by a bandpass filter around the carrier frequency to eliminate all harmonics at the output of the model as shown in Figure 2.9. Examples are the memoryless nonlinear model discussed in Subsection 2.3.1 and the Wiener-Hammerstein model described in Subsection 2.3.3. Inputs of these models are modulated time-domain signals but sometimes only a complex-envelope signal is used as an input of a model such as the memory polynomial model presented in Subsection 2.3.2. In this case, a bandpass

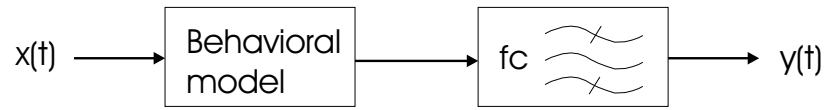


Figure 2.9: Structure of bandpass-type behavioral model

filter following the memory polynomial model is not required because the model directly maps an input complex envelope to an output complex envelope at the carrier frequency.

In behavioral modeling of nonlinear RF systems, there are two major aspects to be considered; structure of a model and extraction of a model. Since structure of a model determines what physical phenomena of an RF system can be mapped into the model, a model should be appropriately constructed to capture intended properties of an RF system. For example, if an input of an RF system is a narrow-band signal, then a memoryless nonlinear model can be used. If an input of an RF system is a wide-band signal and the RF system does not exhibit long-term memory effects, then the Wiener-Hammerstein model can be used. Once structure of a model is decided, then the next step is extraction of the model. Since behavioral models of nonlinear RF systems are usually extracted based on measured data, The procedure used to extract a model depends on what kind of measurements are available such as single-tone, two-tone, multi-tone, complex envelope etc. If physical properties of an RF system to be modeled can be measured directly then extraction of a model is straightforward, but if direct measurement is not possible then a model can sometimes be extracted by post-processing several indirect measurements. Such an indirect extraction is used for a multi-slice model in Chapter 4.

Critically reviewed in the following subsections are various representative behavioral models; memoryless nonlinear model, memory polynomial model and Wiener-Hammerstein model.

### 2.3.1 Memoryless Nonlinear Model

An output of a memoryless nonlinear model in the time domain is the instantaneous response to an input of the model, that is, the output at a moment is determined only by the input at the moment, not by past or future inputs. Any nonlinear function that can describe an instantaneous relation between the input and output can represent a memoryless nonlinear model. Since any analytic function can be approximated as a polynomial, one of the most popular functions used for a memoryless nonlinear model is

$$y(t) = \sum_{k=1}^n a_k x^k(t) \quad (2.6)$$

where  $x(t)$  and  $y(t)$  are the input and output of the model respectively;  $n$  is the order of nonlinearity; and  $a_k$  represents the  $k$  th order coefficient of the polynomial. The coefficients are real numbers when the system modeled exhibits only AM-AM characteristics and are complex numbers when there is AM-PM in addition to AM-AM. The input  $x(t)$  of a single channel can be described in the time domain as

$$x(t) = A(t) \cos(\omega_c t + \theta(t)) \quad (2.7)$$

where  $A(t)$ ,  $\theta(t)$  and  $\omega_c$  are respectively the amplitude, phase in time and center frequency of the signal. By the Euler identities,

$$\begin{aligned} x(t) &= \frac{1}{2} A(t) \left( e^{j(\omega_c t + \theta(t))} + e^{-j(\omega_c t + \theta(t))} \right) \\ &= \frac{1}{2} \left( \hat{x}(t) e^{j\omega_c t} + \hat{x}^*(t) e^{-j\omega_c t} \right) \end{aligned} \quad (2.8)$$

where  $\hat{x}(t)$  ( $= A(t)e^{j\theta(t)}$ ) is the complex envelope of the input and  $\hat{x}^*(t)$  is the conjugate of  $\hat{x}(t)$ . A complex envelope is figuratively described in Section 2.4. Using the binomial expansion,  $x^n(t)$  is obtained as

$$x^n(t) = \frac{1}{2^n} \sum_{k=0}^n \binom{n}{k} [\hat{x}(t)]^k [\hat{x}^*(t)]^{n-k} e^{j\omega_c(2k-n)t}. \quad (2.9)$$

When  $2k - n = \pm 1$ , the contribution of  $x^n(t)$  to the bandpass-filtered output around  $\omega_c$  is derived as

$$x^n(t)_{-\omega_c} = \frac{1}{2^{n-1}} \binom{n}{\frac{n+1}{2}} |\hat{x}(t)|^{n-1} x(t) \quad (2.10)$$

where  $n$  is odd because only odd-order nonlinearities contribute to the passband output. Hence, from (2.6) and (2.10), the bandpass-filtered output around the carrier is given as

$$\begin{aligned} y(t)_{-\omega_c} &= \sum_{k=0}^{(n-1)/2} a_{2k+1} [x(t)]_{-\omega_c}^{2k+1} \\ &= \frac{1}{2} \left( \hat{y}(t) e^{j\omega_c t} + \hat{y}^*(t) e^{-j\omega_c t} \right) \end{aligned} \quad (2.11)$$

where

$$\hat{y}(t) = \sum_{k=0}^{(n-1)/2} \frac{a_{2k+1}}{2^{2k}} \binom{2k+1}{k+1} |\hat{x}(t)|^{2k} \hat{x}(t). \quad (2.12)$$

Extraction of the coefficients,  $a_{2k+1}$ , can be done by fitting to single-tone measurements. While the amplitude of the input tone is swept, the amplitude and phase of the output are collected. The amplitude response is mirrored to the negative input plane so that it becomes an even function of the input amplitude. The phase response is extended to the negative input plane so that it becomes an odd function of the input amplitude. Polynomial fitting to the extended output data then gives complex coefficients in odd orders, say  $b_{2k+1}$ . These fitted coefficients  $b_{2k+1}$  have the following relation with the coefficients  $a_{2k+1}$  in (2.12) as

$$b_{2k+1} = \frac{a_{2k+1}}{2^{2k}} \binom{2k+1}{k+1} \quad (2.13)$$

so  $a_{2k+1}$  is obtained from the fitted coefficients  $b_{2k+1}$  by using (2.13).  $b_{2k+1}$  and  $a_{2k+1}$  are often referred to as envelope and instantaneous coefficients respectively [28].

A memoryless nonlinear model implies in the frequency domain that the model is independent of frequency. Even though a real RF system exhibits frequency-dependent characteristics, a memoryless nonlinear model is a good approximation for narrowband applications since memory of the RF system over a narrow band is usually ignorably small with an assumption that there is no baseband memory. In wide-band or multichannel applications, an RF system exhibits significant memory effects so a memoryless nonlinear model alone cannot accurately account for the system characteristics. Hence it is inappropriate to use a memoryless nonlinear model

for wide-band or multichannel applications. However, there is a situation that a memoryless nonlinear model is combined with linear filters to capture memory effects of a wide-band or multichannel system. An example is the Wiener-Hammerstein model in Subsection 2.3.3. Since it is required to compute a multichannel response of a polynomial model to a multichannel input, the model of (2.6) is here generalized for multichannel applications. In the multichannel case, an  $m$ -channel input signal can be described as

$$\begin{aligned}
x(t) &= \sum_{k=1}^m x_k(t) \\
&= \sum_{k=1}^m A_k(t) \cos(\omega_k t + \theta_k(t)) \\
&= \frac{1}{2} \sum_{k=1}^m \left( \hat{x}_k(t) e^{j\omega_k t} + \hat{x}_k^*(t) e^{-j\omega_k t} \right)
\end{aligned} \tag{2.14}$$

where  $m$  is the number of channels. Using the  $2m$ -polynomial expansion for  $x^n(t)$ , we obtain

$$\begin{aligned}
x^n(t) &= \frac{1}{2^n} \sum_{k_1=0}^n \sum_{k_2=0}^{k_1} \cdots \sum_{k_{2m-1}=0}^{k_{2m-2}} \binom{n}{k_1} \binom{k_1}{k_2} \cdots \binom{k_{2m-2}}{k_{2m-1}} \\
&\times \left( \hat{x}_1(t) \right)^{k_{2m-1}} \left( \hat{x}_1^*(t) \right)^{k_{2m-2}-k_{2m-1}} \left( \hat{x}_2(t) \right)^{k_{2m-3}-k_{2m-2}} \left( \hat{x}_2^*(t) \right)^{k_{2m-4}-k_{2m-3}} \cdots \\
&\times \left( \hat{x}_m(t) \right)^{k_1-k_2} \left( \hat{x}_m^*(t) \right)^{n-k_1} e^{j\omega_1(2k_{2m-1}-k_{2m-2})t} e^{j\omega_2(2k_{2m-3}-k_{2m-2}-k_{2m-4})t} \\
&\times e^{j\omega_3(2k_{2m-5}-k_{2m-4}-k_{2m-6})t} \cdots e^{j\omega_{m-1}(2k_3-k_4-k_2)t} e^{j\omega_m(2k_1-k_2-n)t}
\end{aligned} \tag{2.15}$$

By using (2.6) and (2.15), the bandpass outputs of the memoryless nonlinear model for multichannel applications can be obtained. For example, the bandpass output around  $\omega_1$  is computed when the exponent of the first exponential function in (2.15) is  $\pm 1$  and the exponents of the other exponential functions are zeros.

### 2.3.2 Memory Polynomial Model

One of the recent behavioral models able to capture memory effects of RF power amplifiers is the memory polynomial model [29]–[31]. The model is regarded as a truncation of the general Volterra series [32] since it contains significantly fewer Volterra

kernels. This is an efficient way in terms of computation and modeling. In another perspective, the memory polynomial model being used to model a nonlinear system with memory corresponds to the adaptive delay filter [33] being used to model a linear system with memory. Instead of linear gain blocks in the adaptive delay filter, static nonlinear function blocks are used in the model. The structure of the model is shown in Figure 2.10. Each branch of the model consists of a delay component expressed

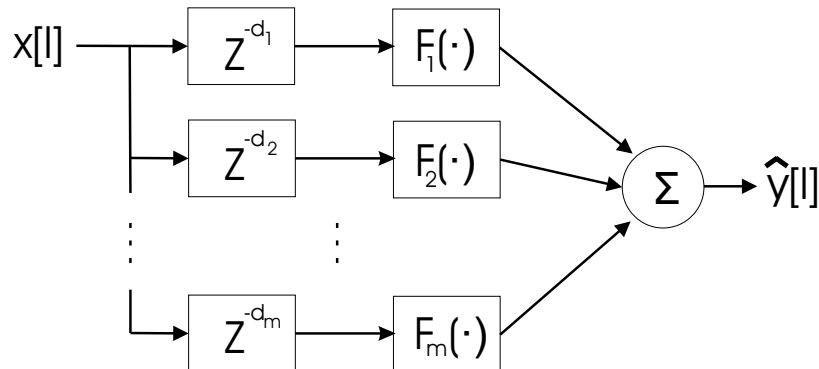


Figure 2.10: Structure of the memory polynomial model

in the  $Z$ -domain and a memoryless nonlinear component expressed in the form of an odd order polynomial with complex coefficients. The output of the model is the sum of the output of each branch. The delay components followed by polynomials account for nonlinear influences of past inputs to the output. The delay components can be unit incremental delays [34] or sparse delays. Compared to a unit incremental delay model, a sparse delay model is known to computationally efficiently capture memory effects, especially long term memory effects, for a given number of delay taps. The reason is that the model with sparse delay taps can have relatively longer delays and the longer delays the model has, the longer-term memory effects the model can capture.

The output of the model in Figure 2.10 is represented as

$$\hat{y}[l] = \sum_{q=1}^m \sum_{k=1}^n a_{2k-1,q} \left| x[l - d_q] \right|^{2(k-1)} \cdot x[l - d_q] \quad (2.16)$$

where  $\hat{y}[l]$  is the modeled discrete complex-envelope output and  $x[l]$  is the discrete

complex-envelope input.  $m$ ,  $a_{2k-1,q}$  and  $d_q$  are the number of branches, the  $2k - 1$  th complex coefficients of the polynomials and the delay value of the  $q$  th branch respectively. The model considers the order of nonlinearity up to  $2n - 1$ . In (2.16), the coefficients of the polynomials are unknowns to be extracted if unit incremental delay taps are used, but both the coefficients and delay values are unknowns if sparse delay taps are used. These unknowns are determined by iteration. In order to establish an error function for iteration, (2.16) is converted to a matrix equation. A matrix of measured output data of a system to be modeled is represented as

$$\mathbf{Y} = [y[l] \ y[l+1] \ \cdots \ y[l+N-1]]^T \quad (2.17)$$

where  $N$  is the number of consecutive data. Now, the right hand side of (2.16) can be represented by the matrix equation

$$\hat{\mathbf{Y}} = \mathbf{H} \cdot \mathbf{a}. \quad (2.18)$$

where

$$\mathbf{H} = [\mathbf{H}_1 \ \cdots \ \mathbf{H}_q \ \cdots \ \mathbf{H}_m] \quad (2.19)$$

$$\mathbf{H}_q = \begin{bmatrix} h_{1,q}[l] & h_{3,q}[l] & \cdots & h_{2n-1,q}[l] \\ h_{1,q}[l+1] & h_{3,q}[l+1] & \cdots & h_{2n-1,q}[l+1] \\ \vdots & \vdots & \vdots & \vdots \\ h_{1,q}[l+N-1] & h_{3,q}[l+N-1] & \cdots & h_{2n-1,q}[l+N-1] \end{bmatrix} \quad (2.20)$$

$$h_{2k-1,q}[l] = |x[l-d_q]|^{2(k-1)} \cdot x[l-d_q] \quad (2.21)$$

and

$$\mathbf{a} = [\mathbf{a}_1 \ \cdots \ \mathbf{a}_q \ \cdots \ \mathbf{a}_m] \quad (2.22)$$

where

$$\mathbf{a}_q = [a_{1,q} \ a_{3,q} \ \cdots \ a_{2n-1,q}]^T. \quad (2.23)$$

The dimensions of the matrix  $\mathbf{H}$  and  $\mathbf{a}$  are  $N \times n \cdot m$  and  $n \cdot m \times 1$  respectively, so the dimension of the modeled output  $\hat{\mathbf{Y}}$  is  $N \times 1$ , which is same as the dimension of

the measured output  $\mathbf{Y}$ . An error function is formulated as

$$\mathbf{E} = \mathbf{Y} - \hat{\mathbf{Y}} \quad (2.24)$$

$$= \mathbf{Y} - \mathbf{H} \cdot \mathbf{a} \quad (2.25)$$

$$= \left[ e[l] \ e[l+1] \ \cdots \ e[l+N-1] \right]^T \quad (2.26)$$

where  $e[l]$  is a difference vector between the measured and modeled datum at the sample time  $l$ . The accuracy of extracted parameters, the delay values and the coefficients of the polynomials, can be quantified as the rms value of the error  $\mathbf{E}$ :

$$\text{rmse} = \left( \frac{1}{N} \sum_{k=0}^{N-1} |e[l+k]|^2 \right)^{1/2}. \quad (2.27)$$

The parameters are determined such that the rms error is minimized. A block diagram of the system identification is shown in Figure 2.11. For the unit incremental delay

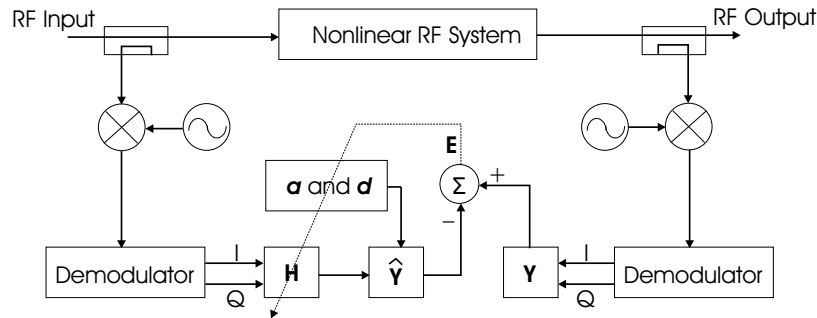


Figure 2.11: System identification of the memory polynomial model

model, the delay value matrix,  $\mathbf{d} = [d_1 \ d_2 \ \cdots \ d_m]$ , are fixed as  $\mathbf{d} = [1 \ 2 \ \cdots \ m]$ , so the parameters to be extracted are the coefficients of the polynomials,  $\mathbf{a}$ . The coefficients can be relatively easily determined by iteration, such as the Newton-Raphson method. However, the delay values are also unknowns for the sparse delay model in addition to the coefficients of the polynomials. The delay values and coefficients cannot be extracted by iteration at the same time. The reason is that an expected delay value needs to be a natural number; however, the error values from (2.24) are complex numbers and the resulting Jacobian matrix is also complex so that iterative fitting

generates complex delay values. In references [33] and [35] the parameters of the model were determined by sequential implementation in which the first branch of the model was extracted and then the second was done and so on as shown in Figure 2.12. In the sequential implementation there are two loops of iteration for each branch.

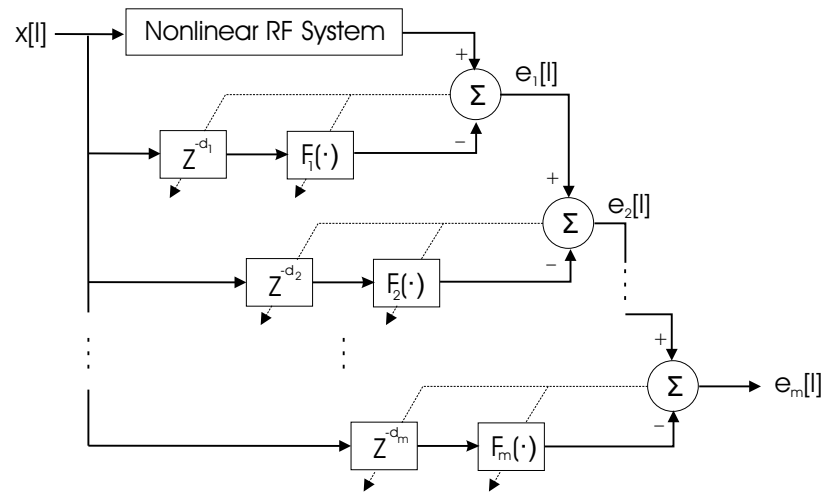


Figure 2.12: Sequential implementation of the memory polynomial model

The inner loop is for the coefficients of the polynomials and the outer loop is for the sparse delay taps. Up to a certain maximum delay, the optimum coefficients are extracted iteratively while delay values are incrementally changed, and then the optimum delay values and coefficients are chosen. Usually the first delay value is zero due to dominance of the memoryless portion over the memory portion of a power amplifier.

A memory polynomial model can capture memory effects but there are two aspects to be considered on modeling memory effects. First, the model is not suitable for capturing short-term memory effects since a baseband-like complex-envelope signal is used to extract parameters of the model and usually time constants of short-term memory effects are shorter than a sampling period of the complex envelope. The other aspect of the model is that it can capture long-term memory effects; however, it only captures some of the actual memory effects of a power amplifier. The reason is that each branch of the model has single constant delay component so it captures

memory effects caused from characteristics of the amplifier at only a single frequency. As to an incremental unit delay model, it could rigorously capture long-term memory effects of a system if the sampling frequency of the input data were high enough to account for long-term memory effects with a relatively short-time constant and the model had a sufficient number of branches to account for long-term memory effects with a relatively long-time constant. The advantage of the sparse delay model is its simplicity but it is not suitable for modeling memory effects when an amplifier exhibits a lot of variation of characteristics over a relatively narrow frequency band, especially baseband. A relatively narrow frequency band is very common in practical amplifiers. Therefore, optimum parameter extraction of a memory polynomial model is not only difficult but also likely to be dependent on the input signal to be used for model extraction. Thus the extracted model must be validated by testing with various types of signals such as a single-tone, multi-tone, digitally-modulated signal etc.

In the previous discussion it was pointed out that a polynomial model cannot capture the two aspects of memory effects considered. As well as described below a memory polynomial model is not suitable for multichannel applications. If an input signal comprises two channels each of which has a digitally-modulated signal, and the frequency separation of the two channels is large compared to the channel bandwidth, then the complex envelope of the signal varies much faster than the complex envelopes of each individual channel. In the case of a two-channel WCDMA signal, the channel bandwidth is around 5 MHz and so, approximating, the fastest modulation signals of the each individual channel have a period of  $0.2 \mu$  seconds. If a channel separation of the two-channel WCDMA signal is 100 MHz and a single complex envelope is used to represent the signal, then the fastest modulation signal has a period of  $0.01 \mu$  second. Thus the complex envelope changes twenty times more often than the complex envelopes of the individual channels. This implies that twenty times more data must be stored and processed to extract a model with the same accuracy in terms of capturing memory effects. Consequently simulation using single-channel frequency envelope simulation takes much longer for a given period of an input. If the two-channel signal were individually treated as two single channels, with

each represented by their own complex envelope but with different carrier frequencies, the previously mentioned problems of model extraction and simulation time could be avoided. However, a memory polynomial model cannot be extracted by using an input of two complex envelopes since the model is independent on carrier frequencies.

### 2.3.3 Wiener-Hammerstein (3 box) Model

Memory effects of a system are frequency-dependent characteristics so it is natural that a behavioral model employ linear filters to account for memory effects. One of the simplest nonlinear models able to capture memory effects is the Wiener-Hammerstein model [36], often referred to as the 3-box model, which consists of two linear filter boxes,  $H_1(f)$  and  $H_2(f)$ , and one static nonlinear function box,  $F(\cdot)$ , between the linear filter boxes as shown in Figure 2.13. This model has been used extensively

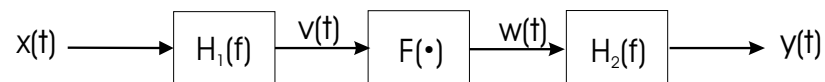


Figure 2.13: Structure of the Wiener-Hammerstein model

in modeling nonlinear systems with memory [37]–[40]. The static nonlinear function describes AM-AM and AM-PM characteristics at the reference frequency (usually the center frequency of the operating frequency band) of the model. The linear filters that are normalized at the reference frequency account for deviations of AM-AM and AM-PM at different frequencies from the AM-AM and AM-PM at the reference frequency. To demonstrate the functionality of the model mathematically, we can represent the static nonlinear function box as a polynomial function with complex coefficients as in (2.6). The polynomial function is rewritten here for convenience as

$$w(t) = \sum_{k=1}^n a_k v^k(t) \quad (2.28)$$

and a sinusoid input signal at the reference frequency is written as

$$x_r(t) = A \cos(2\pi f_r t + \theta) \quad (2.29)$$

where  $A$  is the amplitude of the input signal. (2.29) can conveniently be expressed in the phasor form as

$$\hat{x}_r = Ae^{j\theta}. \quad (2.30)$$

Thus the output response of the model at the reference frequency is derived in phasor form as

$$\begin{aligned} \hat{y}_r &= \sum_{k=0}^{(n-1)/2} b_{2k+1} \left| H_1(f_r) \hat{x}_r \right|^{2k} H_1(f_r) H_2(f_r) \hat{x}_r \\ &= \sum_{k=0}^{(n-1)/2} b_{2k+1} A^{2k+1} e^{j\theta} \end{aligned} \quad (2.31)$$

where  $b_{2k+1}$  represents the envelope coefficients as in (2.13).  $H_1(f_r) = 1$  and  $H_2(f_r) = 1$  since  $H_1(f)$  and  $H_2(f)$  are normalized to the reference frequency. When an input tone is at another frequency, say  $f_1$ , the output response of the model can be written as

$$\begin{aligned} \hat{y}_1 &= \sum_{k=0}^{(n-1)/2} b_{2k+1} \left| H_1(f_1) \hat{x}_1 \right|^{2k} H_1(f_1) H_2(f_1) \hat{x}_1 \\ &= \sum_{k=0}^{(n-1)/2} b_{2k+1} \left| H_1(f_1) A \right|^{2k+1} \left| H_2(f_1) \right| e^{j\theta} e^{j(\theta_{H_1(f_1)} + \theta_{H_2(f_1)})} \end{aligned} \quad (2.32)$$

where  $\hat{x}_1 (= Ae^{j\theta})$  is the phasor of  $x_1(t) (= A \cos(2\pi f_1 t + \theta))$ .  $\theta_{H_1(f_1)}$  and  $\theta_{H_2(f_1)}$  are respectively the phase responses of the filter  $H_1$  and  $H_2$  at the frequency  $f_1$ . In order to demonstrate that the linear filters make displacements of the reference AM-AM and AM-PM at different frequencies, it is convenient to consider AM-AM and AM-PM characteristics of the model separately. If we compare only the AM-AM characteristics of (2.31) and (2.32), the output amplitude at the frequency  $f_1$  can be viewed as if the input amplitude  $A$  at the reference frequency is pre-emphasized (or deemphasized) by  $|H_1(f_1)|$  and then post-emphasized (or deemphasized) by  $|H_2(f_1)|$  after through the static nonlinearity. Therefore, the filters  $H_1(f)$  and  $H_2(f)$  respectively capture horizontal and vertical displacements of the reference AM-AM characteristic by  $-20 \log(|H_1(f_1)|)$  and  $20 \log(|H_2(f_1)|)$  respectively when the input and output amplitudes are expressed in log scales. The negative sign is present due to a positive

(or negative) horizontal shift when  $|H_1(f_1)| < 1$  (or  $|H_1(f_1)| > 1$ ). If we look at the AM-PM characteristics of (2.31) and (2.32) and find that  $|H_2(f_1)|$  makes no contribution to the output phase modulation, then the output phase at the frequency  $f_1$  can be written as

$$\angle \hat{y}_1 = \Phi(|H_1(f_1)|A) + \theta_{H_1(f_1)} + \theta_{H_2(f_1)} \quad (2.33)$$

where  $\Phi(\cdot)$  is defined as

$$\begin{aligned} \angle \hat{y}_r &= \angle \left( \sum_{k=0}^{(n-1)/2} b_{2k+1} A^{2k+1} \right) + \theta \\ &= \Phi(A) . \end{aligned} \quad (2.34)$$

From (2.33) and (2.34), the AM-PM response at the frequency  $f_1$  looks as if the AM-PM response at the reference frequency is horizontally shifted by  $-20 \log(|H_1(f_1)|)$  and then is vertically shifted by  $\theta_{H_1(f_1)} + \theta_{H_2(f_1)}$  as shown in Figure 2.14. The dashed

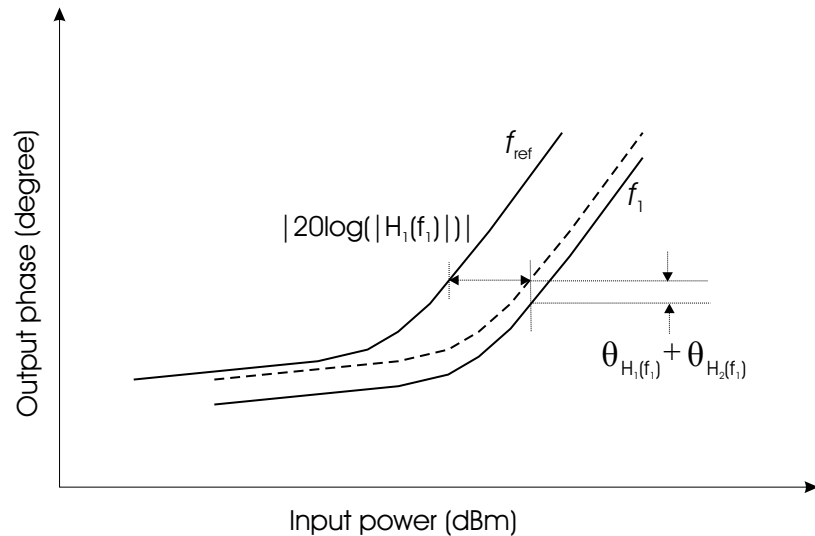


Figure 2.14: AM-PM responses of the Wiener-Hammerstein model

line in Figure 2.14 represents a horizontal displacement of the reference AM-PM response and the two solid lines are assumed to be measured AM-PM responses at the reference frequency,  $f_{\text{ref}}$ , and the frequency  $f_1$  each.

Extraction of the polynomial function with complex coefficients was described in Subsection 2.3.1. Extraction of the linear filters can be done from the observations made so far in this section, or it can be done by numerical fitting. The latter will be exploited in Chapter 5. In the extraction based on the observations, it is assumed that AM-AM and AM-PM responses of a real system to be modeled can be approximated by some combination of horizontal and vertical displacements from the AM-AM and AM-PM responses at the reference frequency. Figure 2.15 shows how an AM-AM response is affected by the linear filters of the 3-box model. The dashed line represents a horizontal displacement of the reference AM-AM response and the two solid lines are assumed to be measured AM-AM responses at  $f_{\text{ref}}$  and  $f_1$  as indicated. The horizontal displacement of the reference AM-AM in Figure 2.15 is described as

$$-20 \log(|H_1(f_1)|) = -20 \log(|H_{ss}(f_1)|) + 20 \log(|H_{sat}(f_1)|) \quad (2.35)$$

where  $H_{ss}(f)$  and  $H_{sat}(f)$  represent small-signal and saturated responses. The data  $H_{ss}(f)$  and  $H_{sat}(f)$  are obtained from  $S_{21}$  measurements over the operational frequency band at a low-input level (where nonlinearity is negligible), and at the 1 dB compression point respectively. The responses are then normalized to the responses at the reference frequency. Note that the AM-AM responses in the small-signal region have one-to-one slopes. From (2.35) and noting that the vertical displacement of the reference AM-AM response is  $20 \log(|H_2(f_1)|)$  as observed before, amplitudes of the linear filters can be written as

$$\left|H_1(f)\right| = \frac{\left|H_{ss}(f)\right|}{\left|H_{sat}(f)\right|} \quad \text{and} \quad \left|H_2(f)\right| = \left|H_{sat}(f)\right|. \quad (2.36)$$

In Figure 2.14, the horizontal displacement of the reference AM-PM response is determined by the amplitude of  $H_1$  and not by the phase of  $H_1$ . Hence the AM-PM response at the frequency  $f_1$  must be modeled only by a vertical displacement. Since the vertical displacement is determined by  $\theta_{H_1(f_1)} + \theta_{H_2(f_1)}$ , there is freedom to choose each individual phase response of the linear filters as long as it is kept that the vertical displacement of the reference AM-PM is  $\theta_{H_1(f_1)} + \theta_{H_2(f_1)}$  much. For convenience,

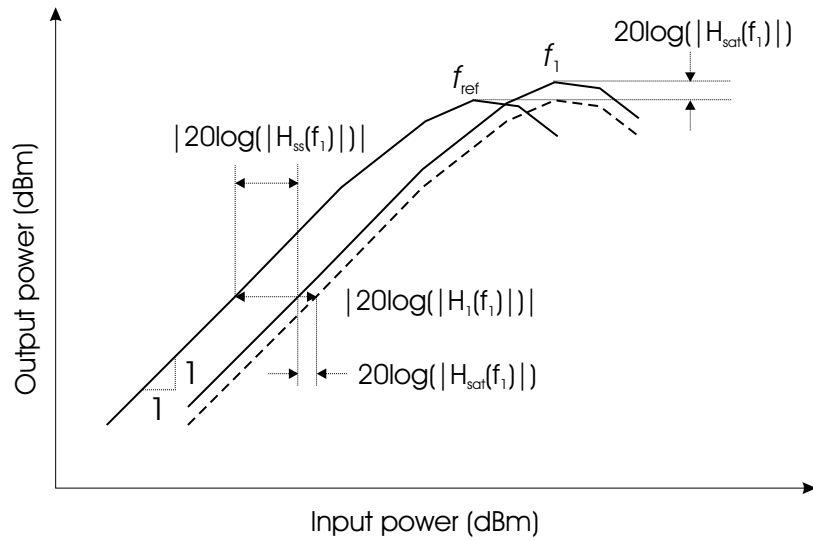


Figure 2.15: AM-AM responses of the Wiener-Hammerstein model

choose the phase response of  $H_1$  as

$$\angle H_1(f) = \angle H_{ss}(f) \quad (2.37)$$

and then the phase response of  $H_2$  becomes

$$\angle H_2(f) = \phi - \angle H_{ss}(f) \quad (2.38)$$

where  $\phi$  is defined as  $\theta_{H_1(f)} + \theta_{H_2(f)}$ . Therefore, from (2.36), (2.37) and (2.38), the frequency response of the linear filters can be derived as

$$H_1(f) = \frac{H_{ss}(f)}{|H_{sat}(f)|} \quad \text{and} \quad H_2(f) = |H_{sat}(f)| e^{j(\phi - \angle H_{ss}(f))}. \quad (2.39)$$

Even though a real RF system does not exactly exhibit horizontally and vertically displaced responses of the reference AM-AM and AM-PM responses at frequencies other than the reference frequency, (2.39) has been formed to be a fairly good approximation up to a 1 dB compression point.

Advantages of the Wiener-Hammerstein model are simplicities in terms of model structure and extraction. In addition it can capture memory effects; however, it can

only capture short-term memory effects since the linear filters of the model only characterize the passband of a system. In particular, the linear filters are usually extracted from single-tone measurements. The tone is swept in frequency and amplitude over a passband so, at the first place, the measured data cannot include long-term memory effects as these cannot be observed. Putting this in another context, long-term memory effects cannot be captured even with perfect model extraction from the measured data. Even if a more realistic test signal was used, such as a digitally-modulated signal, the presence of long-term memory effects in the measured data would result in large model extraction error if the extraction were possible. Therefore, this is a structural problem of the model. However, the model captures short-term memory over a wide frequency band fairly well so it is utilized as part of a multi-slice behavioral model for multichannel applications in Chapter 4.

## 2.4 Simulating RF models

### 2.4.1 Transient Analysis

An electronic circuit consists of linear and nonlinear elements. Linear elements include resistors, capacitors and inductors. Nonlinear elements include diodes, transistors etc. In a transient analysis linear elements are expressed in corresponding linear constitutive relations and nonlinear elements are modeled by nonlinear dependent sources. Thus a circuit can be expressed in nonlinear algebraic equations developed using KCL and KVL in the time domain. In transient analysis the equations are solved at each sampling time by Newton iterations. The solutions are instantaneous node voltages and branch currents. In transient analysis the derivatives utilized in Newton iteration are changes of voltages or currents (or state variables) with respect to time so computation of derivatives is based on voltages and currents at the prior time step.

One of the advantages of transient analysis is that it can handle virtually all types of signals including discrete tones, digital signals, noise and digitally-modulated

signals. However there are limitations in handling modulated RF signals such as AM, FM, digitally-modulated signals where the information signal changes very slowly compared to the modulated signal. To obtain reliable results in transient analysis requires tremendous computational demands as simulation must proceed for a long time. This results in accumulated numerical error as well as the simulation times being unreasonably long. Therefore transient analysis is not suitable for the simulation of RF front ends handling modulated signals.

### 2.4.2 Harmonic Balance Analysis

In harmonic balance analysis a circuit is partitioned into linear and nonlinear sub-circuits as shown in Figure 2.16. The linear sub-circuit includes linear elements

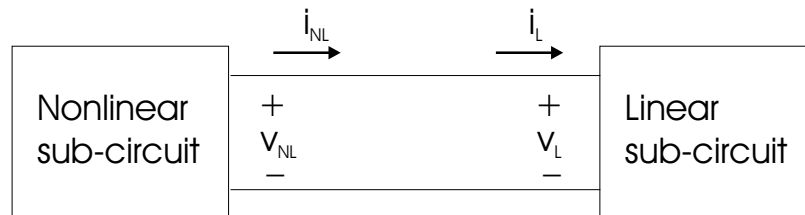


Figure 2.16: Partition of a circuit in harmonic balance

and independent sources. The rest of the circuit is included in the nonlinear sub-circuit. The linear and the nonlinear sub-circuit are respectively computed in the time and frequency domains. Simulation progress by equating the voltages and currents at the interface of the two sub-circuits. For example, the linear currents  $i_L$  are initially estimated and then the linear voltages  $v_L$  are computed. This evaluation is performed in the frequency domain, that is,  $i_L$  and  $v_L$  are expressed as phasors. Next the phasors of the linear voltage are converted to time-domain signals by an inverse Fourier transform and are equated to the nonlinear voltages  $v_{NL}$ . Next the nonlinear currents  $i_{NL}$  are computed from the nonlinear voltage. Finally the nonlinear current is converted to phasors using a Fourier transform and compared to the linear current phasors. If the differences of the linear and the nonlinear voltage phasors are above

a preassigned tolerance, the linear voltage phasors are updated to values that reduce the differences. This process is performed iteratively until the differences are below the tolerance and ‘balanced’ currents are obtained for the two sub-circuits.

Harmonic balance analysis is not affected by the frequency of the drive signal; however, it can handle only a drive signal that can be expressed as a sum of time-independent discrete tones in the frequency domain. Since there is no derivative in a linear sub-circuit equations, solutions are always time-independent phasors. Thus harmonic balance captures only steady-state responses and it cannot handle modulated RF signals that cannot be expressed as a combination of time-independent discrete tones.

### 2.4.3 Conventional Envelope Transient Analysis

Digitally-modulated signals cannot be represented as discrete tones nor conveniently as time-domain waveforms. A single digitally-modulated channel appears as an RF tone whose amplitude and phase vary relatively and extremely slowly corresponding to the amplitude and phase variations constituting the envelope of the signal. For example, a modulation signal in the WCDMA format is 5 MHz wide with a carrier frequency around 2 GHz. Thus the modulation signal appears to vary by one cycle in amplitude and phase over 400 or so RF cycles. The Envelope Transient (ET) method can be used efficiently with modulated signals as the signal is modeled as a sequence of time-varying phasors. The variation of these phasors constitutes the envelope of the signal. Thus analysis can progress as a large sequence of single-tone Harmonic Balance (HB) simulations with low frequency (envelope) derivatives linking the simulations. Representing a digitally-modulated signal as a slowly-varying phasor, transforms a circuit simulation problem into a two-rate problem [41] with a fast rate for the RF carrier and a slow rate being used to capture the modulation envelope and baseband effects. More specifically low-frequency derivatives capture long-term memory effects when a suitable model is used that inherently models these effects.

As in the conventional HB technique, a circuit is partitioned into linear and non-

linear subcircuits with state variables of the nonlinear elements effectively interfacing the subcircuits. The circuit equations describing the two subcircuits are written in the frequency domain as

$$X(\omega) = A(\omega)Y(\omega) + B(\omega)G(\omega) \quad -\infty < \omega < \infty \quad (2.40)$$

and in the time domain as

$$y(t) = f(x(t)). \quad (2.41)$$

Here  $X(\omega)$ ,  $Y(\omega)$  and  $G(\omega)$  are spectra of the state variables,  $x(t)$ , the electrical variables,  $y(t)$ , and the driving sources,  $g(t)$ , respectively. Also,  $A(\omega)$  and  $B(\omega)$  are the transfer functions characterizing the linear subcircuits. Note that the use of arbitrary state variables does not restrict the linear circuit to having just admittance descriptions. The nonlinear subcircuit is described by instantaneous relations between the individual state variables of  $x$  and the components of  $y$ . With a digitally-modulated excitation the carrier signal and its harmonics have time-varying envelopes having the form

$$\begin{aligned} z(t) &= \Re \left[ \sum_{k=0}^N \hat{Z}_k(t) e^{jk\omega_0 t} \right] \\ &= \frac{1}{2} \sum_{k=0}^N \left( \hat{Z}_k(t) e^{jk\omega_0 t} + \hat{Z}_k^*(t) e^{-jk\omega_0 t} \right) \end{aligned} \quad (2.42)$$

where  $\hat{Z}_k(t)$  is the time varying complex envelope of the  $k$  th harmonic. Figure 2.17 present the relationship between  $z(t)$  and  $\hat{Z}_k(t)$  in the 2-dimensional vector domain. Figure 2.17(a) is the spectrum of the  $k$  th harmonic of the digitally-modulated signal  $z(t)$  showing both the positive and the negative frequency-domain components. A representation of the digitally-modulated signal as an RF phasor is given in Figure 2.17(b) where the amplitude and the phase of the phasor vary with time. The spectrum of the envelope portion of the modulated signal, i.e.  $\hat{Z}_k(t)$ , is shown in Figure 2.17(c) and its phasor representation in Figure 2.17(d). The projections of the  $z(t)$  and  $\hat{Z}_k(t)$  vectors on the real axis are the original signal and envelope, respectively, in the time domain.

The first key concept of the ET method is the use of two time scales. This enables the computation of a time-varying envelope on a slow time scale while the high frequency effects are on a fast time scale. Rewriting (2.42) with two time scales yields:

$$\begin{aligned} z(t_1, t_2) &= \Re \left[ \sum_{k=0}^N \hat{Z}_k(t_1) e^{jk\omega_0 t_2} \right] \\ &= \frac{1}{2} \sum_{k=0}^N \left( \hat{Z}_k(t_1) e^{jk\omega_0 t_2} + \hat{Z}_k^*(t_1) e^{-jk\omega_0 t_2} \right) \end{aligned} \quad (2.43)$$

where  $\omega_0$  is the RF carrier frequency. The time scale  $t_1$  is used with the complex envelopes and  $t_2$  is used with the high frequency signals including the carrier and its harmonics. The second key concept is transforming that part of the problem with the fast time scale into a problem that can be solved in the frequency domain. Thus we define  $\hat{Z}_k(t_1)$ , the inverse Fourier transform of  $\hat{Z}_k(\omega)$  as

$$\hat{Z}_k(t_1) = \frac{1}{2\pi} \int_{-BW/2}^{BW/2} \hat{Z}_k(\omega) e^{j\omega t_1} d\omega \quad (2.44)$$

where BW is the bandwidth of the spectrum of the RF signal as shown in Figure 2.17(c). BW is inversely proportional to the size of the time step when  $\hat{Z}_k(t)$  is discretized with respect to time. Similarly  $Z_k(\omega)$  is the spectral component of  $z(t)$  centered at the  $k$ th harmonic of the RF carrier.  $\hat{Z}_k(\omega)$  can be thought of as the positive frequency spectrum of  $Z_k(\omega)$  windowed around  $k\omega_0$  and down-converted by  $k\omega_0$ . The amplitude of  $\hat{Z}_k(\omega)$  is two times that of  $Z_k(\omega)$ . From (2.43) and (2.44) it can be seen that the Fourier transform of  $z(t)$  can be approximated without loss of signal information as

$$Z(\omega) \Big|_{BW} = \frac{1}{2} \sum_{k=0}^N \left( \hat{Z}_k(\omega - k\omega_0) + \hat{Z}_k^*(-\omega - k\omega_0) \right) \quad (2.45)$$

where  $Z(\omega) \Big|_{BW}$  represents spectrums within the bandwidth BW around each of the harmonics of the RF carrier, i.e.  $\pm k\omega_0$  as in Figure 2.17(e). Thus with either  $\hat{Z}_k(\omega)$  or with  $\hat{Z}_k(t_1)$  the total truncated spectrum  $Z(\omega) \Big|_{BW}$  can be obtained.

Now  $x(t)$ ,  $y(t)$  and  $g(t)$  of (2.40) are in the same form as  $z(t)$  so that the spectra of envelopes of  $x(t)$ ,  $y(t)$  and  $g(t)$  at  $k\omega_0$  are conveniently represented as  $\hat{X}_k(\omega - k\omega_0)$ ,

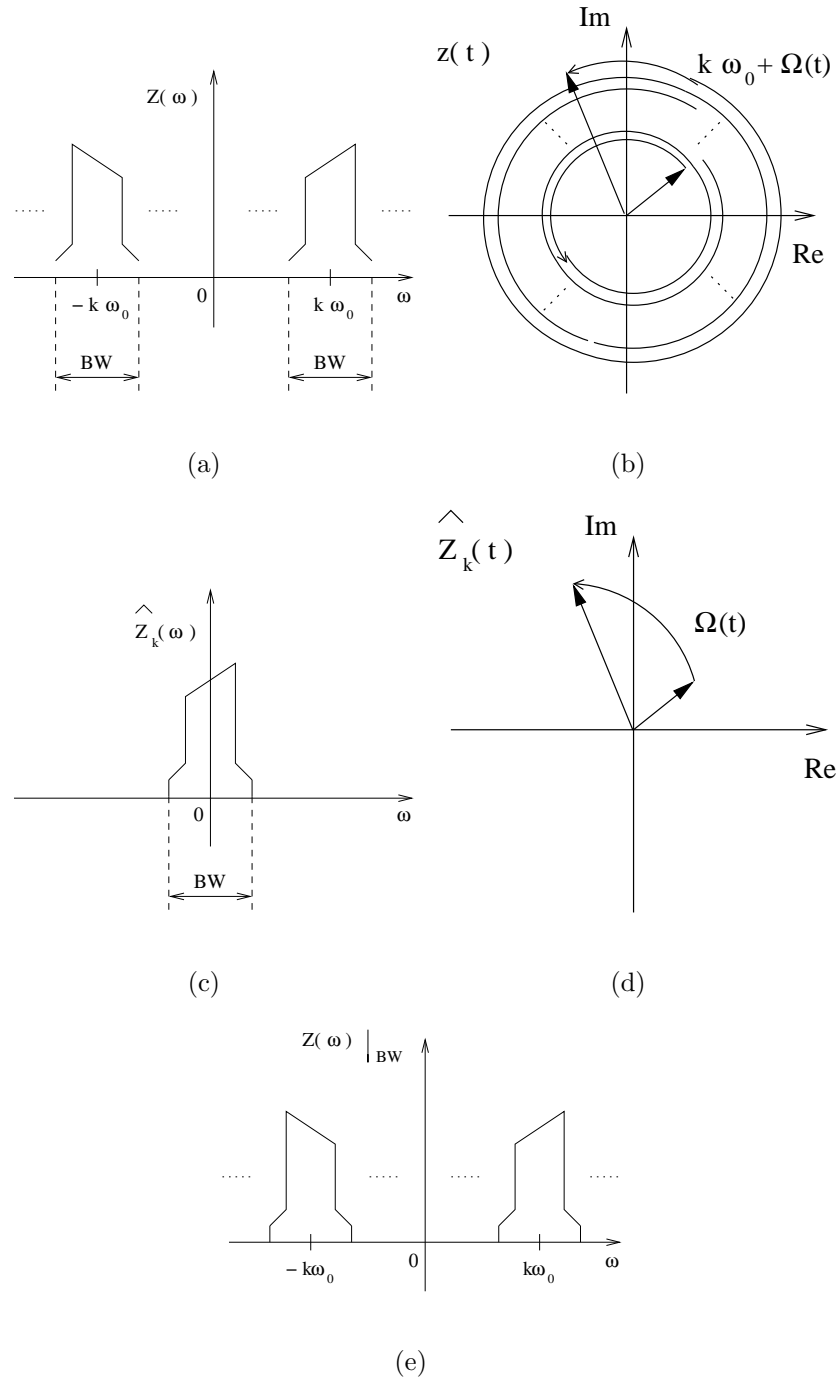


Figure 2.17: Frequency domain representations of a single-channel digitally-modulated signal: (a) its spectrum; (b) its representation as a phasor with amplitude and phase varying slowly in time; (c) envelope signal; (d) the phasor presentation of the envelope; and (e) its windowed spectrum of the modulated RF signal in (a).

$\hat{Y}_k(\omega - k\omega_0)$  and  $\hat{G}_k(\omega - k\omega_0)$  respectively. Then the linear subcircuit equation, (2.40), becomes:

$$\hat{X}_k(\omega - k\omega_0) = A(\omega)\hat{Y}_k(\omega - k\omega_0) + B(\omega)\hat{G}_k(\omega - k\omega_0). \quad (2.46)$$

This can be rewritten as

$$\hat{X}_k(\Omega) = A(\Omega + k\omega_0)\hat{Y}_k(\Omega) + B(\Omega + k\omega_0)\hat{G}_k(\Omega) \quad (2.47)$$

with  $\Omega = \omega - k\omega_0$ . In effect, the RF signals are frequency down-converted enabling

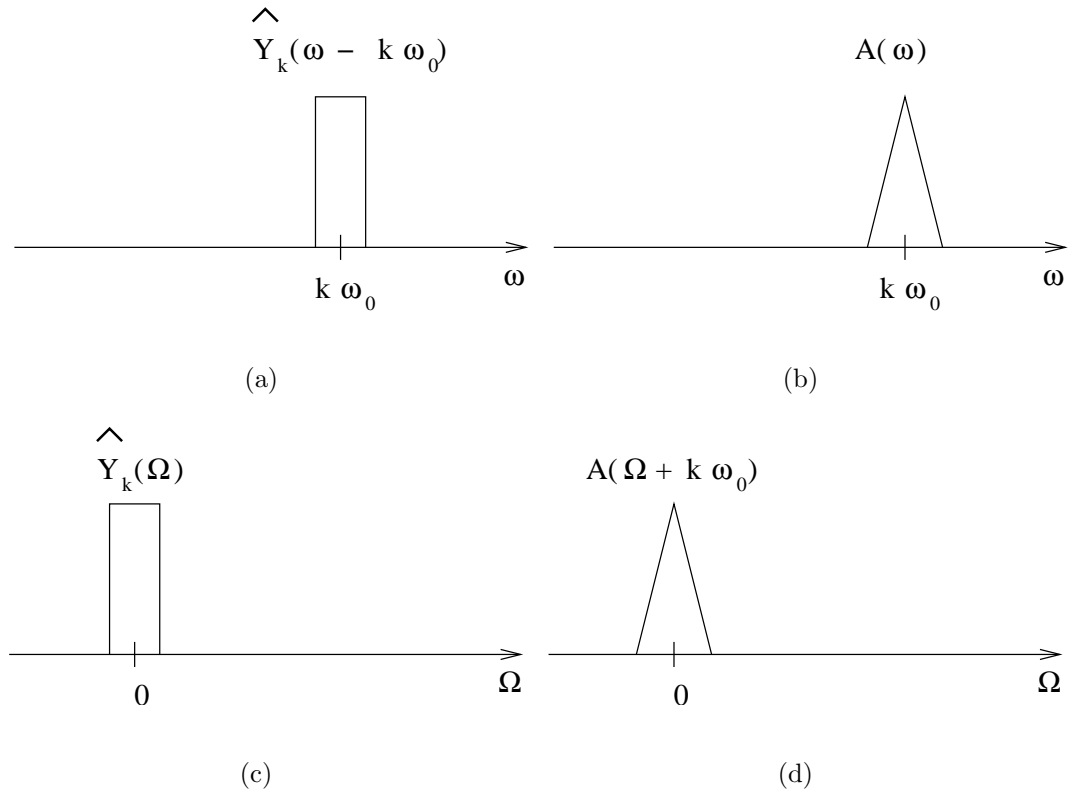


Figure 2.18: (a) spectrum of the electrical variable; (b) its transfer function; (c) down-converted spectrum and (d) down-converted transfer function.

high frequency components to be obtained by computing the circuit equations on the slow time scale as shown in Figure 2.18. The linear transfer function  $A(\Omega + k\omega_0)$  in (2.47) can be expanded in a Taylor series:

$$\begin{aligned} A(\Omega + k\omega_0) &= A(\omega)|_{\omega=k\omega_0} + \Omega \frac{dA(\omega)}{d\omega} \Big|_{\omega=k\omega_0} \\ &+ \frac{\Omega^2}{2} \frac{d^2A(\omega)}{d\omega^2} \Big|_{\omega=k\omega_0} + \dots \end{aligned} \quad (2.48)$$

with the Taylor series expansion for  $B(\Omega + k\omega_0)$  being similar. Plugging the Taylor series of the transfer functions up to the  $q$  th order into (2.40) and taking the inverse Fourier transform, the ET equations are as follows:

$$\begin{aligned} \hat{X}_k(t_1) &= \alpha_{k,0}\hat{Y}_k(t_1) + \beta_{k,0}\hat{G}_k(t_1) \\ &+ \sum_{p=1}^q \left( \alpha_{k,p} \frac{d^p \hat{Y}_k(t_1)}{dt_1^p} + \beta_{k,p} \frac{d^p \hat{G}_k(t_1)}{dt_1^p} \right) \\ 0 &\leq k \leq N \\ y(t_1, t_2) &= f(x(t_1, t_2)). \end{aligned} \tag{2.49}$$

These circuit equations can be solved with a mix of HB and TMS methods. HB analysis is performed at every envelope sample time point and the complex envelopes are obtained by TMS on the  $t_1$  scale.

## 2.5 Summary

Memory effects of RF systems were investigated and a new classification of memory effects was introduced for the purpose of behavioral modeling strategy. According to the new classification memory effects were divided into nonlinear RF effects and nonlinear baseband effects. This classification was done considering presently available and relatively simple measurement methods, which were single-tone test using a network analyzer and complex-envelope measurement using a vector signal analyzer. Nonlinear RF effects and nonlinear baseband effects could be indirectly measured using the two measurement methods. Dividing memory effects as such will establish the basis for an extraction strategy of a multi-slice behavioral model being discussed in Chapter 3 as well as a strategy to measure baseband effects.

Reviewed in Section 2.3 were three behavioral models: a memoryless model; a memory polynomial model; and the Wiener-Hammerstein model. These models were representative models among various behavioral models reported. A memoryless model was the simplest one in modeling of nonlinear communication systems so the mechanism of nonlinear distortion could be easily understood by studying it. A mem-

ory polynomial model was one of the rare models that could capture baseband effects. However it could not capture baseband effects systemically and rigorously. Thus the performance of the model was questionable. The Wiener-Hammerstein model was known to capture memory effects but it could only capture short-term memory effects. Reviewing these behavioral models will help to understand the structure of a multi-slice behavioral model and the mechanism to systemically capture memory effects with it. The Wiener-Hammerstein model will be utilized later in multi-slice behavioral modeling.

Reviewed in Section 2.4 were three circuit simulation techniques: transient; harmonic balance; and envelope transient. Transient and harmonic balance were briefly reviewed since these techniques were utilized in envelope transient. Envelope transient was thoroughly reviewed since it could simulate RF circuits excited with digitally-modulated signals and capture baseband effects. Thus it could be used in capturing baseband effects of multichannel communication systems. The mechanism of capturing baseband effects was not clear in the conventional envelope transient so it will be clarified in Chapter 4. Also, the conventional envelope transient will be extended to multichannel envelope transient that can handle multichannel digitally modulated signals. A multi-slice behavioral model will be used in multichannel envelope transient simulation and transient simulation in Chapter 5.

## Chapter 3

# Multi-Slice Behavioral Model

### 3.1 Introduction

As a preliminary step toward capturing baseband effects (or electrical long-term memory effects) in multichannel communication systems, a multi-slice behavioral model is developed that captures baseband memory effects of a single-channel power amplifier. This work is described by the author in [48]. The model consists of two slices and systemically captures baseband effects of an RF system. The first slice of the model is a static nonlinear function (an odd-order polynomial having complex coefficient), which captures memoryless nonlinearities of an RF system. The second slice consists of a static nonlinear function (an even-order polynomial), a frequency-domain baseband filter and an ideal mixer. The static nonlinear function is used to produce baseband products and the frequency-domain baseband filter is used to shape the baseband products. And then the output of the baseband filter is up-converted to the fundamental frequency band by a mixer to account for baseband effects. The first and the second slice of the model are respectively extracted using measurements with a single tone and a single-channel WCDMA signal. The measurements are in the form of complex envelope so they are easy to obtain using a vector signal analyzer. The

parameters of the model are extracted by directly comparing with the measurements.

In Section 3.2, the specific model architecture is described and how the model captures baseband effects is discussed. In Section 3.3, a procedure for experimentally characterizing a system and extracting the model is presented. In Section 3.4, a commercial power amplifier and a WCDMA signal are used to extract the multi-slice model. The work is validated by comparing measured and modeled results.

## 3.2 Model Architecture

For single-channel applications, a multi-slice behavioral model was developed to capture baseband memory effects that are important in capturing the nonlinear behavior of power amplifiers. Two slices are used for simplicity although the multi-slice model, Figure 3.1, can be extended to cover additional operational behavior. Any

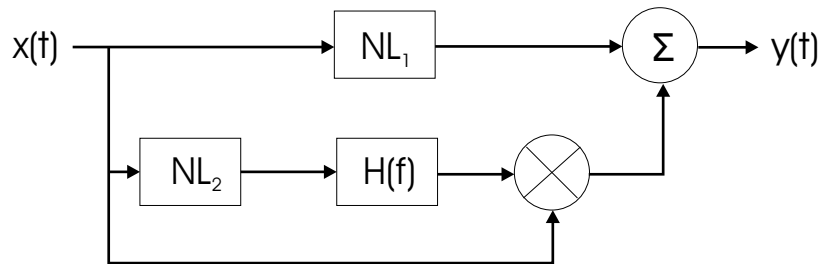


Figure 3.1: A two-slice nonlinear system behavioral model.

form of a behavioral model can be used in each slice. In this work and referring to Figure 3.1, the first slice is represented by an odd-order polynomial having complex coefficients and capturing memoryless contributions to the fundamental response. The second slice consists of a static nonlinear function, a linear frequency domain filter,  $H(f)$ , and an ideal mixer. The static nonlinear function is represented by an even-order polynomial with complex coefficients. In effect the nonlinearity in the second slice generates baseband frequency components. The linear filter in the second slice appropriately shapes the spectrum of baseband produced by the even-order

nonlinearity and the ideal mixer up-converts the output of  $H(f)$  to the fundamental. Hence, the second slice accounts for baseband memory effects that cause asymmetric spectral regrowth.

### 3.3 Extraction Procedure

The measurement and extraction procedure for the odd-order polynomial coefficients in the first slice is the same as that described in Subsection 2.3.1. Thus the first slice captures the AM-AM and AM-PM characteristics of a system. To obtain an accurate memoryless model, it is important to extract low-order coefficients as accurately as possible. This is particularly true for first-order and third-order coefficients, which are generally extracted from measured  $S_{21}$  when input amplitude is low. Since the dynamic range of a network analyzer is limited, the measured  $S_{21}$  data tends to be unreliable. Imprecision is particularly evident for the phase response as it includes a lot of noise when the signal levels are low. It was found that the effect of noise can be removed by averaging multiple measurements. Measurements required for extraction of the second slice were collected using a vector signal analyzer. In this case the input is a single-channel digitally-modulated signal whose bandwidth is equal to the bandwidth of the baseband circuit. When the power of the input is low enough that the third-order nonlinearity is dominant, the output complex envelope at the fundamental is measured to extract the coefficient of  $x^2(t)$  and  $H(f)$ . This measured output includes distortions caused by memoryless nonlinearities and long-term memory effects if it is assumed that short-term memory effects are negligibly small due to the bandwidth of the single-channel input. If we remove the distortions caused by the memoryless nonlinearities from the measured output, then the result will only have the distortions caused by the long-term memory effects. Hence, the post-processed result is treated as the measured output for the extraction. As shown in Figure 3.2, the response required in extraction is obtained by subtracting the modeled output of the first slice from the measured response to the digitally-modulated input. Thus baseband effects in the post-processed data are caused by

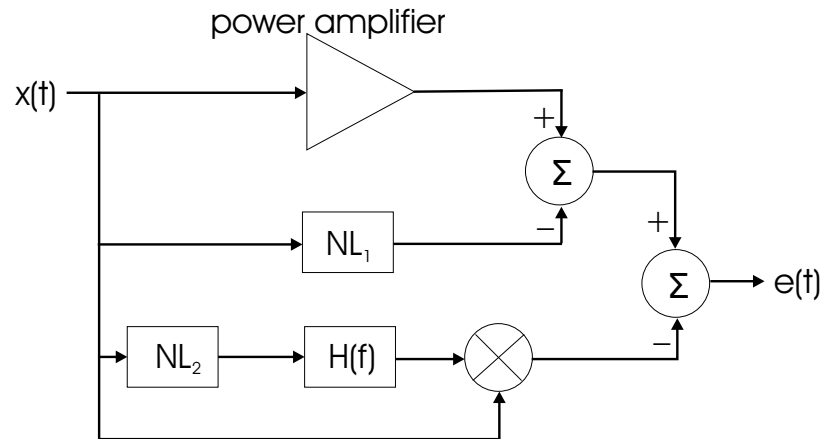


Figure 3.2: A block diagram showing extraction procedure of the two-slice nonlinear system behavioral model.

the second-order nonlinearity so the first block of the second slice is set to  $x^2(t)$  and  $H(f)$  becomes the only unknown block left to be extracted.  $H(f)$  is just a transfer function relating the input and output of  $H(f)$  and is obtained by direct computation. Conversion between the time domain and the frequency domain is done by the Fourier transform. Following extraction of  $H(f)$ , it is normalized and the coefficient of  $x^2(t)$  is adjusted accordingly. Strictly speaking, the complex coefficient extracted for the even-order polynomial nonlinear model of the second slice models a complex gain block and simplifies the model structure. Higher-order nonlinear baseband effects are modeled from data obtained by sweeping amplitude of the input signal and measuring the output response using the extraction procedure described above. Now however, since  $H(f)$  is already determined, higher-order coefficients of the even-order polynomial are extracted.

### 3.4 Verification

A gallium arsenide (GaAs) hetero-junction bipolar transistor (HBT) power amplifier (RF Micro Devices model RF5117) designed for wireless local area network (WLAN) applications was used to extract parameters of the multi-slice model. Gain

of the amplifier was around 25 dB at 2.5 GHz. The nonlinear block in the first slice was extracted from the single-tone AM-AM and AM-PM characteristics at the carrier frequency (2.5 GHz) and fitted to a 17 th-order odd-order complex polynomial. The measured and modelled characteristics are almost identical as seen in Figures 3.3 and 3.4. Initially two-tone testing was used to extract the model of the second slice. It

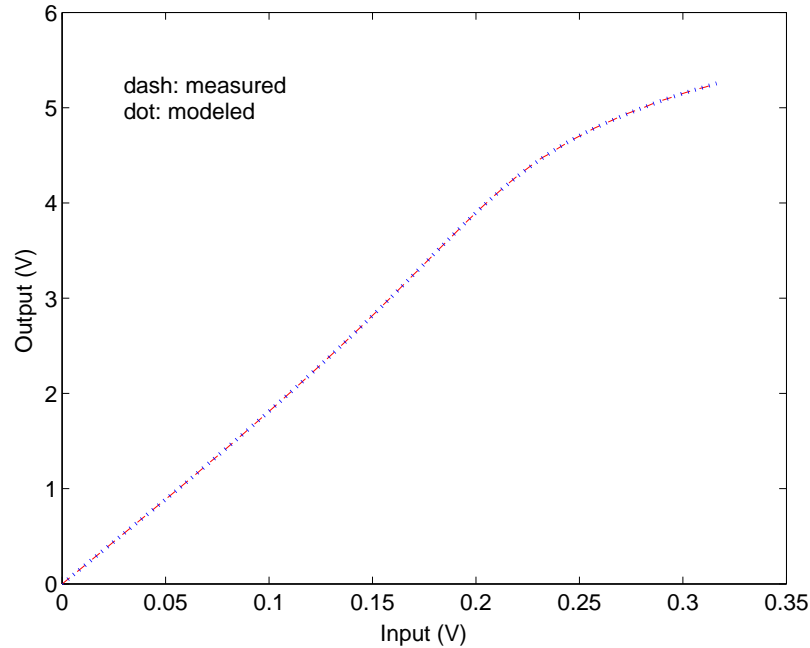


Figure 3.3: Measured and modelled AM-AM characteristics of the amplifier at 2.5 GHz. (The measured and modelled characteristics overlap.)

was found that a precise model could not be easily obtained even if the frequency separation of the two tones was swept. This is attributed to accumulated errors in the difference technique used in extracting the second-slice data. However a reliable model could be extracted using a digitally-modulated signal. The second slice was successfully extracted by comparing the response to a digitally-modulated input signal to that calculated by the first-slice alone. In particular, a Wideband Code Division Multiple Access (WCDMA) down-link signal was used and the response is measured by a Vector Signal Analyzer (VSA: Agilent Model 89600S). An input power level of  $-11$  dBm was chosen for initial extraction of the second slice model as at this power level nonlinear response is significant. The difference between the measured

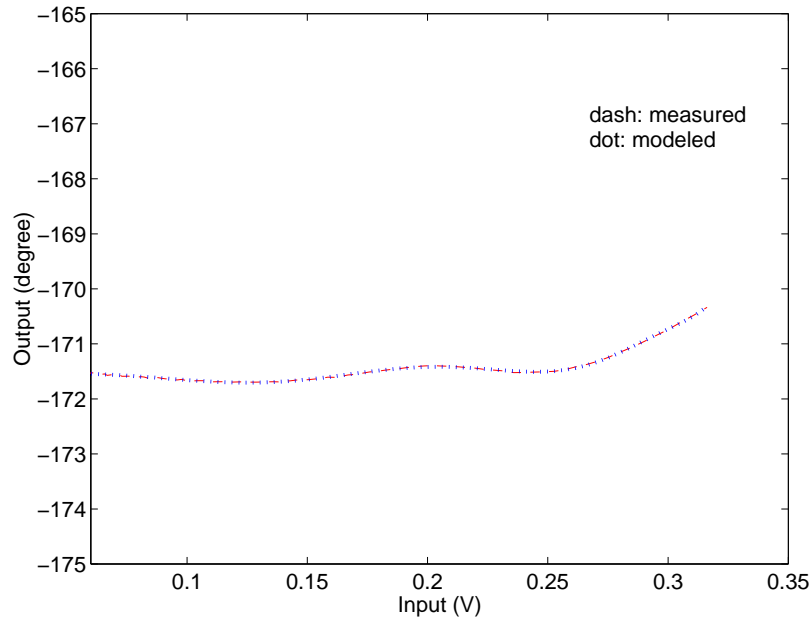


Figure 3.4: Measured and modelled AM-PM characteristics of the amplifier at 2.5 GHz. (The measured and modelled characteristics overlap.)

response and that modelled by the first slice leads to the baseband transfer function response,  $H(f)$ , shown in Figures 3.5 and 3.6. The baseband nonlinear behavior, captured by  $NL_2$ , was obtained from the measurements of the response to the WCDMA signal swept in amplitude and fitted to an even-order complex polynomial. Note the approximate odd symmetry in the phase response of  $H(f)$  in Figure 3.6. This leads to an approximate conjugate relationship between lower-side and upper-side intermodulation products resulting from baseband effects. Note that the extracted  $H(f)$  transfer function (Figures 3.5 and 3.6) are not fully physical since the transfer characteristics of the amplitude and phase fluctuations are not realistic and they are not precisely conjugate. This is a result of the extraction being based on measurements of the response to a digitally-modulated signal. However this model faithfully models behavior over a range of power levels.  $H(f)$  can be extracted in other ways using, for example, the two-tone equivalent of AM-AM and AM-PM characterizations over a range of tone separations. In Section 5.2, another extraction method will be introduced to produce a realistic  $H(f)$  using two-tone IM3 amplitude measurements as well as complex-envelope measurements. Modelled results are compared with mea-

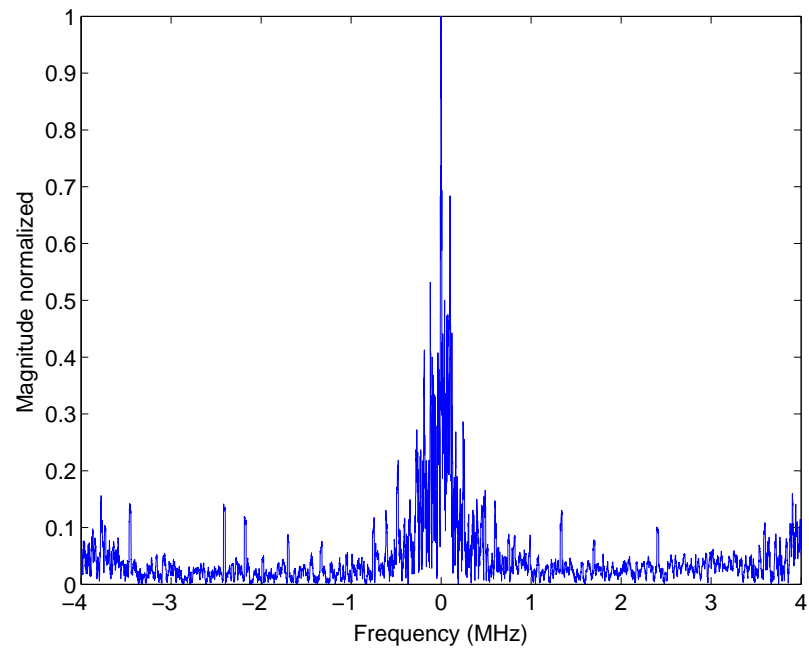


Figure 3.5: Normalized magnitude of  $H(f)$  which is used directly in the model.

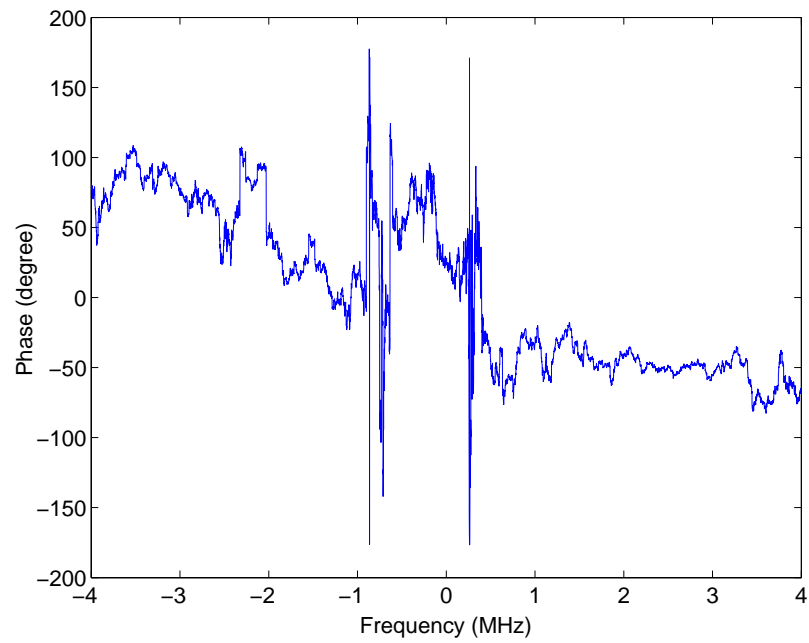


Figure 3.6: Modelled phase characteristics of  $H(f)$  which is used directly in the model.

measurements in Figure 3.7. They agree very well where input power is swept from  $-11$

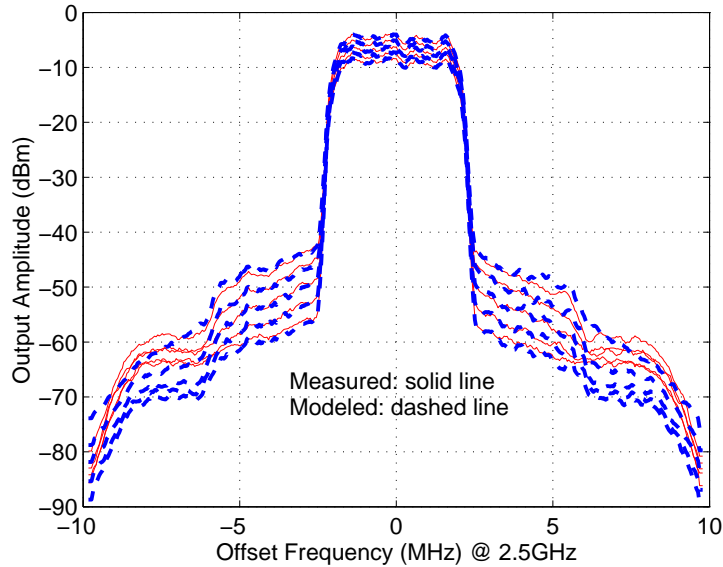


Figure 3.7: Measured and modelled output frequency spectra of the WLAN amplifier.

to  $-7$  dBm. The averaged discrepancy of the spectral regrowth is computed as

$$E = \frac{\sum_{f=1}^N |P(f)_{meas} - P(f)_{mod}|}{N} \quad (3.1)$$

where  $P(f)_{meas}$  and  $P(f)_{mod}$  are respectively measured and modeled values of power at a discrete frequency  $f$ . The resulting error as a function of input is depicted in Figure 3.8. To visualize asymmetric spectral regrowth, the data in Figure 3.7 is re-plotted on an expanded scale in Figure 3.9. About 2 dB of asymmetry is observed in the lower and upper spectral regrowth response. The measured and modeled asymmetries are computed and compared in Figure 3.10. Discrepancies of the noise level at the far sides of the channel in Figure 3.9 are originated from the input signal to the model. The input signal is measured several times and averaged to lower the noise level. This solves the dynamic range problem of a vector signal analyzer when an input level is low. Thus the noise level of modeled output is different from that of the measured output that is not averaged.

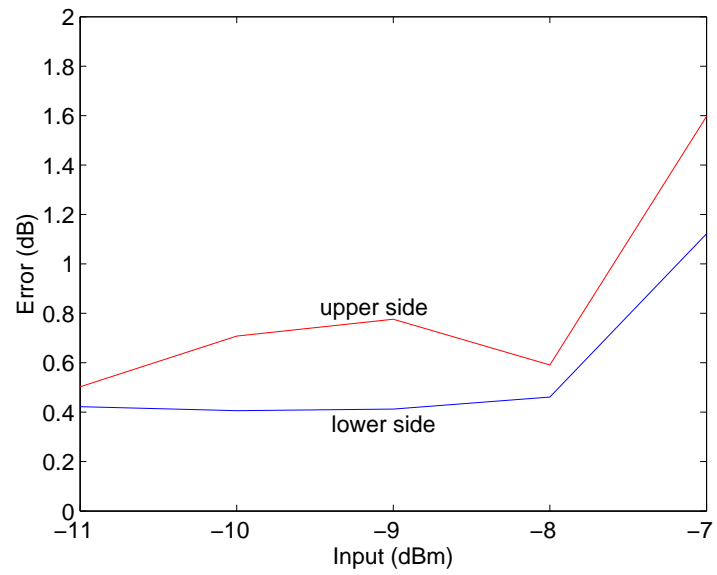


Figure 3.8: Error computed between measured and modelled spectral regrowth.

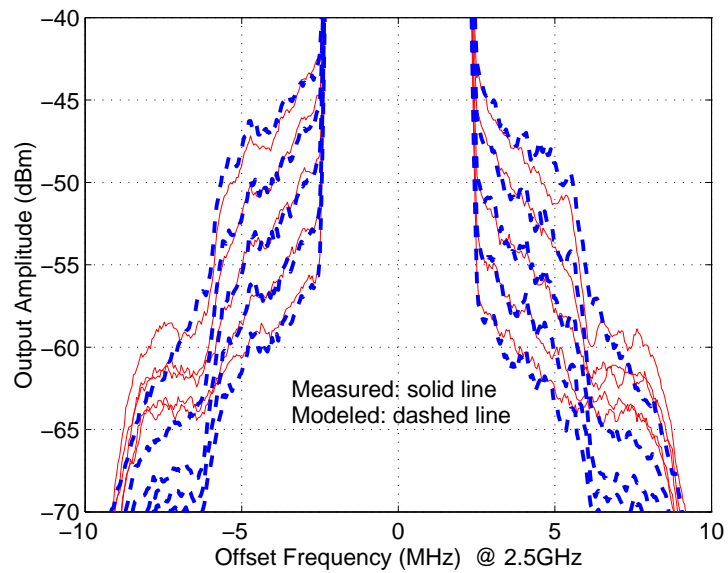


Figure 3.9: Expansion of Figure 3.7 with clearer depiction of spectral regrowth asymmetry and comparison of the modeled and measured results.

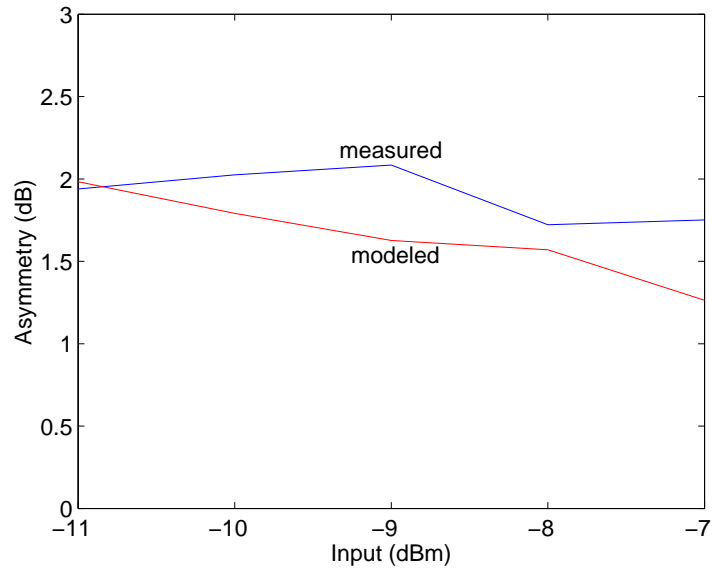


Figure 3.10: Asymmetries of measured and modelled spectral regrowth.

The measured and modelled time-domain envelope responses are compared in Figs. 3.11 and 3.12. Two modelled characteristics are shown with one being the response from the first slice only (being a memoryless model) and the multi-slice model (with baseband memory). The multi-slice model response (with 0.59 % error) is much closer to the measured response than the response of the memoryless model (with 1.37 % error); however the discrepancies are not very clear in the time domain since the level of the spectral regrowth is as low as  $-45$  dBc. This comparison is more vividly seen in the frequency domain as shown in Figure 3.13. The memoryless model (first slice only) accurately captures the response in the main channel but not in the lower and upper channel regions. The memory model (model with both slices) faithfully captures the adjacent channel response. Discrepancies between the measured and modeled spectral regrowth are computed and shown in Table 3.1.

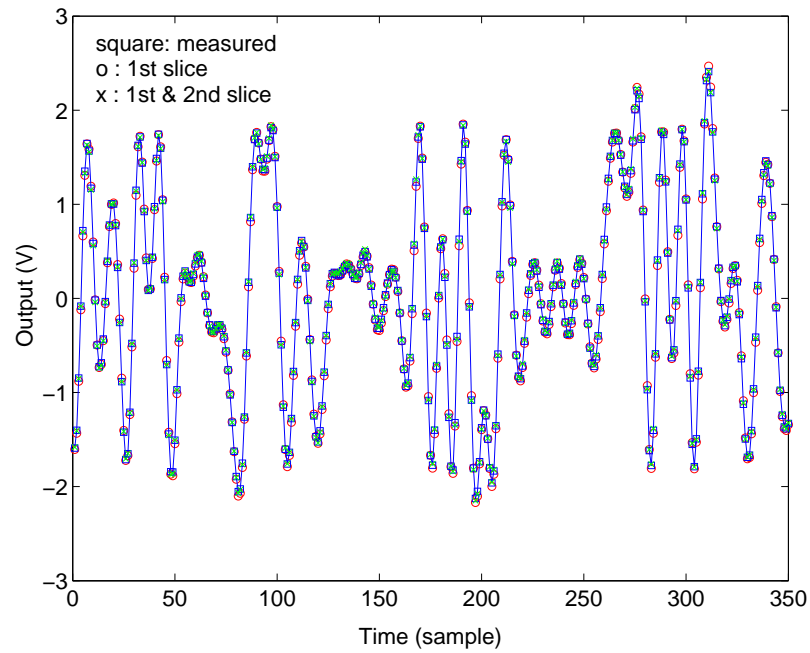


Figure 3.11: Real part of the modelled and measured output complex envelopes in the time domain.

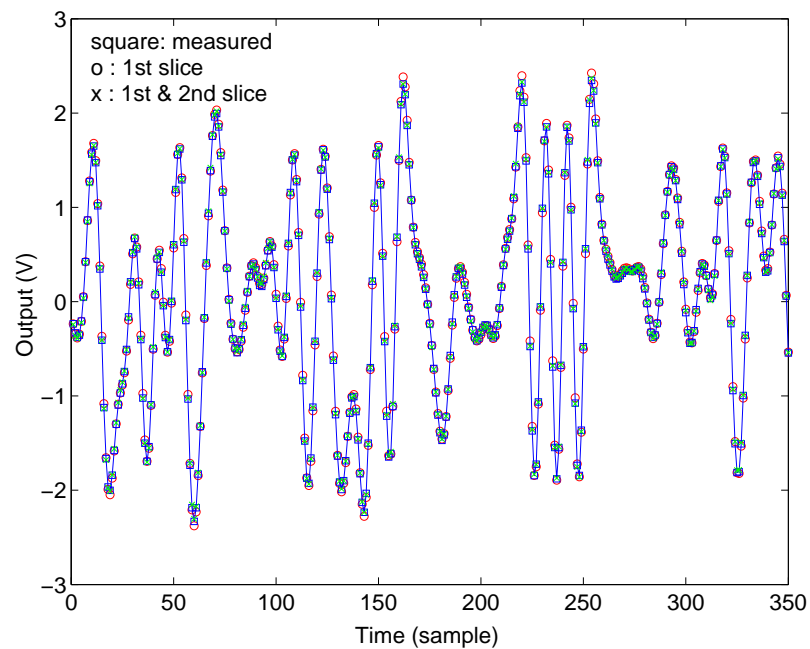


Figure 3.12: Imaginary part of the modelled and measured output complex envelopes in the time domain.

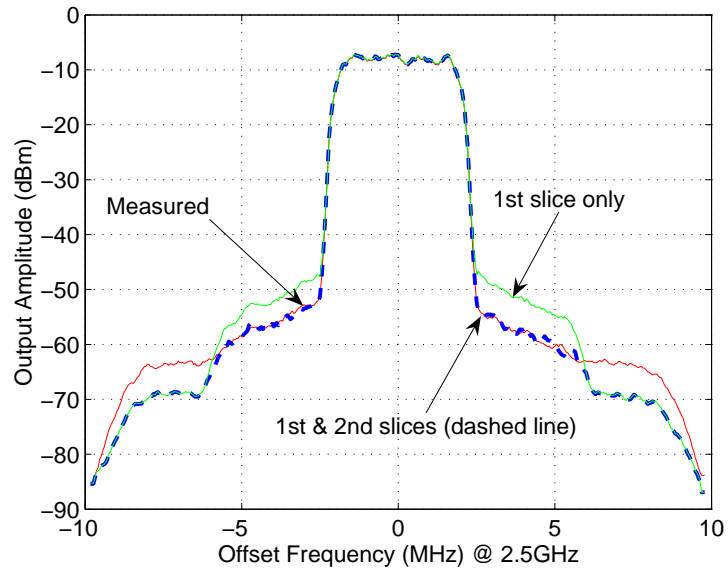


Figure 3.13: Output frequency spectra of the model with and without memory, and measurements.

Table 3.1: Discrepancies (in dB) between the measured and modeled spectral regrowth.

	memory model	memoryless model
lower channel	0.42	4.14
upper channel	0.50	6.03

### 3.5 Summary

A multi-slice behavioral model was used to capture baseband effects of a single-channel power amplifier. An odd-order polynomial in the first slice of the model was extracted from single-tone measurements. After extracting the first slice, the second slice was extracted from complex-envelope measurements with a single-channel WCDMA signal. A new approach in this chapter was using a complex envelope of a digitally-modulated signal to extract a baseband filter in the second slice of the model. A complex envelope of a digitally-modulated signal could be measured easily using a vector signal analyzer. This greatly simplified measurement to extract the baseband compared to using a two-tone signal. If we used a two-tone signal to extract the baseband filter, we would need to measure AM-AM and AM-PM responses over the operating frequency band, or amplitude and phase responses of the third-order intermodulation products while sweeping the amplitudes and the frequency separation of the two tones. This would take tremendous effort and time. The modeled results were compared and agreed well with WCDMA measurements over a range of power levels. Especially asymmetric spectral regrowth as low as  $-45$  dBc was accurately modeled. Shown in this chapter was that not only the multi-slice model captured baseband effects accurately but also it was extracted conveniently using a complex envelope.

One of the disadvantages of the extraction was that the transfer characteristics of the extracted baseband filter was not smooth as shown in Figure 3.5 and 3.6. Due to this property, the extracted model was restricted to the type of an input signal and was not compatible with other type of a signal such as discrete tones. The disadvantage came from direct computation of the baseband filter by using a complex envelope. Nevertheless, using a complex-envelope signal to extract the baseband filter was very convenient and the resulting multi-slice model was able to accurately capture baseband effects of an RF system. The problem of the non-smooth baseband filter will be solved in Chapter 5. Also, the multi-slice model will be extended for multichannel applications in Chapter 5.

## Chapter 4

# Multichannel Envelope Transient Analysis

### 4.1 Introduction

An Envelope Transient analysis for multichannel applications [42]–[43] was theoretically formulated in Section 4.1. Various applications of the analysis can be found in [44]–[47]. In the analysis, each individual channel is treated separately to achieve better computational efficiency. In Section 4.2, formulation for circuit elements R, L and C are constructed in the modified Nodal admittance matrix form to build a simulator. In the patent document [7], one of the original documents describing envelope transient analysis, the linear circuit response is captured by its impulse response. In this chapter the analysis is generalized to handle arbitrarily complex baseband circuitry described using circuit elements or by the multi-slice model introduced in the previous chapter. To complete the development an error function is formulated to enable iterative circuit simulation. In Section 4.3, it is shown that the envelope transient method can capture memory effects, especially baseband effects. Derivatives of

the envelope transient equations around DC take baseband effects into account. As a further illustration of capturing baseband effects, the envelope transient analysis is compared to a sequence of HB analyses with time-varying phasors in Section 4.4. The difference between the two analyses is inclusion of long time-constant derivatives in envelope transient analysis that are not included in HB analysis. Finally a multi-channel envelope transient analysis is compared to a single-channel envelope transient analysis in Section 4.5. The impact on computational efficiency using multichannel envelope transient analysis is demonstrated when channels are separated widely.

## 4.2 Theoretical Formulation

A two-channel digitally-modulated signal can be generally expressed in the following form

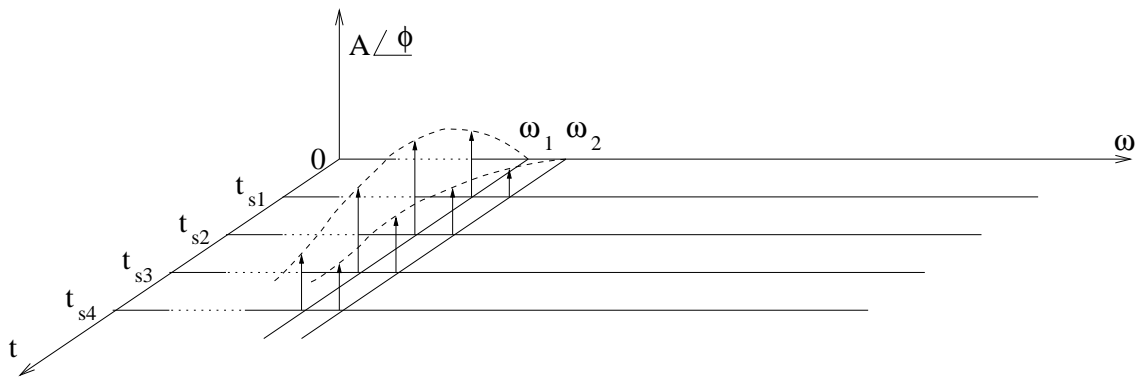
$$z(t) = \text{Re} \left[ \hat{Z}_1(t)e^{j\omega_1 t} + \hat{Z}_2(t)e^{j\omega_2 t} \right] \quad (4.1)$$

where  $\hat{Z}_1(t)$  and  $\hat{Z}_2(t)$  represent the complex envelopes corresponding to each carrier frequency,  $\omega_1$  and  $\omega_2$ . This two-channel expression is used for the purpose of simplicity but it can be simply generalized to multi-channel signals. The signal in (4.1) can be viewed as comprising two time-varying tones. The spectrum of the signals in a nonlinear circuit with an input  $g(t)$  (of the form of (4.1)) is shown in Figure 4.1. The waveforms in the circuit have the general forms:

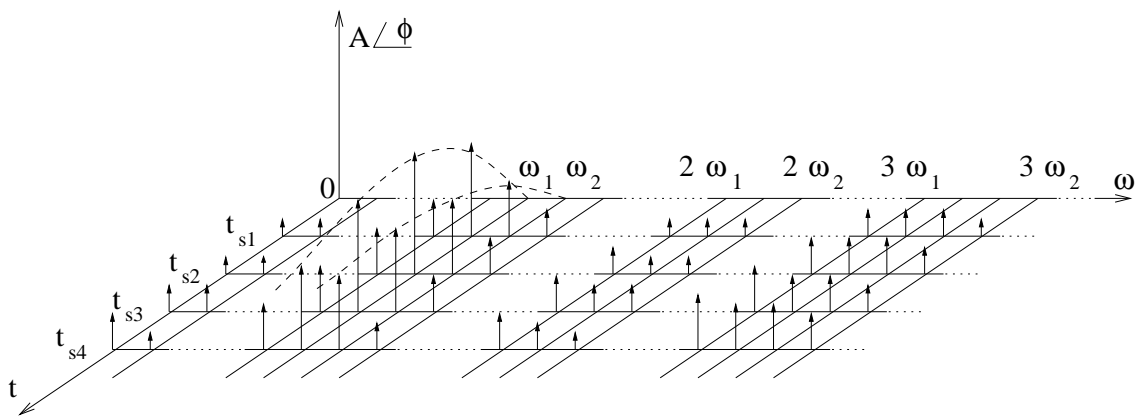
$$x(t) = \text{Re} \left[ \sum_{m,n=-k}^k \hat{X}_{m,n}(t)e^{j(m\omega_1+n\omega_2)t} \right] \quad (4.2)$$

where  $m\omega_1 + n\omega_2 \geq 0$ , and  $m$  and  $n$  are frequency indices. Now denote  $g(t)$  as the two-channel source, and  $x(t)$  and  $y(t)$  as circuit waveforms. The frequency-domain relationship of these signals is defined in (2.40). Applying the same procedures used with Single Envelope Transient (SET), the linear circuit equation of Multi Envelope Transient (MET) is obtained as follows:

$$\hat{X}_{m,n}(t_1) = \alpha_{m,n,0}\hat{Y}_{m,n}(t_1) + \beta_{m,n,0}\hat{G}_{m,n}(t_1) \quad (4.3)$$



(a)



(b)

Figure 4.1: Input and output of a nonlinear system in the complex envelope expression view: (a) time-varying input signal; and (b) time-varying internal and output signals.

$$\begin{aligned}
& + \sum_{p=1}^q \left( \alpha_{m,n,p} \frac{d^p \hat{Y}_{m,n}(t_1)}{dt_1^p} \right. \\
& \left. + \beta_{m,n,p} \frac{d^p \hat{G}_{m,n}(t_1)}{dt_1^p} \right)
\end{aligned}$$

where  $m$  and  $n$  are chosen in the manner of  $m\omega_1 + n\omega_2 \geq 0$ ; The source envelope,  $\hat{G}_{m,n}(t_1)$  is non zero only at fundamental frequencies and/or DC, otherwise it is zero. The nonlinear subcircuit is computed in the time domain as in SET.

The spectra of the signals in the nonlinear system are presented in Figure 4.2 with each of the spectral bands having the same bandwidth BW. The bandwidth must be chosen to encompass the expected regrowth but with the restriction that the spectral bands do not overlap.

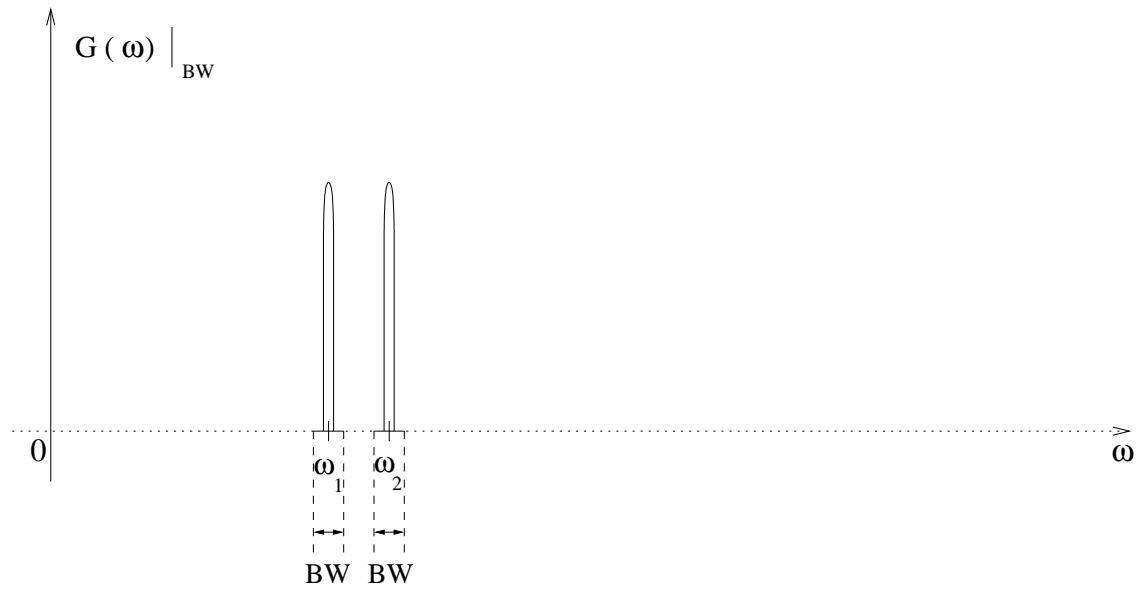
### 4.3 Formulation for Circuit Simulation

In formulating the network equations using KCL and KVL as required in circuit simulation, linear device stamps for constructing the Modified Nodal Admittance Matrices (MNA) are required. The stamp of the linear resistor can be written in the following form

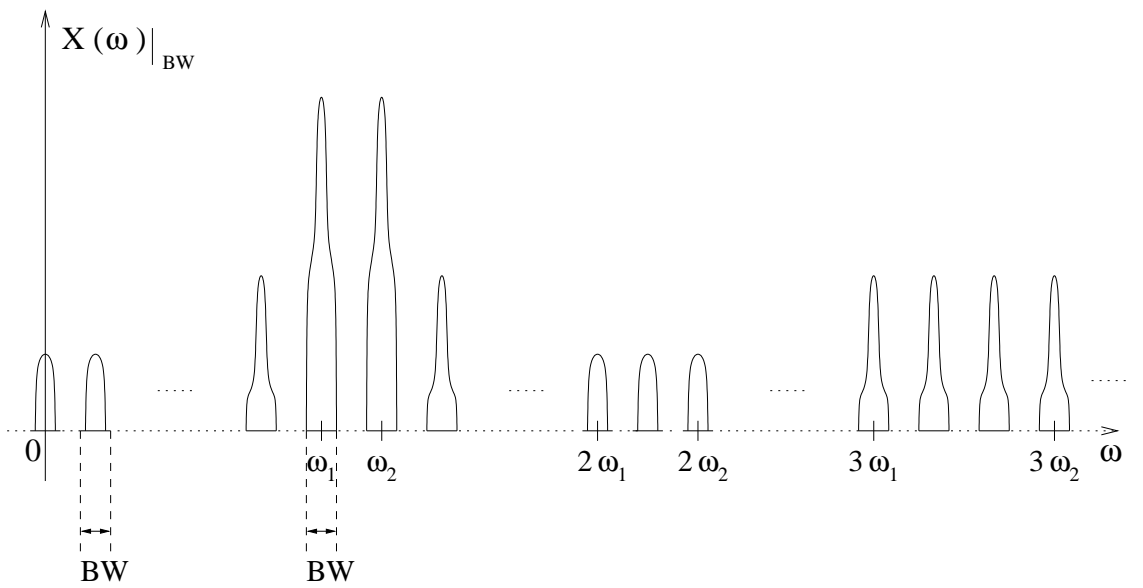
$$\begin{pmatrix} G & -G \\ -G & G \end{pmatrix} \begin{pmatrix} \hat{V}_{m,n}^i(t) \\ \hat{V}_{m,n}^j(t) \end{pmatrix} = 0 \quad (4.4)$$

where  $\hat{V}(t)$  is the resistor terminal voltage in complex envelope and  $G = 1/R$ . The frequency indices are  $m$  and  $n$ . Superscripts of  $\hat{V}(t)$  represent terminal indices. The linear capacitor stamp can be formulated as follows

$$\begin{aligned}
& \begin{pmatrix} j(m\omega_1 + n\omega_2)C & -j(m\omega_1 + n\omega_2)C \\ -j(m\omega_1 + n\omega_2)C & j(m\omega_1 + n\omega_2)C \end{pmatrix} \begin{pmatrix} \hat{V}_{m,n}^i(t) \\ \hat{V}_{m,n}^j(t) \end{pmatrix} \\
& + \begin{pmatrix} C & -C \\ -C & C \end{pmatrix} \begin{pmatrix} \frac{d\hat{V}_{m,n}^i(t)}{dt} \\ \frac{d\hat{V}_{m,n}^j(t)}{dt} \end{pmatrix} = 0 \quad (4.5)
\end{aligned}$$



(a)



(b)

Figure 4.2: Spectrum of signals in a nonlinear system considered in MET analysis: (a) spectra of source signals; and (b) spectra of internal circuit and output signals.

Similarly, the linear inductor stamp can be formulated as

$$\begin{aligned} & \begin{pmatrix} 0 & 0 & 1 \\ 0 & 0 & -1 \\ 1 & -1 & -j(m\omega_1 + n\omega_2)L \end{pmatrix} \begin{pmatrix} \hat{V}_{m,n}^i(t) \\ \hat{V}_{m,n}^j(t) \\ \hat{I}_{m,n}(t) \end{pmatrix} \\ & + \begin{pmatrix} 0 & 0 & 0 \\ 0 & 0 & 0 \\ 0 & 0 & -L \end{pmatrix} \begin{pmatrix} \frac{d\hat{V}_{m,n}^i(t)}{dt} \\ \frac{d\hat{V}_{m,n}^j(t)}{dt} \\ \frac{d\hat{I}_{m,n}(t)}{dt} \end{pmatrix} = 0 \end{aligned} \quad (4.6)$$

where the direction of  $\hat{I}_{m,n}(t)$  is from terminal i to terminal j. As is normal in HB analysis, a circuit is partitioned into linear and nonlinear sub-circuits with the linear portion described by a MNAM. A circuit so partitioned can be described in MET by

$$\hat{\mathbf{G}}_{m,n} \hat{\mathbf{u}}_{m,n}(t) + \mathbf{C} \frac{d\hat{\mathbf{u}}_{m,n}(t)}{dt} = \hat{\mathbf{s}}_{m,n}^f(t) + \mathbf{T}^T \hat{\mathbf{i}}_{m,n}^{\text{NL}}(t) \quad (4.7)$$

where  $\hat{\mathbf{G}}$  and  $\mathbf{C}$  are submatrices of the MNAM. The other quantities  $\hat{\mathbf{u}}$ ,  $\hat{\mathbf{s}}^f$ ,  $\mathbf{T}^T$  and  $\hat{\mathbf{i}}^{\text{NL}}$  are terminal voltages and required currents in the linear subcircuit, independent sources, a transposed incidence matrix and contribution from the nonlinear subcircuit respectively. All of these are in the envelope domain with  $t$  being time referred to the baseband. As required in transient analysis, the derivative vector in (4.7) is discretized using

$$\frac{d\hat{\mathbf{u}}_{m,n}(t_k)}{dt} = a\hat{\mathbf{u}}_{m,n}(t_k) + \hat{\mathbf{b}}_{m,n}(t_{k-1}) \quad (4.8)$$

and the subcircuits are balanced by setting

$$\hat{\mathbf{v}}_{m,n}^{\text{NL}}(t_k) = \mathbf{T} \hat{\mathbf{u}}_{m,n}(t_k), \quad (4.9)$$

where  $\hat{\mathbf{v}}_{m,n}^{\text{NL}}$  is the terminal voltage vector of the nonlinear subcircuit. Combining the above results we have the following matrix error function:

$$\begin{aligned} \mathbf{f}_{m,n}(\hat{x}(t_k)) &= \mathbf{T} \mathbf{u}_{m,n}(t_k) - \mathbf{v}_{m,n}^{\text{NL}}(t_k) \\ &= \mathbf{T} (\hat{\mathbf{G}}_{m,n} + a\mathbf{C})^{-1} \left( \hat{\mathbf{s}}_{m,n}^f(t_k) \right. \\ &\quad \left. + \mathbf{T}^T \hat{\mathbf{i}}_{m,n}^{\text{NL}}(\hat{x}(t_k)) - \mathbf{C} \hat{\mathbf{b}}_{m,n}(t_{k-1}) \right) \\ &\quad - \hat{\mathbf{v}}_{m,n}^{\text{NL}}(\hat{x}(t_k)) = \mathbf{0} \end{aligned} \quad (4.10)$$

where  $\hat{x}$  is the vector of state variables. Simulation proceeds by setting the above error function to zero at each time step.

## 4.4 Baseband Effects

Baseband (low frequency or long time constant) impedance effects are captured by the linear transfer function  $A(\Omega + k\omega_0)$  and  $B(\Omega + k\omega_0)$  in (2.47). As an example, the component of the transfer function of a linear capacitor (with which an admittance description is used) is represented, without approximation, as

$$A(\Omega + k\omega_0) = jk\omega_0 C + j\Omega C. \quad (4.11)$$

This is just the constitutive relation of the linear capacitor in ET. The inverse Fourier transform of (2.40) combined with (4.11) is then

$$\hat{I}_k(t_1) = jk\omega_0 C \hat{V}_k(t_1) + C \frac{d\hat{V}_k(t_1)}{dt_1} \quad (4.12)$$

where  $t_1$  is the time scale of the complex envelope. The derivative term in (4.12) captures the small changes in the relationship between the capacitor current and voltage due to the slow time-varying modulation signal. With a linear inductor an impedance description is used and  $A(\Omega + jk\omega_0) = jk\omega_0 L + j\Omega L$ . Thus the constitutive relation for a linear inductor is:

$$\hat{V}_k(t_1) = jk\omega_0 L \hat{I}_k(t_1) + L \frac{d\hat{I}_k(t_1)}{dt_1}. \quad (4.13)$$

Using the constitutive relations of elementary components, the fully general ET equations are as follows:

$$\begin{aligned} \hat{X}_k(t_1) &= f_1(\hat{Y}_k(t_1), \hat{G}_k(t_1), \frac{d\hat{Y}_k(t_1)}{dt_1}, \frac{d\hat{G}_k(t_1)}{dt_1}, \\ &\quad \frac{d^2\hat{Y}_k(t_1)}{dt_1^2}, \frac{d^2\hat{G}_k(t_1)}{dt_1^2}, \dots) \\ &0 \leq k \leq N \\ y(t_1, t_2) &= f_2(x(t_1, t_2)) \end{aligned} \quad (4.14)$$

where  $f_2$  is the same function as  $f$  in (2.41).

## 4.5 Harmonic Balance vs. Envelope Transient

This is a convenient point to contrast three analysis techniques: a sequence of HB analyses with time-varying phasors; the conventional Single Envelope Transient (SET); and the enhanced Multi Envelope Transient (MET) developed here. A digitally-modulated RF carrier, a single channel, can be viewed as a time sequence of RF phasors. If a single-tone HB solution is performed then the only low-frequency component will be at DC. Thus a sequence of HB solutions will only capture baseband resistive effects. Conventional SET does capture baseband resistive and capacitive effects through the time derivative at the slow time rate, the time derivative in (4.12). The extended MET method here also captures baseband inductive effects provided that a state variable based HB solver is used. ET captures the baseband signal caused by even-order nonlinearity of the nonlinear circuit block. Accurate computation of the baseband signal is especially important as the balancing of the I and Q chains is critical in wireless communication systems. When the amplitude of the baseband signal is relatively large, it can affect other frequency components including fundamentals and harmonics.

A power amplifier designed for the Personal Communications Services band with IS-95 reverse link excitation was modelled using both time-varying HB and SET. This amplifier, PCS\_pamp\_prj, is a part of the example set supplied with the commercial ADS circuit simulator. The modelled performance obtained using time-varying HB and SET are shown in Figure 4.3 with almost identical results obtained. For the time-varying HB and SET to result in the same response, baseband impedance/admittance is either totally resistive or very small (the baseband derivatives are zeros or close to zeros) yet the former is unlikely to be a characteristic of the amplifier. The conclusion is that the long-time derivatives extracted from the amplifier are negligibly small since the only difference between time-varying HB and SET is whether there are derivatives or not. This conclusion was verified by driving the amplifier with two tones separated by 200 kHz with a center frequency of 1.9 GHz. The simulated magnitude differences between lower and upper third order intermodulation (IM3) products are about 0.01 dB as shown in Figure 4.4, that is, there is no significant asymmetry in the

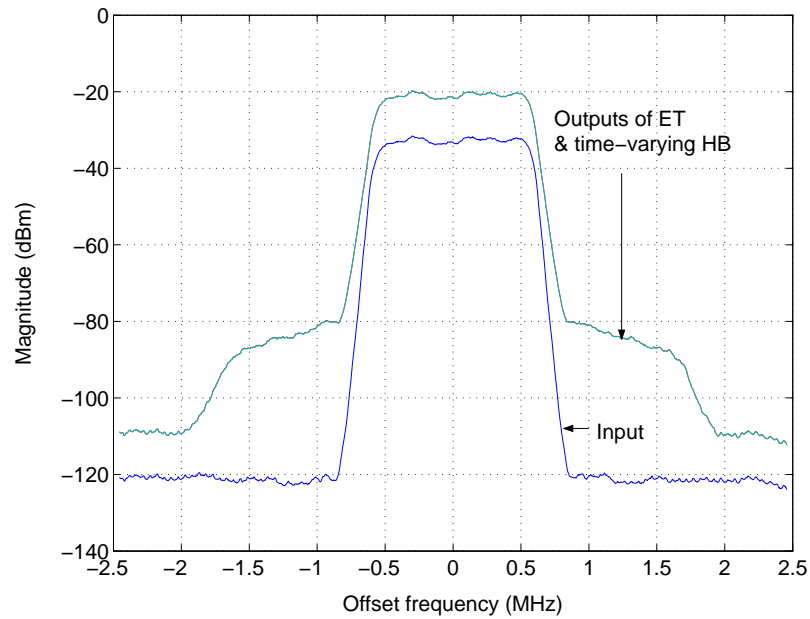


Figure 4.3: Input and output spectra of the PCS amplifier with an IS-95 signal modelled using the time-varying HB and ET method. Center frequency is 1.9 GHz. (The output spectra of the time-varying HB and ET overlap.)

intermodulation responses. Frequency-dependent baseband effects were introduced by modifying the amplifier by changing capacitances and inductances to introduce significant baseband derivatives. Time-varying HB and SET are performed with the modified amplifier. Figure 4.5 presents about 10 dB of difference between the two methods. The lower side has about 1 dB more spectral regrowth than the upper side does as in Figure 4.6. The same two-tone test with the modified amplifier results in about 1 dB difference between lower and upper IM3 at the input level of the IS-95 signal (-5 dBm) for the time-varying HB and ET computation as presented in Figure 4.7, which is directly related to the results in Figure 4.6. These simulations illustrate the importance of using baseband derivatives in full circuit simulation of RF front ends. The circuits used in this section are in Appendix B.

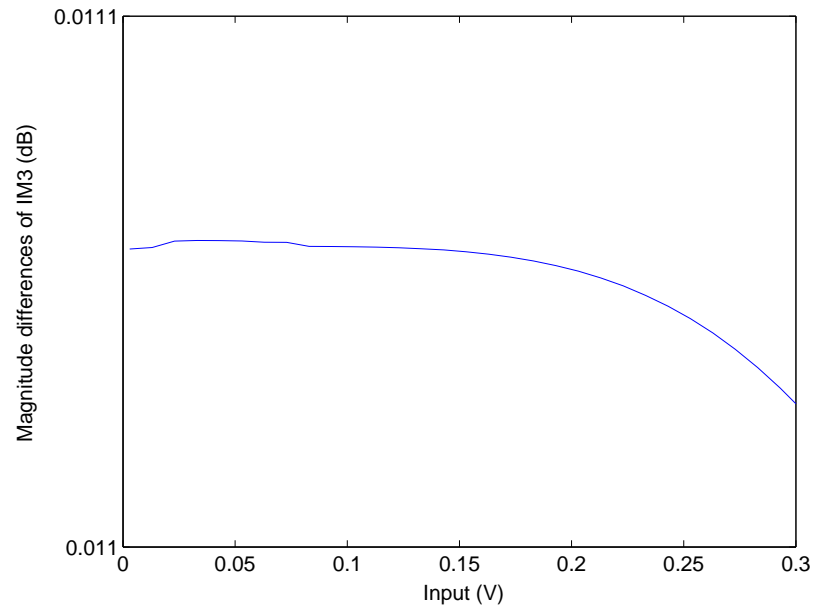


Figure 4.4: Magnitude differences between lower and upper IM3 products of the PCS amplifier with two tones separated by 200 KHz.

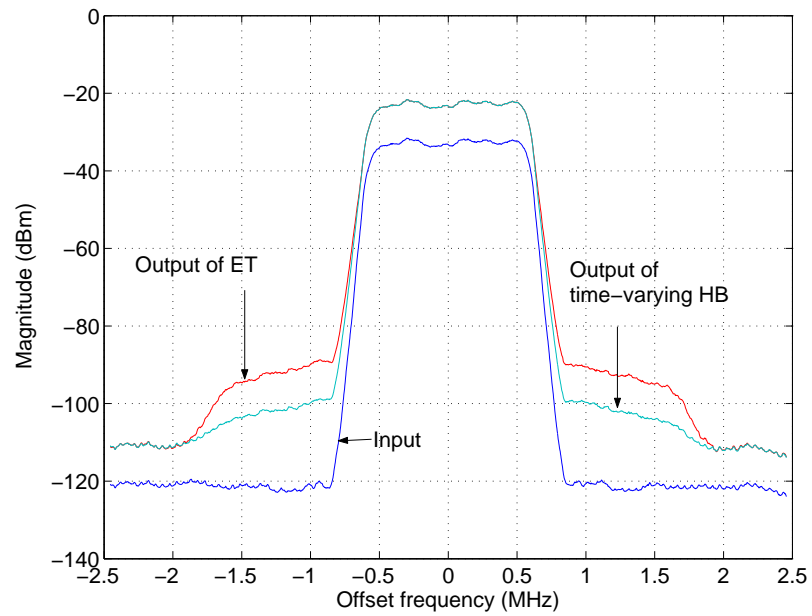


Figure 4.5: Input and output spectra of the modified PCS amplifier with an IS-95 signal modelled using the time-varying HB and ET method. Center frequency is 1.9 GHz.

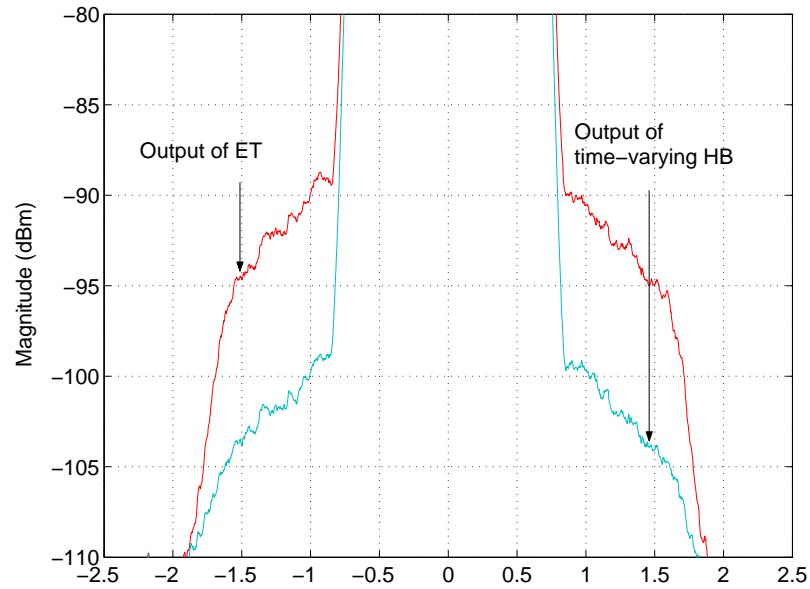


Figure 4.6: Expansion of Figure 4.5 with clearer depiction of spectral regrowth asymmetry.

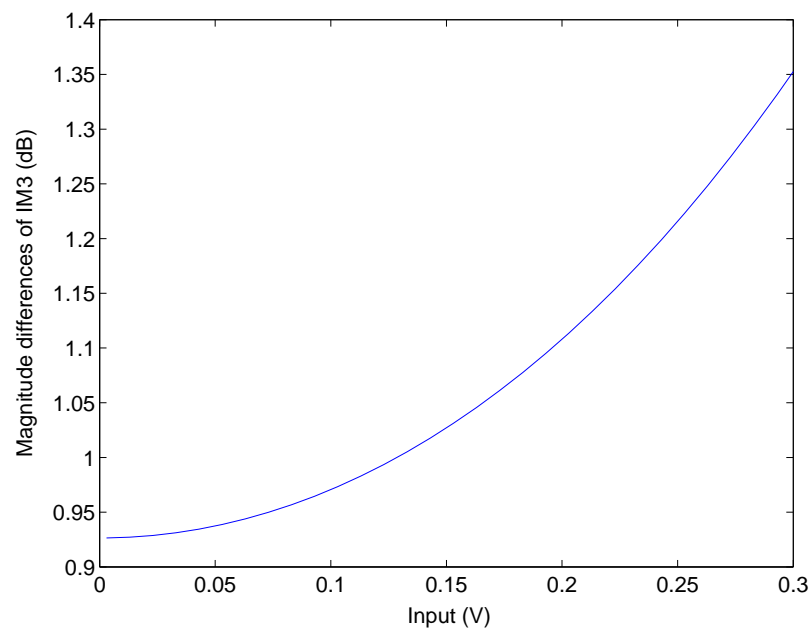


Figure 4.7: Magnitude differences between lower and upper IM3 products of the modified PCS amplifier with two tones separated by 200 KHz.

## 4.6 Single vs. Multi Envelope Transient

A system with a multichannel signal can be simulated using Single Envelope Transient (SET) but the multiple channels must be considered as a single RF carrier with a single envelope. Consequently the envelope bandwidth must be large enough to encompass all channels. Thus computation time using SET increases with increased frequency separation of the channels due to the computation of the spectrum between the channels. However with MET the computation time is independent of channel separation. The simulation time (normalized) of SET and MET is shown in Figure 4.8 for the analysis of the nonlinear amplifier with a two-channel signal. Near quadratic increase of time with SET is observed. In SET the computation time increases because more time points must be considered and more time is required to construct the output spectrum.

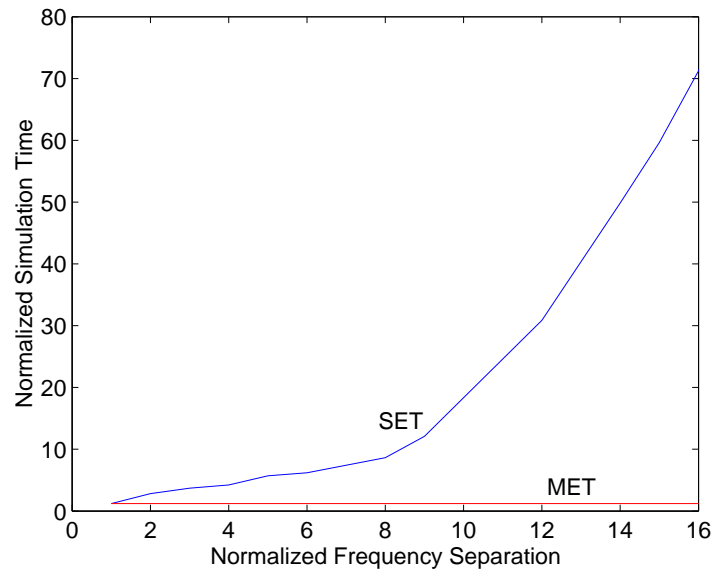


Figure 4.8: Normalized simulation time of SET and MET with respect to channel separation.

This increased computation can be seen when the multi-tone signal is expressed in the form of a signal with a single envelope. The two-tone signal of (4.1) is differently

expressed with a single complex envelope as

$$z(t) = \Re \left[ (\hat{Z}_1(t) e^{j(\frac{\omega_1 - \omega_2}{2})t} + \hat{Z}_2(t) e^{j(\frac{\omega_2 - \omega_1}{2})t}) e^{j(\frac{\omega_1 + \omega_2}{2})t} \right]. \quad (4.15)$$

The bandwidth of the complex envelope in (4.15) is larger than that of each individual channel, and is equal to sum of the bandwidths of each channel and the frequency separation of the two carriers. That is, the modulation bandwidth that must be used in simulation must incorporate both channels including the span between channels. Therefore the sample time step of SET will be smaller for the same accuracy. In contrast MET utilizes a different complex envelope for each channel so computation does not depend on the frequency separation of the channels.

## 4.7 Summary

A single-channel envelope transient analysis was extended to a multichannel envelope transient analysis for multichannel applications. Single-channel envelope transient could handle a multichannel signal; however, multichannel envelope transient was more suitable for simulating multichannel circuits since the channels were separately treated. This resulted in less computational demand. Equations for a circuit simulator were formulated for constructing a general circuit simulator that could handle multichannel digitally-modulated signals and capture general baseband memory effects. Such a simulator will be substantiated using MATLAB in Chapter 5.

Multichannel envelope transient used the constituent equations of the linear resistor, inductor and capacitor in the envelope domain when building circuit equations. The constituent equations looked different from the constituent equations of such elements in the time domain but basically related the same legitimate voltage-current laws as those in the time domain. By using the constituent relations the multichannel envelope transient analysis developed in this chapter could capture arbitrary baseband memory effects. This eliminated the ambiguity of computing baseband products that was previously reported in [5]–[10].

Importance of capturing baseband effects was shown by comparing envelope transient and a sequence of harmonic balance analyses with time-varying phasors. The difference came from that equations of envelope transient included derivatives with respect to time but those of harmonic balance did not. Thus harmonic balance could not capture any memory effects. Also demonstrated was computational efficiency of the multichannel envelope transient analysis compared with the single-channel envelope transient analysis. The multichannel envelope transient provided even better computational efficiency when channels were separated widely.

Investigating envelope transient thoroughly (especially the mechanism of capturing baseband memory effects) and extending the conventional envelope transient to multichannel envelope transient will open up the way to use a multi-slice model in the multichannel envelope transient and eventually to simulate multichannel RF systems exhibiting baseband memory effects. An example of using a multi-slice model in multichannel envelope transient will be demonstrated in Chapter 5.

## Chapter 5

# Multichannel Communication

## Systems

### 5.1 Introduction

The multi-slice behavioral model introduced in Chapter 3 was developed for single-channel applications. It tends to be inaccurate when it is used in multichannel applications. For multichannel applications, the multi-slice model needs to be modified. Also, the performance of the multi-slice model was dependent on input excitations because the extracted linear filter in the second slice was not smooth. In Section 5.2 the model is modified for multichannel applications. The first slice of the modified model is extended to include two linear filters and it captures short-term memory effects over a wide frequency band. The second slice of the modified model includes a complex gain block that makes the model in a more realistic form and a linear filter to capture channel dependent baseband effects. Also the baseband filter is extracted in a more smooth shape so the model becomes independent on excitations. In Section 5.3 the multichannel envelope transient analysis developed in Chapter 4 is implemented

in MATLAB and it is used to simulate a simple amplifier model excited with a two-channel WCDMA signal for validation. In Section 5.4 the baseband portion of the multi-slice model developed in Section 5.2 is transformed to a circuit and is used in multichannel envelope transient simulations to demonstrate usage of multi-slice models in established circuit simulators. Finally the extracted model is used in transient simulation in Section 5.5. The important result is that the behavioral model can be used in efficient transient simulation as, here, the carrier frequency of a single-channel WCDMA signal can be scaled.

## 5.2 Modeling of a Power Amplifier Using a Multi-Slice Behavioral Model

The multi-slice behavioral model in Chapter 3 is modified to make the model cover a wide frequency band for multichannel applications. A multi-slice behavioral model to be introduced in this section similarly consists of two slices as shown in Figure 5.1. The first slice includes two linear frequency domain filters,  $H_1(f)$  and  $H_2(f)$ , and

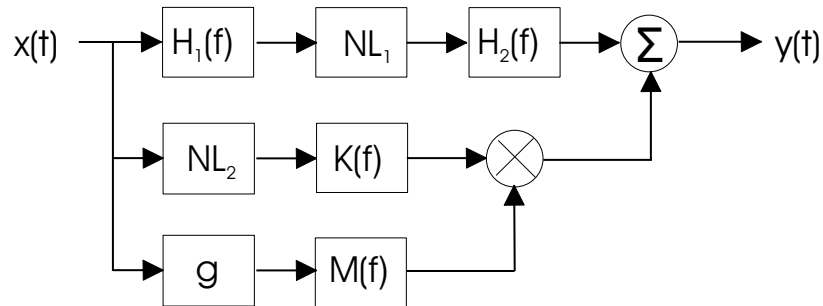


Figure 5.1: A two-slice nonlinear system behavioral model for multichannel applications.

a static nonlinear function box,  $NL_1$ , between the two filters. The static nonlinear function is represented by an odd-order polynomial having complex coefficients and accounts for memoryless nonlinearities of an RF system at the center of the operating

frequency band. The linear filters work as pre- and post-distorters and capture short-term memory effects. The structure of the first slice is the same as the structure of the Wiener-Hammerstein model in Subsection 2.3.3 but extraction of the slice and measurement for the extraction are different as shown later in this section. The second slice consists of two sub-slices. The first sub-slice includes a static nonlinear function box,  $NL_2$ , followed by a linear frequency domain filter,  $K(f)$ . The static nonlinear function is represented by an even-order polynomial having real coefficients and produces baseband frequency components. The linear filter shapes the baseband components in order to capture proper baseband contributions. The second sub-slice includes a linear frequency domain filter,  $M(f)$ , and accounts for baseband effects dependent on carrier frequencies in the case of multichannel RF systems. A complex gain block,  $g$ , is also used to normalize the filter. An ideal mixer is employed at the end of the second slice to up-convert the baseband components from the first sub-slice by mixing with the output of the second sub-slice.

Extraction of the first slice begins by finding the coefficients of the odd-order polynomial from AM-AM and AM-PM responses at the reference frequency (normally the center frequency of the operating frequency band). After the coefficients are determined, the two linear filters are computed at the same time by fitting to two-dimensional single-tone measurements. The method used to obtain the measurements is discussed in Subsection 2.3.3. In the fitting process, a matrix of the input signal for the extraction of the filters can be constructed as

$$\hat{\mathbf{x}} = [\hat{x}_1 \quad \hat{x}_2 \quad \cdots \quad \hat{x}_m]^T \quad (5.1)$$

where  $\hat{x}$  and  $m$  respectively represent an input phasor and the number of input levels swept at a single frequency. T represents transposition of the matrix. Considering that the static nonlinear function is in the form of (2.6), an output matrix of the first slice at a single frequency other than the reference frequency, say  $f_1$ , can be computed as

$$\begin{aligned} \tilde{\mathbf{y}} &= [\tilde{y}_1 \quad \tilde{y}_2 \quad \cdots \quad \tilde{y}_m]^T \\ &= \sum_{k=0}^{(n-1)/2} \frac{a_{2k+1}}{2^{2k}} \binom{2k+1}{k+1} \left| \hat{\mathbf{x}} H_1(f_1) \right|^{2k} \cdot \left( \hat{\mathbf{x}} H_1(f_1) H_2(f_1) \right) \end{aligned} \quad (5.2)$$

where  $\tilde{y}$  represents a modeled output phasor of the 1st slice. The exponent of the matrix and  $\cdot$  are computed using the Hadamard product. An error function now can be made in the matrix form as

$$\begin{aligned} \mathbf{e} &= [e_1 \quad e_2 \quad \cdots \quad e_m]^T \\ &= \hat{\mathbf{y}} - \tilde{\mathbf{y}} \\ &= [\hat{y}_1 \quad \hat{y}_2 \quad \cdots \quad \hat{y}_m]^T - \tilde{\mathbf{y}} \end{aligned} \quad (5.3)$$

where  $\hat{y}$  is a measured output phasor corresponding to the input  $\hat{x}$ . Transfer characteristics of the linear filters at the frequency  $f_1$  are obtained when  $\sum_{k=1}^m |e_k|$  is below the desired tolerance. A diagram of the extraction procedure for the linear filters is shown in Figure 5.2 and this is repeated at different frequencies until the entire operating frequency band is covered. Compared to the extraction method described

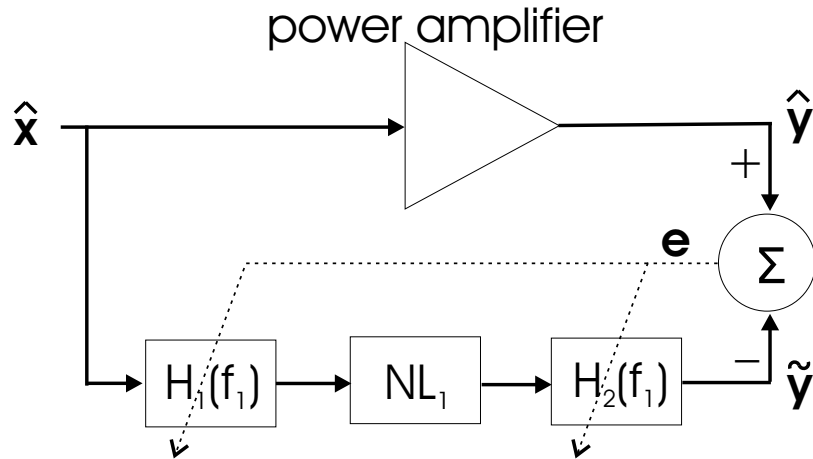


Figure 5.2: A block diagram of the extraction for the linear filters in the first slice.

in Subsection 2.3.3, this method is likely to be more accurate since the parameters are extracted from more measured data.

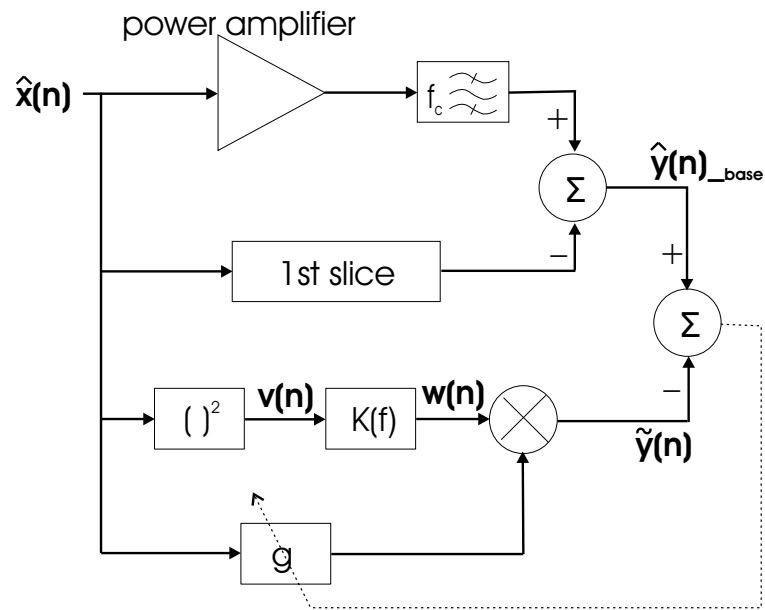
In the second-slice extraction, three kinds of measurements are now used: complex-envelope responses to a single-channel digitally-modulated signal; amplitude responses to two tones swept in frequency separation; and complex-envelope responses to a two-channel digitally-modulated signal. These are respectively used to extract  $g$ ,  $K(f)$

and  $M(f)$  in the second slice. As before the measurements with the single- and two-channel digitally-modulated signals are captured at fundamental frequencies using a vector signal analyzer and are directly used in the extraction. As for the two-tone measurement, amplitudes of third-order intermodulation (IM3) components are measured using a spectrum analyzer. The frequency separation of the two tones are swept to cover the baseband while the asymmetries (or amplitude differences) of the IM3 components being a function of the frequency separation are measured. Even though three kinds of measurements are required, each measurement is simple and easy to conduct. In addition, the extraction itself incorporates self-verification since the extracted parameters are to be based on measurements with various excitations.

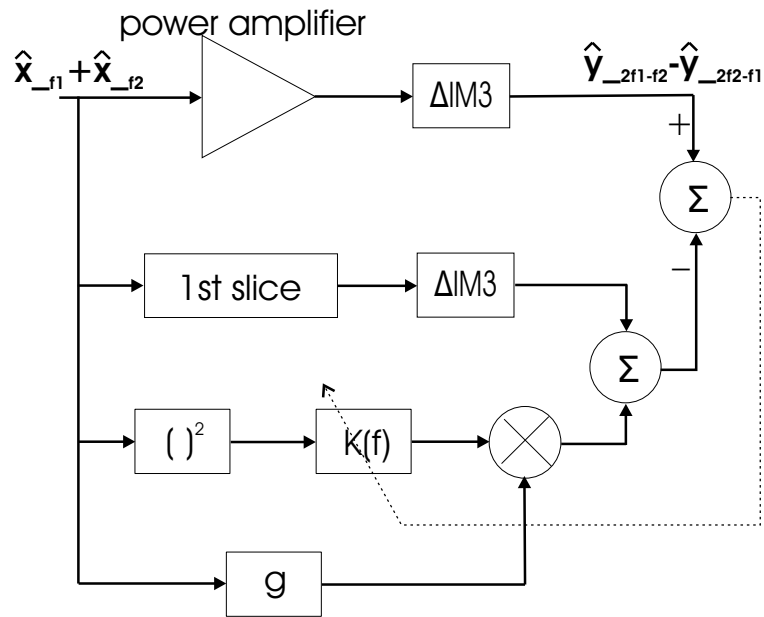
The second slice is extracted sequentially after extraction of the first slice as done in Chapter 3 but now extraction procedure is more complicated. First, the complex gain  $g$  is extracted using a measured response to a single-channel digitally-modulated signal when an input level is low enough that third-order nonlinearity is dominant. The response of the first slice to the same single-channel digitally-modulated input is computed and subtracted from the measurement. The resulting difference is the output of the second slice to be extracted. The complex gain  $g$  in the second sub-slice is extracted by fitting to the result of the subtraction. Since the third-order nonlinearity is dominant,  $NL_2$  is fixed as  $x^2(t)$ . The baseband filter  $K(f)$  is assumed to be an ideal DC rejection filter and the linear filter  $M(f)$  is ignored for the moment. DC components should be rejected by the second slice because the extracted first slice already accounts for them. If DC components were included in the second slice, an extracted model would be inaccurate when an input is a single-tone signal. Thus, the model becomes dependent on excitations, which diminishes generality of the model. In the fitting process as shown in Figure 5.3(a), the output of  $NL_2$  at the baseband is written as

$$v(n)_{base} = \frac{1}{2} \hat{x}(n) \hat{x}^*(n) \quad (5.4)$$

where  $\hat{x}(n)$  and  $n$  are the discrete input complex envelope and the number of the input data respectively.  $\hat{x}^*(n)$  is conjugate of  $\hat{x}(n)$ . The output of the baseband filter



(a)



(b)

Figure 5.3: A block diagram of the extraction for: (a) the complex gain block; and (b) the baseband filter in the second slice.

$K(f)$  is computed using the Fourier and inverse Fourier transforms as

$$w(n) = \mathcal{F}^{-1}\{K(f)V(f)_{base}\} \quad (5.5)$$

where

$$V(f)_{base} = \mathcal{F}\{v(n)_{base}\} . \quad (5.6)$$

$\mathcal{F}\{\}$  and  $\mathcal{F}^{-1}\{\}$  are respectively a Fourier and an inverse Fourier transform operator.

An error function is formed as

$$\begin{aligned} e(n) &= \hat{y}(n)_{base} - \tilde{y}(n) \\ &= \hat{y}(n)_{base} - g \cdot w(n)\hat{x}(n) . \end{aligned} \quad (5.7)$$

The complex gain is determined when  $\sum_{k=1}^n |e(k)|$  becomes below a desired tolerance. Next, the baseband filter is extracted by comparing to the measurements of IM3 asymmetries as shown in Figure 5.3(b).  $\Delta IM3$  boxes in Figure 5.3(b) are conceptually employed so the boxes generate amplitude differences of IM3 products. The baseband filter can be a circuit level model or can be represented in poles and zeros so the filter is smooth enough to make the model independent on input excitations. A pole-zero representation is used in this section and a circuit representation will be used for the enhanced envelope transient simulations in the next section. Poles and zeros of the baseband filter are determined by fitting to the measurements of IM3 asymmetries that are dependent on frequency separation. After that, the gain block is modified. The baseband and gain blocks can iteratively be modified until both modeled responses to the digitally-modulated and two-tone signals are close to the measurements. Usually one or two iterations are enough. Finally the linear filter  $M(f)$  is determined by comparing to measured responses to a two-channel digitally-modulated signal. Compared to the baseband filter, this filter is smooth over the operation band so adjusting phase of the filter depending on the frequency separation of the two channels is usually effective.

The performance of the multi-slice model is validated with the same power amplifier used in Section 3.4. For extraction of the first slice,  $S_{21}$  data of the amplifier was measured at frequencies from 2.2 GHz to 2.6 GHz with a 2 MHz step while the

input amplitude was swept at each frequency. The reference AM-AM and AM-PM responses were modeled from the  $S_{21}$  measurement at 2.4 GHz using an odd-order polynomial function up to 29th order. The measured responses were compared with the modeled responses in Figure 5.2 (a) and (b). They were almost identical. Using the AM-AM and AM-PM responses at other frequencies, the linear filters,  $H_1$  and  $H_2$ , were extracted as shown in Figure 5.5. The modeled AM-AM and AM-PM responses over the operating frequency band were compared with the measured responses as shown in Figure 5.6 and Figure 5.7. The AM-AM responses were very close but the AM-PM responses were very different, especially upper side in the band. This was due to the complex phase responses of the cascaded amplifier and structural limitation of the first slice model as explained in Subsection 2.3.3. However quite a wide band near 2.4 GHz was modeled accurately.

In extraction of the second slice, a single-channel WCDMA signal was used to extract the complex gain  $g$ . At the moment the baseband filter was assumed to be an ideal DC rejection filter. The value of the extracted gain  $g$  was shown in the first row of Table 5.1. After extracting the gain, two-tone  $\Delta$ IM3 measurements with various

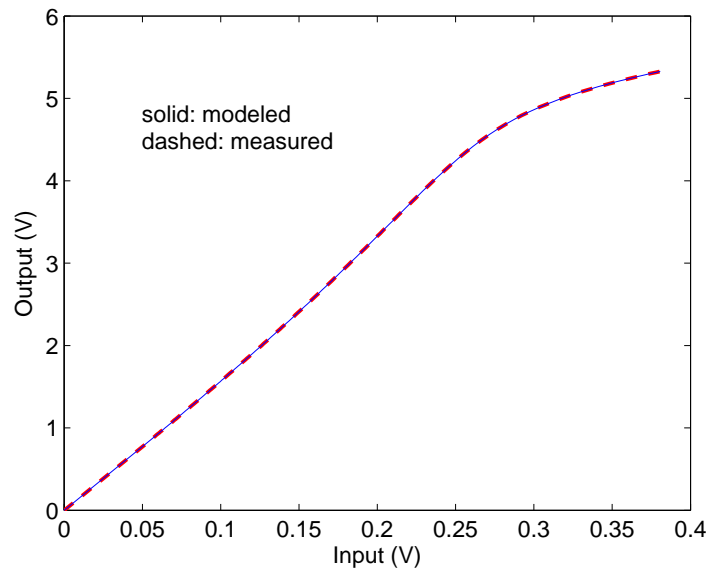
Table 5.1: The extracted values of the complex gain  $g$

Before modification	$13.8590 + 34.8704i$
After modification	$13.8674 + 34.9811i$

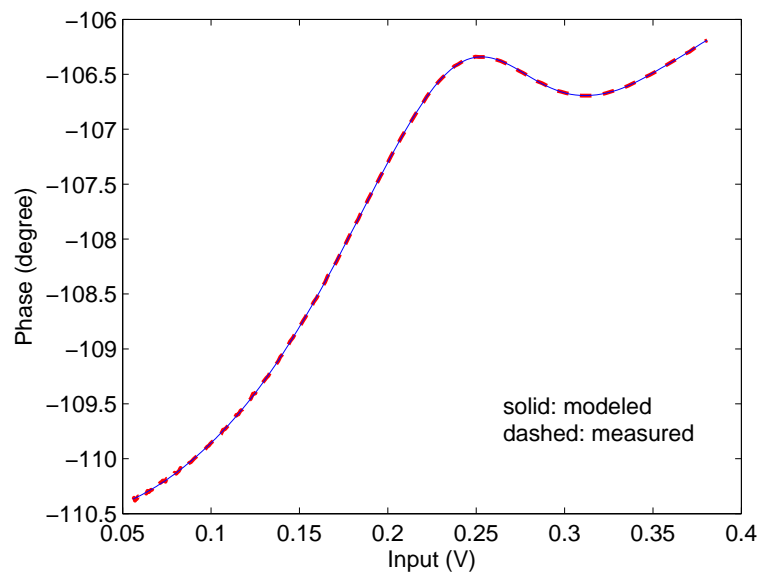
frequency separations were used to extract the baseband filter  $K(f)$ . Considering the measurements, the filter was selected to be in the form of poles and zeros as

$$K(s) = \frac{s(s + z_1)(s + z_2)(s + z_3)}{(s + p_1)(s + p_2)(s + p_3)(s + p_4)} \quad (5.8)$$

The poles and zeros were extracted by comparing with the two-tone  $\Delta$ IM3 measurements. The extracted values of the poles and zeros are shown in Table 5.2. The amplitude and phase responses of the extracted baseband filter were shown in Figure 5.8. The modeled filter was compared with the two-tone  $\Delta$ IM3 measurements in Figure 5.9. Next, the complex gain  $g$  was modified taking the extracted baseband filter into account. The modified value was shown in the second row of Table 5.1. It was

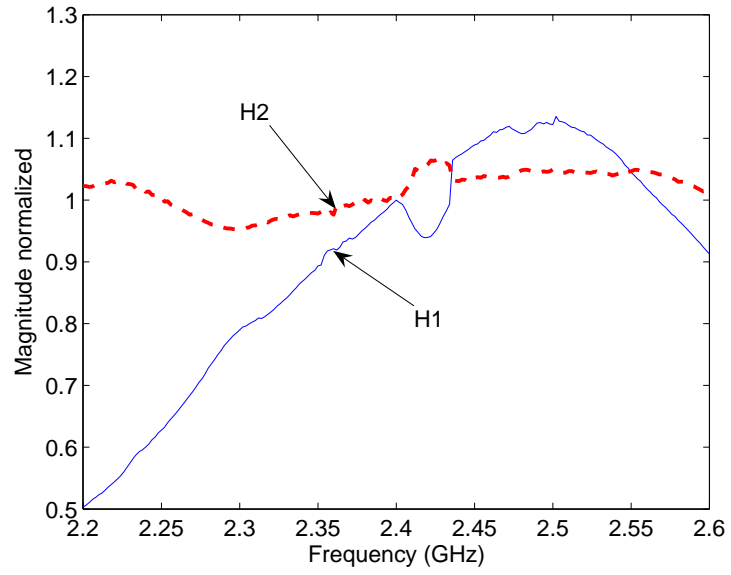


(a)

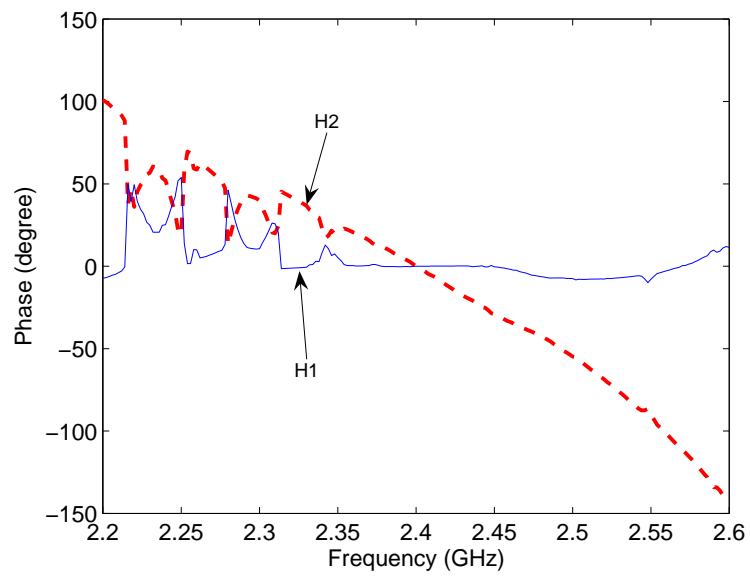


(b)

Figure 5.4: Measured and modeled (a) AM to AM response; and (b) AM to PM response of the amplifier at 2.4 GHz.

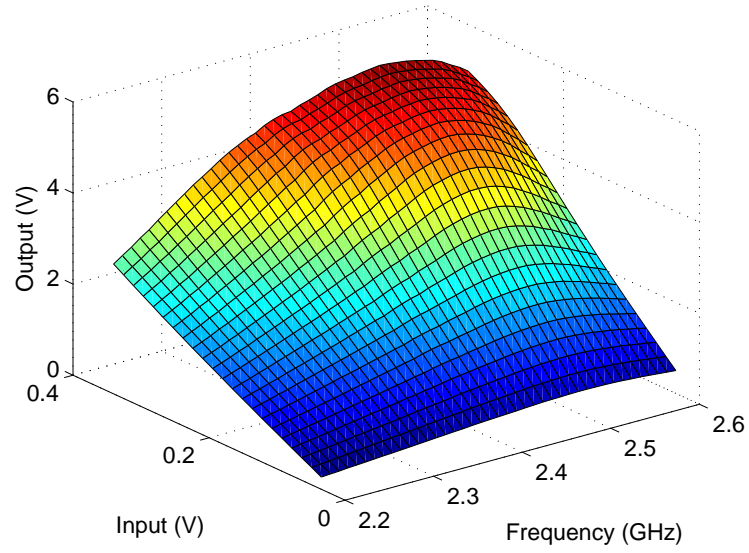


(a)

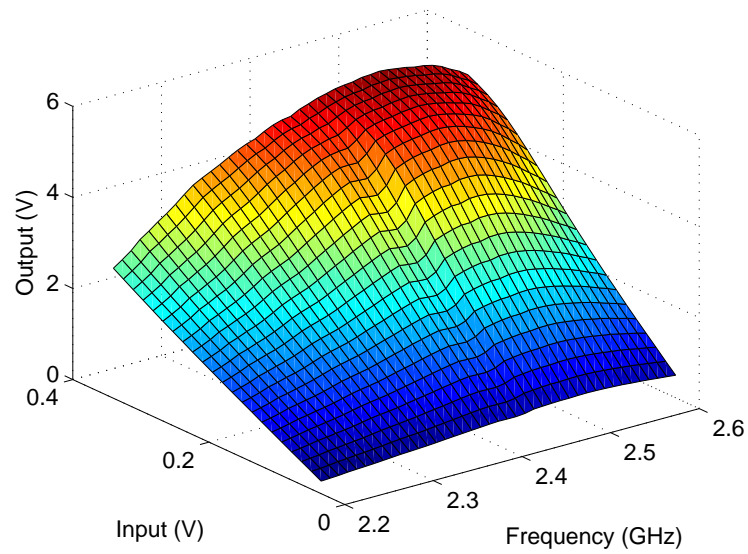


(b)

Figure 5.5: Modeled (a) magnitude response; and (b) phase response of H1 and H2.

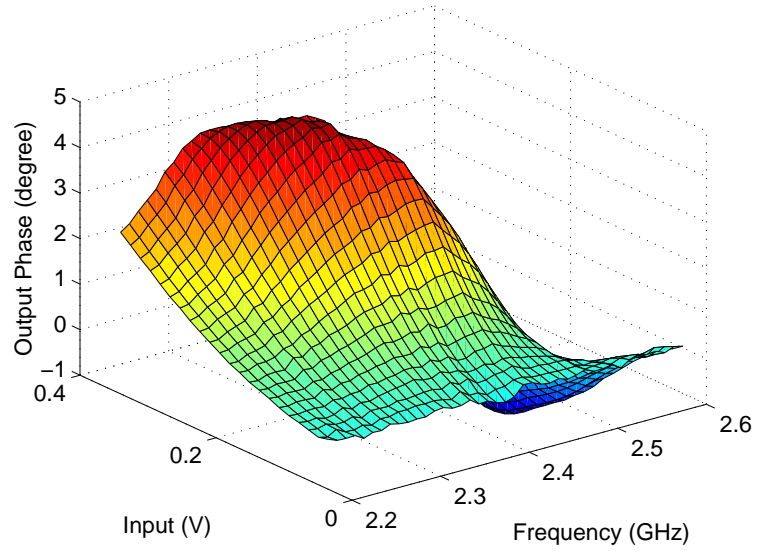


(a)

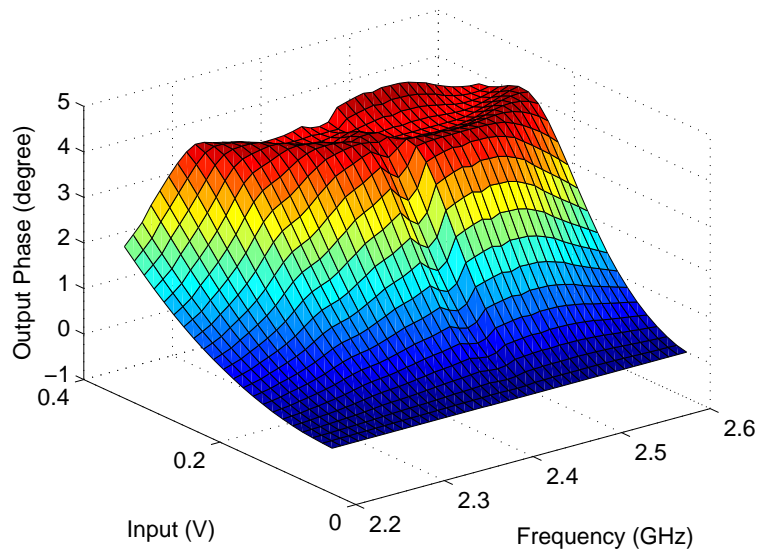


(b)

Figure 5.6: (a) Measured AM-AM responses; and (b) modeled AM-AM responses over the operating frequency band.

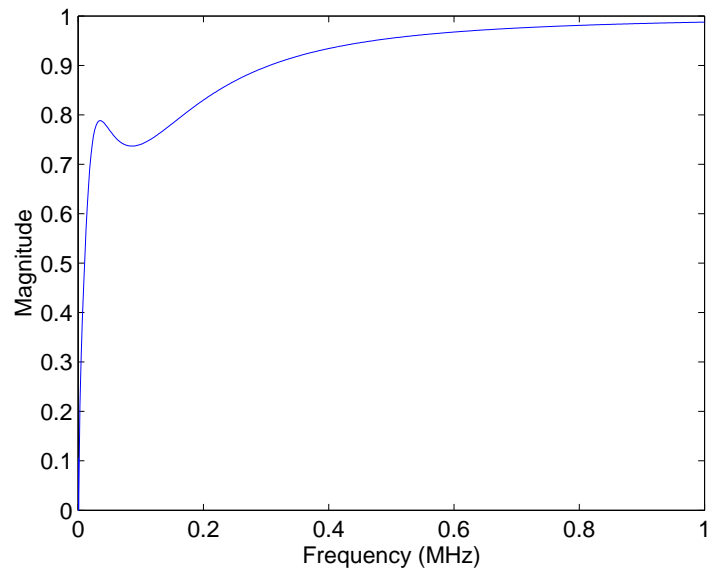


(a)

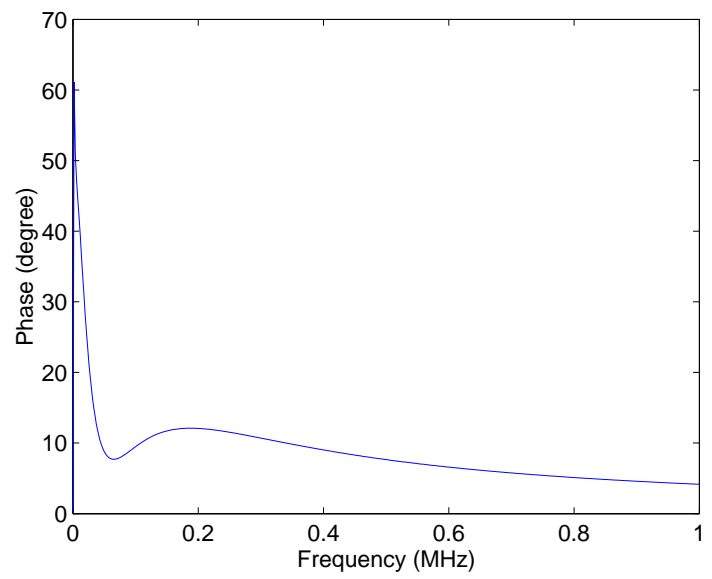


(b)

Figure 5.7: (a) Measured AM-PM responses; and (b) modeled AM-PM responses over the operating frequency band.



(a)

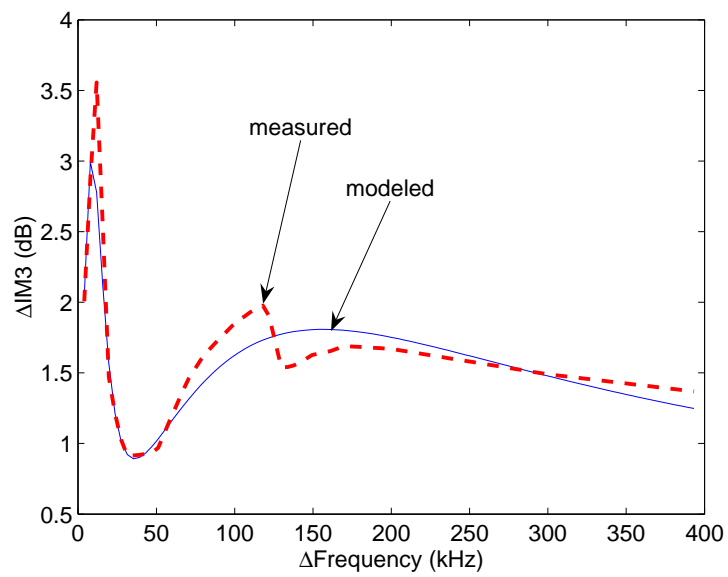


(b)

Figure 5.8: (a) The amplitude response; and (b) The phase response of the baseband  $K(f)$ .

Table 5.2: The extracted poles and zeros of the baseband filter  $K(f)$ 

$z_1$	0.10091084966041e5
$z_2$	1.88392999442162e5
$z_3$	4.86538625518979e5
$p_1$	0.02838425029946e5
$p_2$	0.81323374548877e5
$p_3$	0.81879094047698e5
$p_4$	8.25738338513121e5

Figure 5.9: Measured and modeled magnitude of  $\Delta IM3$  as a function of frequency separation.

observed that the modified value was not very different from the initially extracted value. Finally a two-channel WCDMA signal was used to extract the linear filter  $M(f)$ . The center frequencies of the channels were 2.38 GHz and 2.42GHz. Without the filter  $M(f)$ , the response to the two-channel input was compared with the measurements in Figure 5.10. There were discrepancies on the spectral regrowth of the

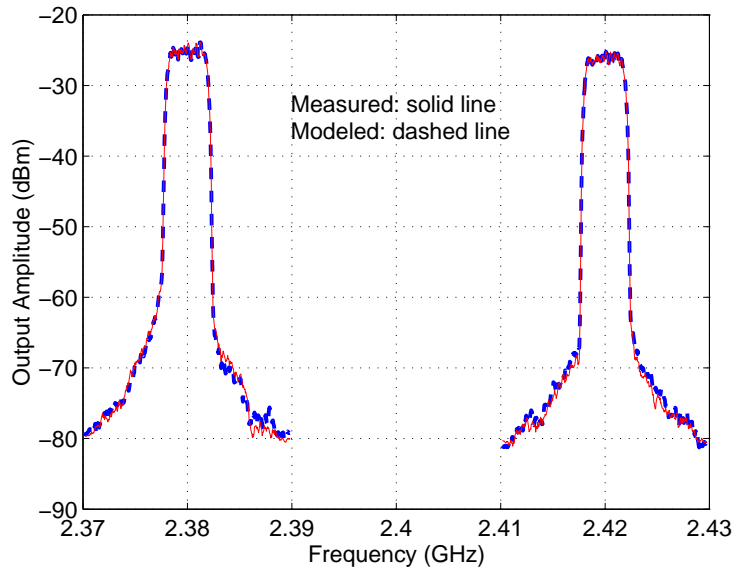


Figure 5.10: Measured output of a two-channel WCDMA signal and modeled output without the filter  $M(f)$ .

channels as shown in Table 5.3 so phases of the filter  $M(f)$  were manually modified to reduce the discrepancies. The extracted phase of the filter  $M(f)$  at the lower and

Table 5.3: Discrepancies (in dB) between the measured and modeled spectral regrowth without the filter  $M(f)$ .

	lower channel	upper channel
lower side	0.41	0.99
upper side	1.14	1.22

upper channels were respectively  $-20^\circ$  and  $20^\circ$ . The filter  $M(f)$  imposed linear phase changes over the operating frequency band as a lossless linear transmission line.

For the validation of the extracted model, a two-tone excitation with the frequency separation of 20 KHz was used first. The amplitudes of the two tones were swept.

Measured and modeled responses to the excitation were shown in Figure 5.11. They

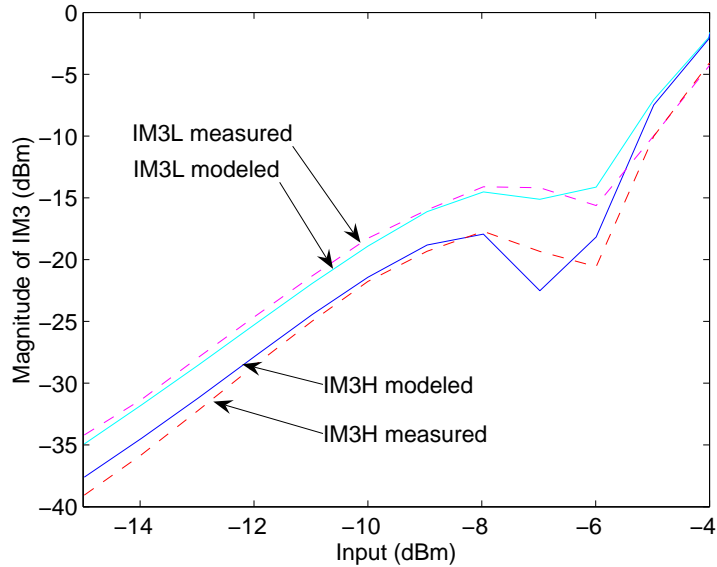
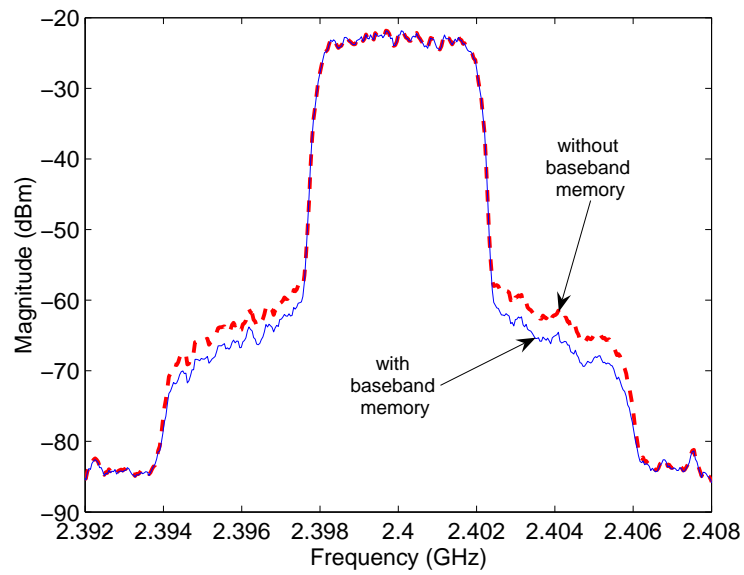


Figure 5.11: Modeled phase response of H1 and H2.

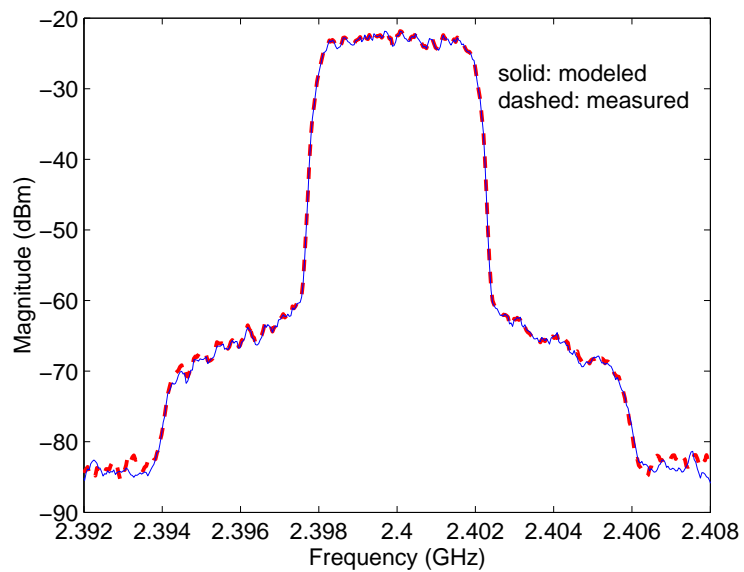
agreed very well. At the high level of the input, there were more discrepancies since the model included only the second order baseband effects. This can be improved by having the model with higher orders. The first slice also needs to model responses at a stronger nonlinear region. Next, a single-channel WCDMA signal was used. In Figure 5.12 (a), the modeled amplitude responses with and without baseband effects were compared. Differences of 2 dB and 3 dB were respectively observed on the lower and upper sides. Asymmetry was about 1 dB. In Figure 5.12 (b), the modeled response with the baseband effects was compared with the measured response. It was observed that the baseband effects were very accurately modeled. Discrepancies were computed and shown in Table 5.4. Figure 5.12 demonstrates that the

Table 5.4: Discrepancies (in dB) between the measured and modeled spectral regrowth.

	memoryless model	memory model
lower side	2.28	0.28
upper side	3.10	0.24



(a)



(b)

Figure 5.12: (a) The modeled amplitude responses with and without baseband effects to a single-channel WCDMA; and (b) the modeled response with baseband effects compared with the measurement.

Wiener-Hammerstein model is unable to model baseband effects. In Figure 5.13 (a), the modeled phase responses with and without baseband effects were compared. The phase responses represented relative output phases to input phases over the channel. Moving average was used to compare the phase responses in the side bands. The relative output phases in the side band were not clear enough to compare since the input phases were originated from noise. In Figure 5.13 (b), the modeled phase response with baseband effects was compared with the measured response. It was clear that the modeled phase response with baseband effects was much closer to the measured response. Averaged phase errors were computed and shown in Table 5.5. Finally a

Table 5.5: Discrepancies between the measured and modeled phase.

	memoryless model	memory model
lower side	18.00°	5.03°
upper side	13.01°	6.82°

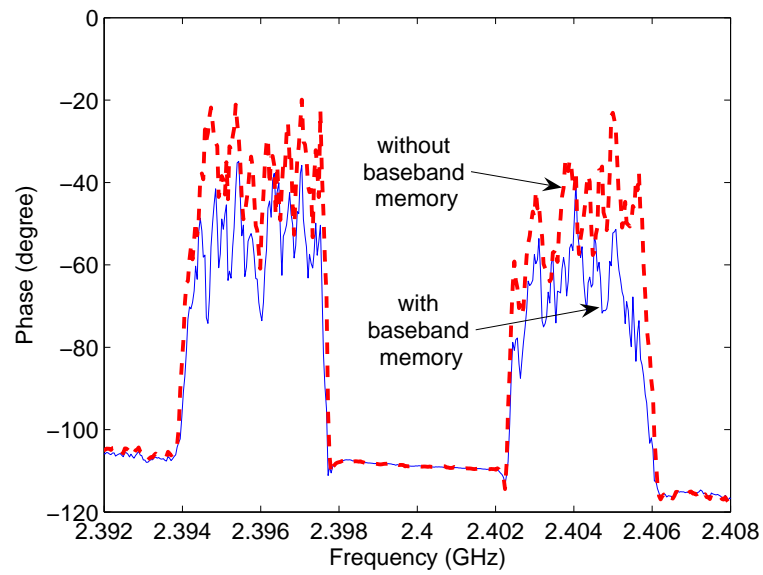
two-channel WCDMA signal was used to validate the model. In Figure 5.14(a), the modeled results with and without baseband effects were compared. There were about 3 dB discrepancies in the upper channel. In Figure 5.14(b), the modeled results with baseband effects were compared with the measurements. They matched very well with the measurements at both channels. Considering that the level of the spectral regrowth was  $-45$  dBc, baseband effects were modeled quite accurately. Computed errors were shown in Table 5.6 and 5.7.

Table 5.6: Discrepancies (in dB) between the measured and modeled (without baseband effects) spectral regrowth.

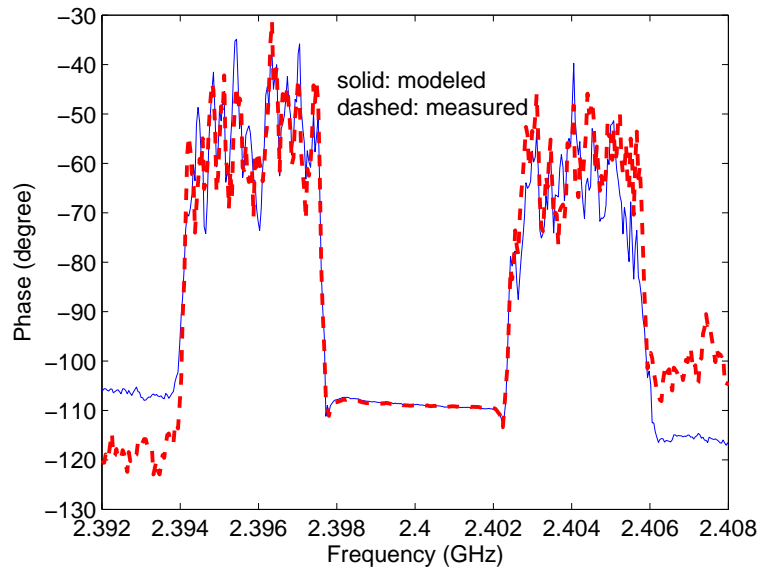
	lower channel	upper channel
lower side	0.38	2.71
upper side	0.35	2.91

Table 5.7: Discrepancies (in dB) between the measured and modeled (with baseband effects) spectral regrowth.

	lower channel	upper channel
lower side	0.26	0.69
upper side	0.34	1.01

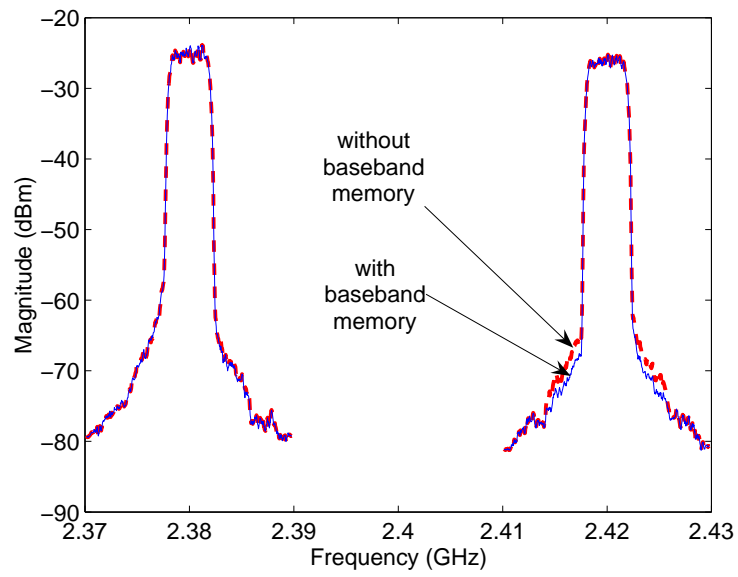


(a)

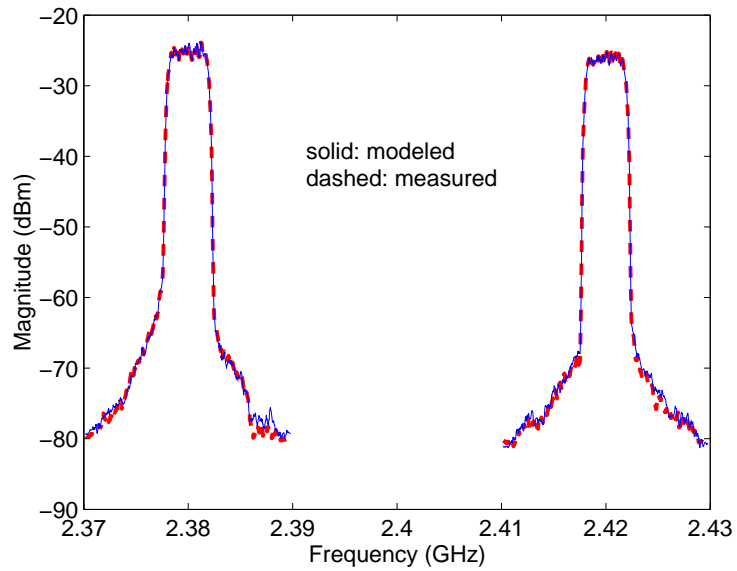


(b)

Figure 5.13: (a) The modeled phase responses with and without baseband effects to a single-channel WCDMA; and (b) the modeled response with baseband effects compared with the measurement.



(a)



(b)

Figure 5.14: (a) The modeled amplitude responses with and without baseband effects to a two-channel WCDMA; and (b) the modeled response with baseband effects compared with the measurement.

## 5.3 Enhanced Envelope Transient Simulation in MATLAB

The multichannel envelope transient analysis developed in Chapter 4 was implemented in MATLAB. See Appendix A for the MATLAB codes. In this section the analysis implemented is applied to a simple circuit model as an example. The example circuit model is shown in Figure 5.15. The model is divided into linear and nonlinear

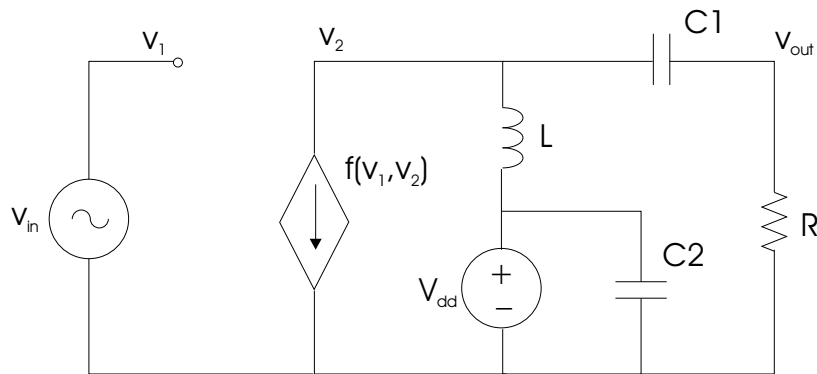


Figure 5.15: The circuit model of the amplifier.

portions for simulations as shown in Figure 5.16. The nonlinear current and voltage

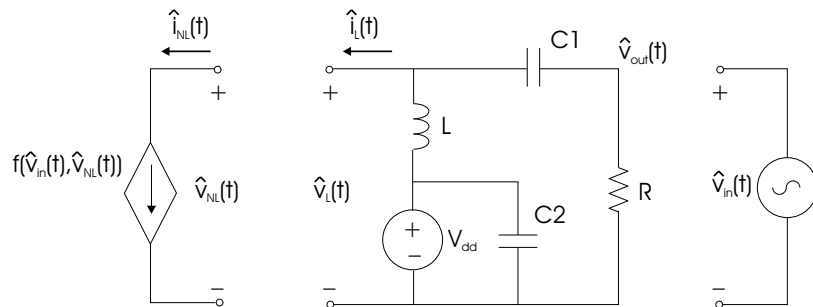


Figure 5.16: The circuit divided into the linear and nonlinear sub-circuits.

are computed in the time domain, and then they are converted to the phasors  $\hat{i}_{NL}(t)$  and  $\hat{v}_{NL}(t)$  by using the Fourier transform. This computation is straight forward.

The linear portion is computed in the frequency domain. Circuit equations by using the KCL and KVL in complex envelope can be written as

$$\hat{i}_L(t) + \hat{i}_{C1}(t) + \hat{i}_{ind}(t) = 0 , \quad (5.9)$$

$$\hat{i}_{C1}(t) = j\omega C1(\hat{v}_L(t) - V_{dd}) + C1 \frac{(\hat{v}_L(t) - V_{dd})}{dt} , \quad (5.10)$$

$$\hat{v}_L(t) - V_{dd} = j\omega L \hat{i}_{ind}(t) + L \frac{d\hat{i}_{ind}(t)}{dt} \quad (5.11)$$

and

$$\hat{i}_{C1}(t) = \frac{\hat{v}_{out}(t)}{R} . \quad (5.12)$$

Using (5.9)–(5.12) and discretizing, the equation between the linear current  $\hat{i}_L(t)$  and voltage  $\hat{v}_L(t)$  is constructed as

$$\begin{aligned} \hat{v}_L(t_n) = & \left( (1 + j\omega RC1 + \frac{RC1}{h})(j\omega L + \frac{L}{h})\hat{i}_L(t_n) + \frac{C1}{h}(j\omega L + \frac{L}{h})(\hat{v}_L(t_{n-1}) - \hat{v}_{out}(t_{n-1})) \right. \\ & \left. + (1 + j\omega RC1 + \frac{RC1}{h})(V_{dd} - \frac{L}{h}\hat{i}_L(t_{n-1})) \right) \\ & / \left( (j\omega L + \frac{L}{h})(j\omega C1 + \frac{C1}{h}) + (1 + j\omega RC1 + \frac{RC1}{h}) \right) \end{aligned} \quad (5.13)$$

where  $h$  is a time step. When a circuit is more complex, circuit equations can be built in a matrix form as described in Chapter 4.

A flow chart of the simulation procedure is shown in Figure 5.17. At each sample time, a linear current is guessed and then a linear voltage is computed from the linear current. Next a nonlinear current is computed from a nonlinear voltage that is the same as the linear voltage. After that, the nonlinear current is compared with the linear current guessed. If the difference between the two current is greater than a desired tolerance, the linear current is modified by using the Newton-Raphson method. These steps are repeated until the current difference is less than the tolerance. Using the circuit in Figure 5.16, a multichannel ET simulation was conducted. Simulation results are shown in Figure 5.18. The input was a two-channel WCDMA signal. The center frequencies of the channels were located at 2.39 GHz and 2.41 GHz. Since the model used was a simplified version and did not include any feedback loop between the input and output, no asymmetric spectral regrowth was observed.

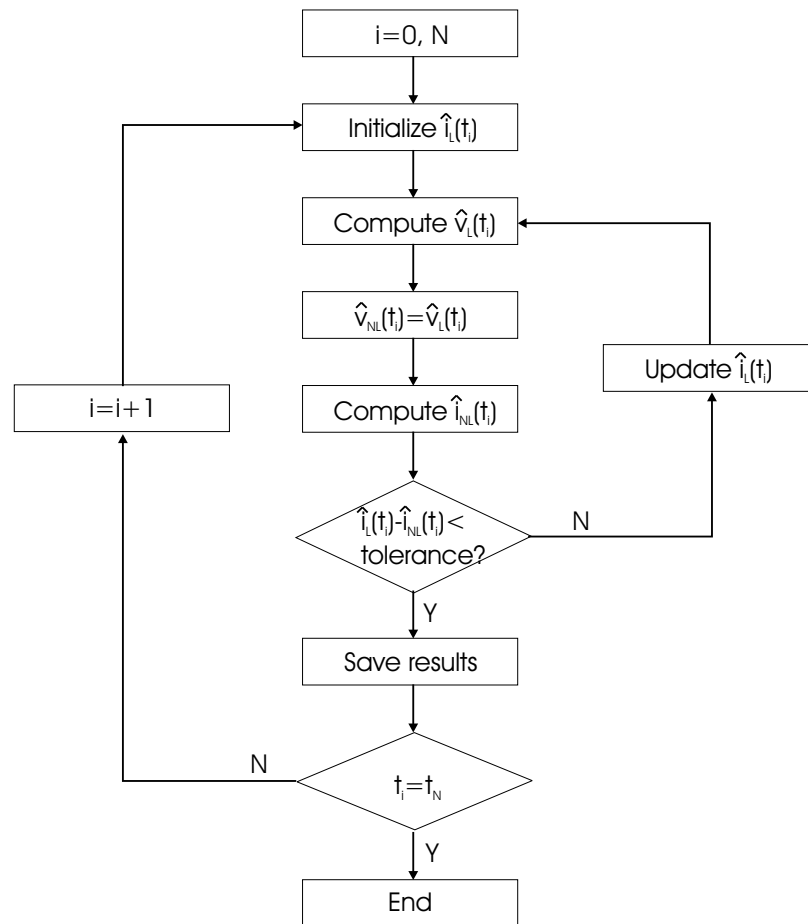


Figure 5.17: The flow chart of the multichannel envelope transient simulations.

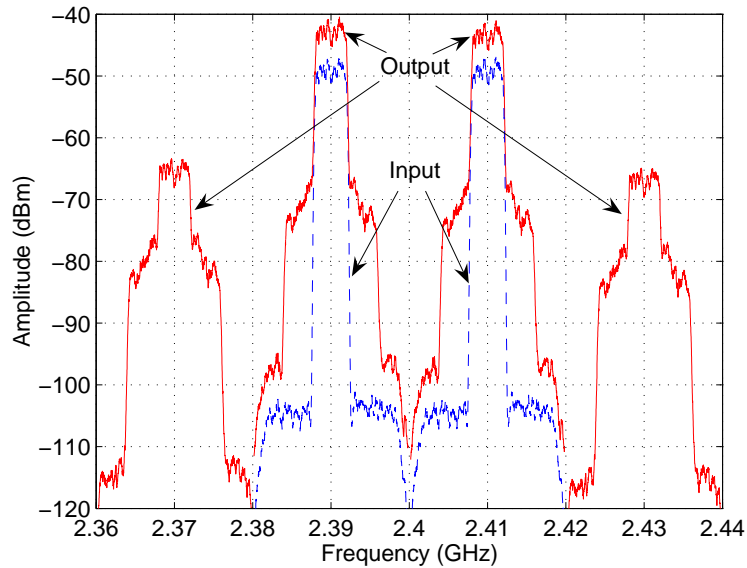


Figure 5.18: The results of the multichannel envelope transient simulations.

## 5.4 Multichannel Envelope Transient Simulation

### Using a Multi-Slice Model

The multi-slice model developed in Chapter 3 can be used in envelope transient simulations. As an example the baseband part of the multi-slice model developed in Section 5.2 is modified to apply the multichannel envelope transient analysis coded in MATLAB. The modified baseband circuit is shown in Figure 5.19. The parameters of the baseband circuit are obtained by fitting manually to measured IM3 asymmetries. This can be done by least square fitting. While sweeping frequency separation of two tones, IM3 asymmetries of the modified model are compared with measurements in Figure 5.20 to check the modified baseband filter. The modeled results are close to the measurements up to 50 kHz of frequency separation but there are more discrepancies at higher frequency separations. This is due to a simple baseband circuit model. However simulation results with an input of a two-channel WCDMA signal agree with measurements as shown in Figure 5.21. In Figure 5.21(a) a sequence of HB

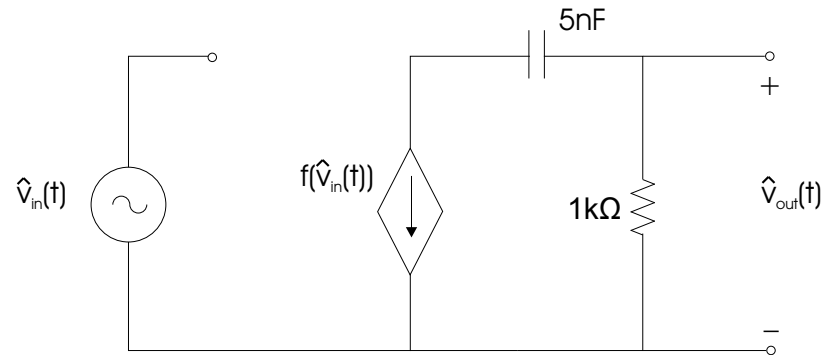


Figure 5.19: The baseband circuit for the multichannel envelope transient simulations.

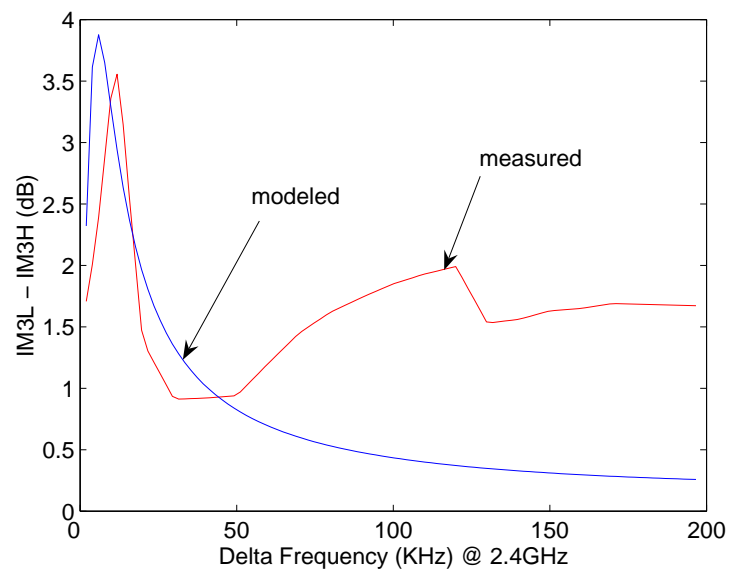
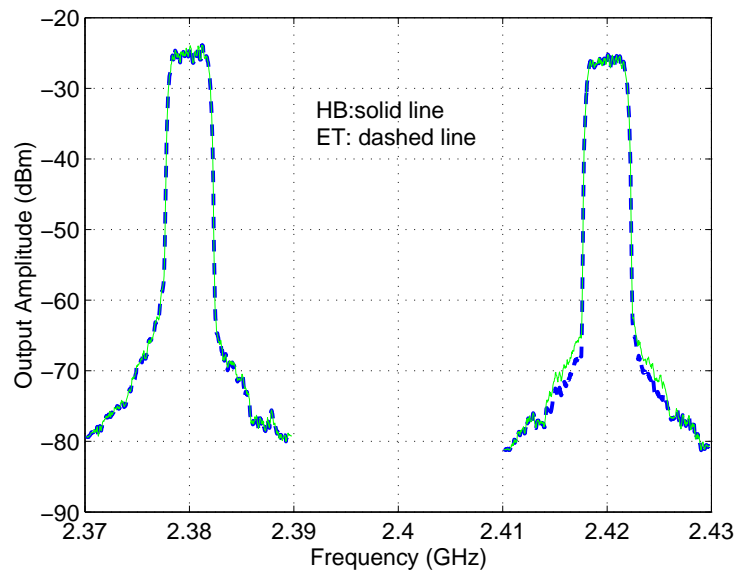
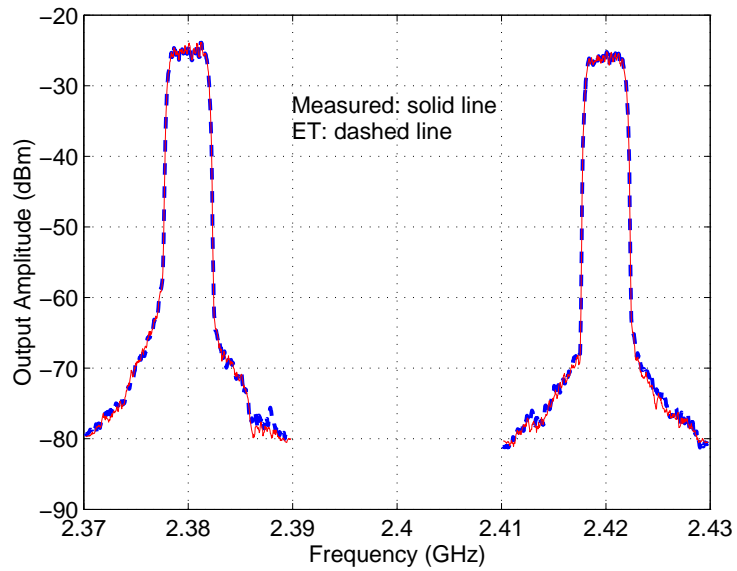


Figure 5.20: Measured and modeled IM3 asymmetries.



(a)



(b)

Figure 5.21: (a) The modeled amplitude responses with and without baseband effects to a two-channel WCDMA; and (b) the modeled response with baseband effects compared with the measurement.

simulations is compared with a multichannel ET simulation. There is not much discrepancy in the lower channel but about 3 dB discrepancy in the upper channel. This shows that baseband effects in case of multichannel look different from the single-channel case in which asymmetric spectral regrowth is observed. In Figure 5.21(b) the multichannel ET simulation is compared with measurements. It agrees well with the measurements at the both channels. Computed errors are shown in Table 5.8 and 5.9.

Table 5.8: Discrepancies (in dB) between the measured and modeled (without baseband effects) spectral regrowth.

	lower channel	upper channel
lower side	0.38	2.71
upper side	0.35	2.91

Table 5.9: Discrepancies (in dB) between the measured and modeled (with baseband effects) spectral regrowth.

	lower channel	upper channel
lower side	0.26	0.68
upper side	0.33	1.01

## 5.5 Time-Marching Simulation Using a Multi-Slice Model

Generally transient simulation of RF circuits or systems excited with digitally-modulated signals is not practically feasible due to tremendous computational demands. This problem is circumvented by reducing orders of the carrier frequency of a modulated signal. In this section the extracted multi-slice model in Section 5.2 is used in transient simulation. The excitation of the model is the same single-channel WCDMA as in Section 5.2 and the carrier frequency of the signal is originally 2.4 GHz. A new carrier frequency is set to be 20 MHz for better computational efficiency. With the new carrier frequency computations can be reduced by a factor

of 120 (2.4GHz/20 MHz) if the same number of sampled points per period is simulated for the same amount of time, which provides the same accuracy. A similar frequency scaling technique is shown in [49] but time-domain computation is done only for polynomials with real coefficients. As the first step, the drive signal is regenerated with a carrier of 20 MHz from a measured input complex envelope of the WCDMA signal as shown in Figure 5.22. The inphase,  $I(t)$ , and quadrature,  $Q(t)$ ,

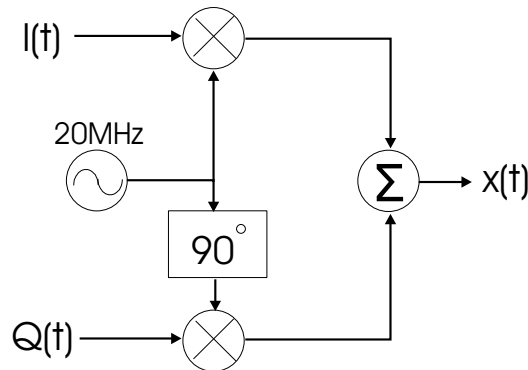


Figure 5.22: Generation of a WCDMA input signal with 20 MHz of the carrier frequency.

baseband signals can be obtained from the complex envelope. The baseband signals vary relatively slowly on the scale of the sampling time step of the modulated signal, that is, the sampling time step of the baseband signals, 50 ns, is twenty times that of the modulated signal, 2.5 ns, if it is sampled twenty points per period. Consequently the complex-envelope signal needs to be interpolated. If we look at the frequency spectrum of the interpolated signal, there are harmonic and spurious frequency products as shown in Figure 5.23. Amplitudes of these frequency products are as large as  $-40$  dBc. This would be big enough to degrade accuracy of modeling distortion if the undesired frequency products were included in the time-domain input signal to the model. Thus, these frequency products should be suppressed in the frequency domain and then the processed frequency spectrum is transformed into a time-domain signal.

In transient simulation, the static nonlinear function block, which is a polynomial with complex coefficients, in the first slice of the model is decomposed for time-domain computation as shown in Figure 5.24. The linear filters  $H_1(f)$  and  $H_2(f)$  in the first

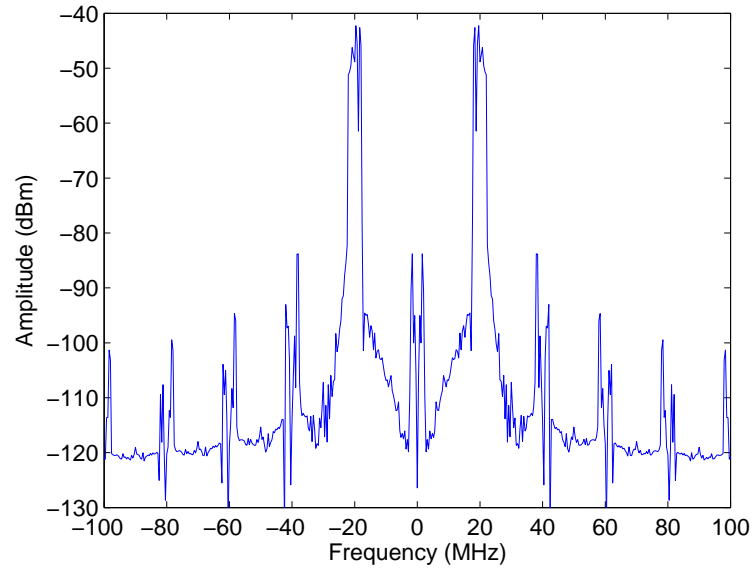


Figure 5.23: A frequency spectrum of the linearly interpolated input signal.

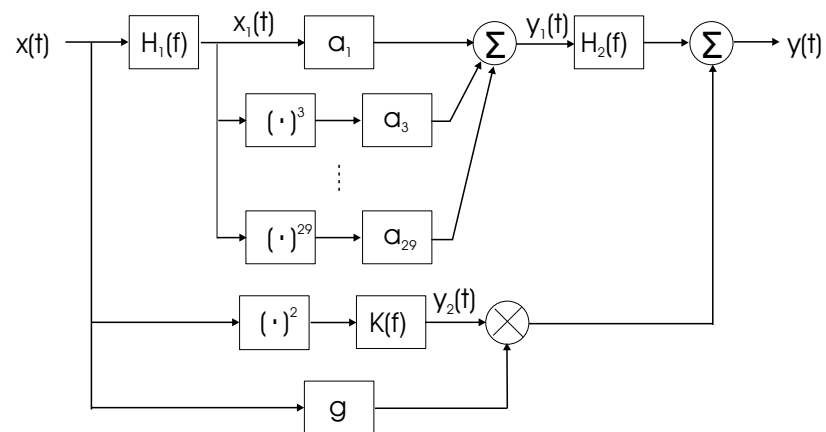


Figure 5.24: Multi-slice behavioral model in transient simulation.

slice do not affect the output much because the transfer characteristics of the both filters are close to unity over the channel bandwidth. Accordingly the filters are virtually ignored in this section; however, for multichannel applications these filters should be synthesized into circuit models or other models that can be computed in the time domain. The linear filter  $K(f)$  in the second slice is represented with a simple DC rejection filter as shown in Figure 5.19.

Computation of a polynomial with complex coefficients in the time is done as

$$y_1(t) = \sum_n \left[ \text{Re}\{a_n\}x_1^n(t) + \text{Im}\{a_n\}x_1^n(t + \Delta t) \right] \quad (5.14)$$

where  $\text{Re}\{\}$  and  $\text{Im}\{\}$  are operators that respectively generate real and imaginary numbers of the operands.  $\Delta t$  is a time-delay determined by  $1/(4f_0)$  where  $f_0$  is the carrier frequency. The complex gain box  $g$  is computed similarly. When multiplication of a complex coefficient is modeled in SPICE-like simulation, a voltage-controlled-voltage source can be used as shown in Figure 5.25. The baseband part of the second

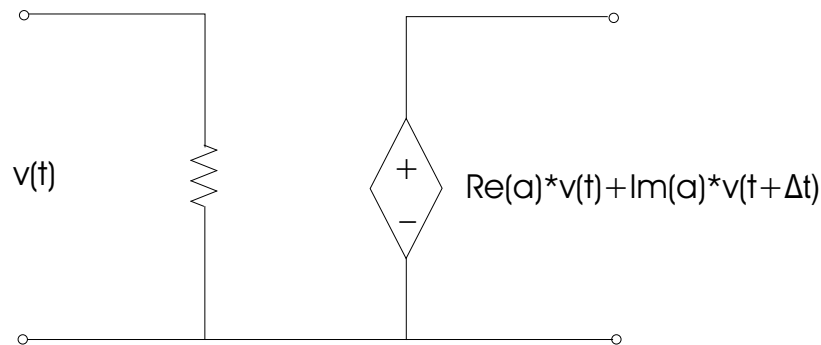


Figure 5.25: A SPICE model for computation of a complex coefficient  $a$ .

slice is computed as

$$y_2(t_n) = \frac{RC}{h + RC} \left( x^2(t_n) - x^2(t_{n-1}) + y_2(t_{n-1}) \right) \quad (5.15)$$

where  $t_n$  and  $h$  respectively represent  $n$  th sampling time and a sampling time-step. Values of the circuit elements  $R$  and  $C$  are the same as shown in Figure 5.19.

An output response of the multi-slice model to a WCDMA signal is Fourier-transformed and the resulting frequency spectrum around carrier frequency is shown

in Figure 5.26. The output frequency spectrum is compared to the response of the

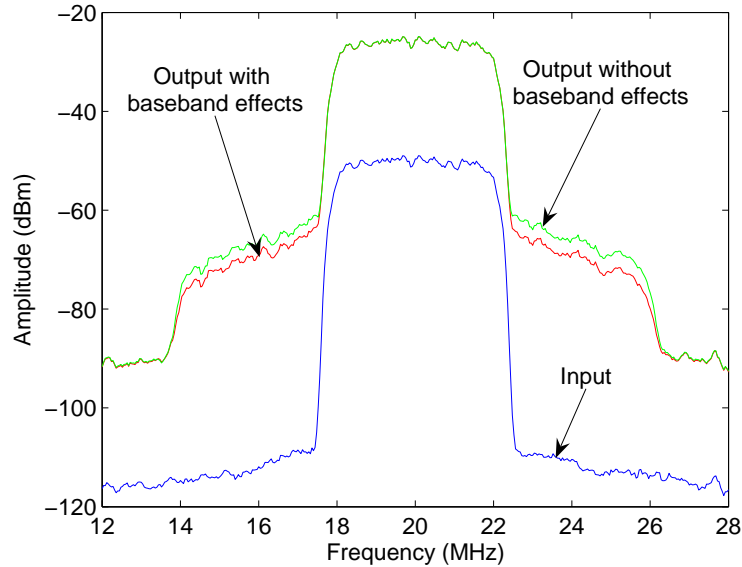


Figure 5.26: Input and output frequency spectra of the multi-slice model.

first slice only that is the output without baseband effects. There is about 1 dB of asymmetry if we consider that the spectral regrowth of the output without baseband effects is symmetrical. The spectra shown in Figure 5.26 are the positive frequency spectra only so the power level is 3 dB less than the actual power. The modeled output frequency spectrum is compared with a measurement in Figure 5.27. This is done by compensating the carrier frequency and the power of 3 dB. Since the measured frequency spectrum is generated from a complex envelope, the power of the spectrum is at an actual level. By comparing to the output spectrum of the first slice, it is shown that baseband effects are well modeled. Computed errors are shown in Table 5.10. A part of the modeled output in the time domain is compared with

Table 5.10: Discrepancies (in dB) between the measured and modeled spectral regrowth.

	memoryless model	memory model
lower side	1.71	0.81
upper side	2.59	0.66

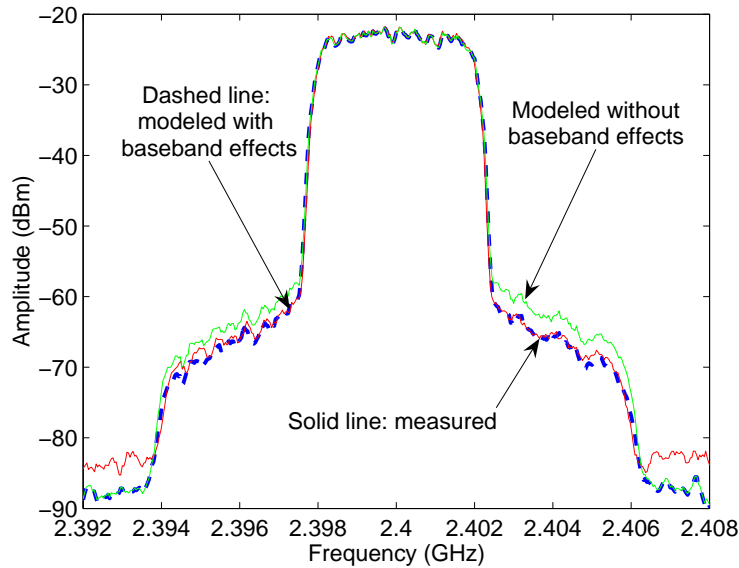


Figure 5.27: Measured and modeled output frequency spectrum.

a measurement in Figure 5.28. There are discrepancies at the beginning. This is because the first sampled point of the measured input and output complex envelopes is artificially inserted to be zero when time starts and then the modified complex envelopes are used to generate corresponding time-domain signals. The generated time-domain input signal is used in simulation to get the modeled output that is compared to the time-domain output generated from the modified complex envelope. Thus the effect of inserting a zero is carried on because of the time shift of  $\Delta t$  when computing complex coefficients. Other than that the measured and modeled results agree very well. A computed error is 0.92%.

In this section, the versatility of a multi-slice model was demonstrated. Not only does a multi-slice model capture baseband effects accurately but it is also compatible with a transient simulator such as SPICE. This implies that there is no restriction to the drive signal. For example, a digitally-modulated signal with noise can be used for BER tests of a communication system. Therefore this opens up a new concept in simulation of communication systems.

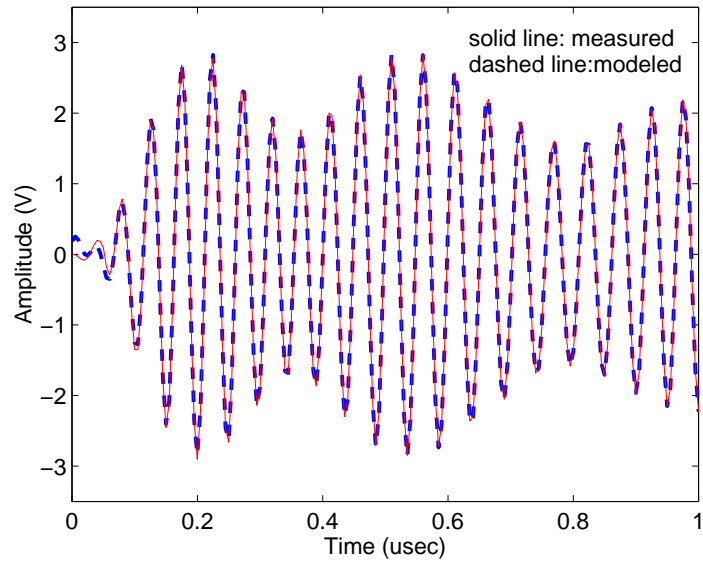


Figure 5.28: A part of the modeled and measured time-domain signal.

## 5.6 Summary

The multi-slice model used in Chapter 3 was modified for multichannel applications and the modified model was built with new extraction procedures. The extraction was done using relatively simple measurement compared to two-dimensional two-tone IM3 measurement. The extracted model accurately captured baseband effects of a power amplifier excited with a two-channel WCDMA signal. The extracted baseband filter was smooth unlike the previously extracted filter shown in Chapter 3. Thus the model worked with various excitations; single tone, two-tone and single-channel WCDMA. This was the first time that a behavioral model was reported to systemically capture baseband effects of a multichannel RF system and the model was extracted using simple measurement.

A multichannel envelope transient analysis was implemented in MATLAB and a simple circuit model of an amplifier was used to validate the implementation. Simulation results with a two-channel WCDMA excitation was included. This implementation helped with investigating baseband effects of a RF circuit by turning on and

off the derivatives of the envelope transient equations. Also the implementation built the basis for using a multi-slice model in multichannel envelope transient.

A multi-slice model was able to be used in already established circuit simulators such as multichannel envelope transient and transient analysis as well as it captured baseband effects accurately. The baseband portion of the multi-slice model extracted in Section 5.2 was modified into a circuit and the multichannel envelope transient analysis implemented in Section 5.3 was applied to the circuit. This simulation was validated by comparing the simulation results with measurements. Finally the extracted multi-slice model was used in transient simulation. This was done with a low carrier frequency by reducing the order of the RF frequency. Simulation results agreed with measurements very well. This approach made it possible not only to simulate an RF system in the time domain but to use any drive signal such as CDMA, chirp, noise signal in RF system simulation. This opened up a new concept in RF system simulation.

# Chapter 6

## Conclusion and Future Work

### 6.1 Conclusion and Discussion

As the input signal bandwidth increases in modern RF communication systems, capturing memory effects becomes an issue in the modeling community. Modeling of RF communication systems has usually been done using measured data but memory effects of an RF system cannot be measured directly. Thus it needs a strategic approach to measure and model the effects. Considering presently available measurement techniques, memory effects were divided into nonlinear RF effects and nonlinear baseband effects. These were respectively similar to electrical short-term and long-term memory effects. This classification paved the way to modeling baseband effects of a multichannel RF system with a multi-slice behavioral model.

As a preliminary step toward modeling baseband effects of a multichannel power amplifier, a multi-slice behavioral model was used to model baseband effects of a power amplifier excited with a single-channel WCDMA signal. A static nonlinear function (an odd-order polynomial with complex coefficients) in the first slice of the model captured the nonlinearity of the amplifier at the carrier frequency. Extraction of the coefficients were done by fitting to AM-AM and AM-PM responses as conventionally

done. Another static nonlinear function (an even-order polynomial with complex coefficients), a baseband filter in the frequency domain and an ideal mixer in the second slice of the model captured baseband effects of the amplifier. A complex-envelope signal measured by a vector signal analyzer was used to extract the baseband filter. This was a new attempt and saved a lot of effort required if we would have used other measurement technique as two-dimensional two-tone IM3 measurement. The problem with the extraction was that the shape of the extracted baseband filter was not smooth so the extracted model was input-dependent. This was originated from direct computation of the baseband filter using a complex envelope. This problem was solved by using another type of simple measurement to extract the baseband filter later when a multi-slice model was used to capture baseband effects of a multichannel power amplifier.

A multichannel envelope transient (ET) analysis was developed for multichannel applications with enhanced computational efficiency. Compared to the case of a single ET analysis, the enhanced computational efficiency was originated from separation of channels. The multichannel ET analysis was able to capture arbitrary baseband effects by using the constituent equations of the linear resistor, inductor and capacitor. This clarified the ambiguity of capturing baseband memory that was previously reported in [5]–[10]. The multichannel ET analysis could be used along with a sequence of HB analyses in circuit design. By comparing results of the two analyses, it would be found how much baseband effects contribute to the fundamental channels. To find out which component would contribute the most, the derivative of a suspected component could be turned off and then simulation should be conducted. If there were a lot of baseband effects before turning off the derivative and the baseband effects were reduced after deactivating the derivative, then the value of the component would need to be changed. The multichannel ET analysis was implemented in MATLAB. It was tested with a simple amplifier model and worked very well. The implemented analysis was used to model baseband effects of a multichannel power amplifier.

The multi-slice model previously used for modeling of a single-channel power amplifier was modified to capture baseband effects of a multichannel power amplifier excited with a two-channel WCDMA signal. The first slice of the modified model

was the same as the Wiener-Hammerstein model and captured nonlinear RF effects. This slice was extracted by fitting to two-dimensional single-tone measurements obtained using a network analyzer. The second slice of the model captured nonlinear baseband effects. Only single-channel measurement was previously used to model a baseband filter of the second slice and this resulted in a non-smooth baseband filter. This problem was solved by additionally using two-tone IM3 amplitude measurements for extraction of a baseband filter. The extracted baseband filter was smooth and the extracted model was no more input-dependent. Modeled output was compared with measurements and asymmetric spectral regrowth due to baseband effects of the amplifier was modeled very well. In the extraction, used were various measurements: single-tone; two-tone IM3 amplitude; and single-channel. However all of these measurements were easy and simple to obtain compared to two-dimensional two-tone IM3 measurement in which we must obtain relative-phase information of IM3 to model a baseband filter. This was the first time that a behavioral model was reported to capture baseband effects of an RF communication system excited with a multichannel digitally-modulated signal. The systematical extraction of a multi-slice model to capture baseband effects was an original contribution.

The baseband filter of the extracted model was synthesized into a circuit-level model. The synthesized model was used in the multichannel ET analysis implemented in MATLAB. Simulation results were compared and agreed well with measurements. Also the extracted multi-slice model was used in transient simulation. An example of the single-channel WCDMA case was presented to prove the possibility of applying transient scheme to simulation of an RF system excited with a digitally-modulated signal. This was done by significantly reducing the carrier frequency of the excitation. According to the example shown in Section 5.5, the original carrier frequency was 2.4 GHz and the new carrier frequency was 20 MHz. This was a reduction by a factor of 120. Reducing the carrier frequency provided enhanced computational efficiency and made it possible to simulate an RF system excited by a digitally-modulated signal in the time domain. This provided a new concept in RF system simulation. The simulation result agreed with a measurement very well. One of the advantages in using multi-slice models in transient simulation is that there is no restriction to

the drive signal. Thus excitation could be single tone, multi-tone, CDMA, chirp and noise signals. This would be very useful, for example, when conducting bit-error-rate simulation of an RF communication system. Using a multi-slice model in multichannel ET and transient analyses demonstrated compatibility of the model with established circuit simulators so one-time modeling of an RF communication system using a multi-slice model could provide a general model for various simulators.

## 6.2 Suggestions for Future Work

Circuit-level modeling is likely to be more accurate compared to system-level modeling; even so, system-level modeling provides more advantages in large system simulations in terms of computational efficiency. Thus, modeling accuracy and computational efficiency are tradeoffs between the two modeling methods. If we accept a hybrid strategy, we can make the best out of the tradeoffs. For example, circuit-level modeling is applied to critical parts of a system such as a power amplifier and the rest of the system is modeled in system-level. For the circuit level models, the multichannel ET analysis can be used. In this way, we can achieve optimum modeling accuracy and computational efficiency together. Using this method it will be useful to relate distortion caused by baseband effects to bit error rate of a communication system.

Regarding multi-slice modeling, transient simulation of the extracted model with a multichannel digitally-modulated signal will be the first future work. Another future work will be applying the extraction method to other amplifiers and determining if the method is universal. The model extracted as an example only covers the weak nonlinear region of an RF amplifier so a future work will be to extend the model into the strong nonlinear region. Another future work will be to make the model applicable to the case of wide channel-separation. To do this, it will be necessary to build a more robust model structure of the first slice since accuracy of capturing baseband effects greatly depends on how rigorously the first slice captures short-term memory effects. Also it will be interesting to test the model with many channels.

After having an accurate model, the model will be very useful to design predistorters [50]–[53] for linearization of RF amplifiers so designing predistorters by using multi-slice models will be another future work. Finally multi-slice models can be used in established circuit simulators but demonstrated simulations in Chapter 5 were done in MATLAB so implementing the models into commercial circuit simulators can be a future work.

## Bibliography

- [1] K. M. Gharaibeh and M. B. Steer, “Characterization of cross modulation in multichannel amplifiers using a statistically based behavioral modeling technique,” *IEEE Trans. Microwave Theory Tech.*, Vol. 51, No. 12, Dec. 2003, pp. 2434–2444.
- [2] K. Kundert, “Introduction to RF simulation and its application,” *IEEE J. Solid-State Circuits*, Sept. 1999, pp. 1298–1319.
- [3] K. Kundert, J. K. White and A. Sangiovanni-Vincentelli, “An envelope-following method for the efficient transient simulation of switching power and filter circuits,” in *Proc. Int. Conf. Computer Aided Design*, Nov. 1988, pp. 446–449.
- [4] A. Brambilla and P. Maffezzoni, “Envelope following method for the transient analysis of electrical circuits,” *IEEE Trans. Circuits Syst. I*, Jul. 2000, pp. 999–1008.
- [5] E. Ngoya, J. Sombrin and J Rousset, “Simulation des circuits et systèmes: méthodes actuelles et tendances,” in *Séminaires Antennes Actives et MMIC*, Arles, France, April 1994, pp. 171–176.
- [6] E. Ngoya and R. Larchevèque, “Envelop transient analysis: a new method for the transient and steady state analysis of microwave communication circuits and systems,” in *IEEE MTT-S Int. Microwave Symp. Dig.*, June 1996, pp. 1365–1368.
- [7] “Method for simulating a circuit,” US patent #5588142, Hewlett-Packard, Palo

- Alto, Calif., Application Filed: May 12, 1995, Inventor: D. Sharrit, Santa Rosa, Calif.
- [8] ADS Circuit Simulation Manual, Agilent Technology, Palo Alto, California, U.S.A., Chapter 16.
  - [9] V. Rizzoli, A. Neri, F. Mastri and A. Lipparini, "Modulation-oriented harmonic balance based on Krylov-subspace methods," in *IEEE MTT-S Int. Microwave Symp. Dig.*, June 1999, pp 771–774.
  - [10] J. Pedro and N. Carvalho, "Simulation of RF circuits driven by modulated signals without bandwidth constraints," in *IEEE MTT-S Int. Microwave Symp. Dig.*, June 2002, pp. 2173–2176.
  - [11] A. Walker, M. Steer, K. Gard and K. M. Gharaibeh, "Multi-slice behavioral model of RF systems and devices," *IEEE Radio and Wireless Conf.*, Sep. 2004, pp. 71–74.
  - [12] M. Nakhla and J. Vlach, "A piecewise harmonic balance technique for determination of periodic response of nonlinear systems," *IEEE Trans. Circuits Syst.*, Vol. 23, Feb. 1976, pp. 85–91.
  - [13] K. Kundert, J. K. White and A. Sangiovanni-Vincentelli, *Steady-State Methods for Simulating Analog and Microwave Circuits*, Kluwer, 1990.
  - [14] J. Sevic, K. Burger and M. Steer, "A novel envelope-termination load-pull method for ACPR optimization of RF/microwave power amplifiers," in *IEEE MTT-S Int. Microwave Symp. Dig.*, Vol. 2, June 1998, pp. 723–726.
  - [15] J. Vuolevi, T. Rahkonen and J. Manninen, "Measurement technique for characterizing memory effects in RF power amplifiers," *IEEE Trans. Microwave Theory Tech.*, Vol. 49, Aug. 2001, pp. 1383–1389.
  - [16] N. Carvalho and J. Pedro, "A comprehensive explanation of distortion sideband asymmetries," *IEEE Trans. Microwave Theory Tech.*, Vol. 50, No. 9, Sept. 2002, pp. 2090–2101.

- [17] N. Suematsu, Y. Iyama and O. Ishida, "Transfer characteristic of IM3 relative phase for a GaAs FET amplifier," *IEEE Trans. Microwave Theory Tech.*, Vol. 45, No. 12, Dec. 1997, pp. 2509–2512.
- [18] J. Brinkhoff and A. Parker, "Effect of Baseband Impedance on FET Intermodulation," *IEEE Trans. Microwave Theory Tech.*, Vol. 51, March 2003, pp. 1045–1051.
- [19] K. Remley, D. Williams, D. Schreurs and J. Wood, "Simplifying and interpreting two-tone measurements," *IEEE Trans. Microwave Theory Tech.*, Vol. 52, No. 11, Nov. 2004, pp. 2576–2584.
- [20] Y. Yang, J. Yi, J. Nam, B. Kim and M. Park, "Measurement of two-tone transfer characteristics of high-power amplifier," *IEEE Trans. Microwave Theory Tech.*, Vol. 49, No. 3, Mar. 2001, pp. 568–571.
- [21] C. Clark, C. Silva, A. Moulthrop and M. Muha, "Power-amplifier characterization using a two-tone measurement technique," *IEEE Trans. Microwave Theory Tech.*, Vol. 50, No. 6, June 2002, pp. 1590–1602.
- [22] D. Williams, J. Leckey and P. Tasker, "A study of the effect of envelope impedance on intermodulation asymmetry using a two-tone time domain measurement system," in *IEEE MTT-S Int. Microwave Symp. Dig.*, June 2002, pp. 1841–1844.
- [23] P. Asbeck, H. Kobayashi, M. Iwamoto, G. Hanington, S. Nam and L. Larson, "Augmented behavioral characterization for modeling the nonlinear response of power amplifiers," in *IEEE MTT-S Int. Microwave Symp. Dig.*, June 2002, pp. 135–138.
- [24] T. Gho and R. Pollard, "Predicting CDMA spectral regrowth using a general statistical behavioral model for power amplifiers with memory effects," in *Proc. Int. Symp. circuits Syst.*, May 2003, pp. II-248–II-251.

- [25] H. Ku, M. Mckinley and J. Kenney, "Extraction of accurate behavioral models for power amplifiers with memory effects using two-tone measurements," in *IEEE MTT-S Int. Microwave Symp. Dig.*, June 2002, pp. 139–142.
- [26] A. Soury, E. Ngoya and J. Nebus, "A new behavioral model taking into account nonlinear memory effects and transient behaviors in wideband SSPAs," in *IEEE MTT-S Int. Microwave Symp. Dig.*, June 2002, pp. 853–856.
- [27] N. Gallou, E. Ngoya, H. Buret, D. Barataud and J. Nebus, "An Improved behavioral modeling technique for high power amplifiers with memory," in *2001 IEEE MTT-S Int. Microwave Symp. Dig.*, May 2001, pp. 983–986.
- [28] K. Gard, H. Gutierrez and M. Steer, "Characterization of spectral regrowth in microwave amplifiers based on the nonlinear transformation of a complex Gaussian process," *IEEE Trans. Microwave Theory and Techn.*, July 1999, pp. 1059–1069.
- [29] J. Kim and K. Konstantinou, "Digital predistortion of wideband signals based on power amplifier model with memory," *Electron. Lett.*, Vol. 37, No. 23, Nov. 2001, pp. 1417–1418.
- [30] M. Nizamuddin, P. Balister, W. Tranter and J. Reed, "Nonlinear tapped delay line digital predistorter for power amplifiers with memory," in *IEEE Wireless Comm. Networking Conf.*, Vol. 1, Mar. 2003, pp. 607–611.
- [31] H. Ku and J. Kenney, "Behavioral modeling of nonlinear RF power amplifiers considering memory effects," *IEEE Trans. Microwave Theory Tech.*, Vol. 51, No. 12, Dec. 2003, pp. 2495–2504.
- [32] L. Ding, G. Zhou, D. Morgan, Z. Ma, J. Kenny, J. Kim and C. Giardina, "Memory polynomial predistorter based on the indirect learning architecture," in *Proc. IEEE Global Telecomm. Conf.*, Taipei, Taiwan, R.O.C., Nov. 2002, pp. 967–971.
- [33] D. Etter and Y. Cheng, "System modeling using an adaptive delay filter," *IEEE Trans. Circuits Syst.*, Vol. CAS-34, July 1987, pp. 770–774.

- [34] H. Ku, M McKinley and J. Kenney, “Quantifying memory effects in RF power amplifiers,” *IEEE Trnas. Microwave Theory Tech.*, Vol. 50, Dec. 2002, pp. 2843–2849.
- [35] Y. Cheng and D. Etter, “Analysis of an adaptive technique for modeling sparse systems,” *IEEE Trans. Acoust., Speech, Signal Processing*, Vol. 37, No. 2, Feb. 1989, pp. 254–264.
- [36] M. C. Jeruchim, P. Balaban and K. S. Shanmugan, *Simulation of Communication systems*, Kluwer, 2nd Edition, 2000
- [37] A. Sano and L. Sun, “Identification of Hammerstein-Wiener system with application to compensation for nonlinear distortion,” in *Proc. IEEE SICE Annual Conf.*, Vol. 3, Aug. 2002, pp. 1521–1526.
- [38] P. Crama and Y. Rolain, “Broad-band measurement and identification of a Wiener-Hammerstein model for an RF amplifier,” in *IEEE ARFTG Conf. Dig.*, Dec. 2002, pp. 49–57.
- [39] D. Nešić, “Observability for simple Wiener and simple Wiener-Hammerstein systems,” in *Proc. IEEE American Cotrol Conf.*, Vol. 4, June 1998, pp. 2349–2353.
- [40] C. Evans and D. Rees, “Nonlinear distortions and multisine signals Part I: Measuring the best linear approximation,” in *Proc. IEEE Instrum. Measure. Tech. Conf.*, Vol.2, May 1999, pp. 1038–1046.
- [41] J. Roychowdhury, “Analyzing circuits with widely separated time scale using numerical PDE methods,” *IEEE Trans. Circuits Syst. I*, Vol. 48, No. 5, May 2001, pp. 578–594.
- [42] N. Carvalho, J. Pedro, W. Jang and M. Steer, “Simulation of nonlinear RF circuits driven by multi-carrier modulated signals,” in *IEEE MTT-S Int. Microwave Symp. Dig.*, June 2005, pp. 801–804.

- [43] N. Carvalho, J. Pedro, W. Jang and M. Steer, “Nonlinear RF circuit and systems simulation when driven by several modulated signals,” *IEEE Trans. Microwave Theory Techn.*, Vol. 54, No. 2, Feb. 2006, pp. 572–579.
- [44] S. Sancho and A. Suárez, “Efficient analysis of phase-locked loops through a novel time-frequency approach, based on two envelope transient formulations,” in *IEEE MTT-S Int. Microwave Symp. Dig.*, June 2003, pp. 2153–2156.
- [45] E. de Cos, A. Suárez and S. Sancho, “Envelope transient analysis of self-oscillating mixers,” *IEEE Trnas. Microwave Theory Tech.*, Vol. 52, No. 4, April 2004, pp. 1090–1100.
- [46] S. Sancho, A. Suárez and J. Chuan, “General envelope-transient formulation of phase-locked loops using three time scales,” *IEEE Trnas. Microwave Theory Tech.*, Vol. 52, No. 4, April 2004, pp. 1310–1320.
- [47] N. Carvalho, J. Pedro, W. Jang and M. Steer, “Nonlinear simulation of mixers for assessing system-level performance,” *Int. J. RF Microwave CAE*, Vol. 15, No. 4, July 2005, pp. 350–361.
- [48] W. Jang, A. Walker, K. Gard and M. Steer, “Capturing asymmetrical spectral regrowth in RF systems using a multi-slice behavioral model and enhanced envelop transient analysis,” *Int. J. RF Microwave CAE*, In press.
- [49] B. Baytekin and R. Meyer, “Analysis and simulation of spectral regrowth in radio frequency power amplifiers,” *IEEE J. Solid-State Circuits*, Vol. 40, No. 2, Feb. 2005, pp. 370–381.
- [50] H. Qian and G. Zhou, “A neural network predistorters for nonlinear power amplifier with memory,” in *Proc. IEEE Digital Signal Processing Workshop*, Oct. 2002, pp. 312–316.
- [51] W. Bösch and G. Gatti, “Measurement and simulation of memory effects in predistortion linearizers,” *IEEE Trnas. Microwave Theory Tech.*, Vol. 37, No. 12, Dec. 1989, pp. 1885–1890.

- [52] Y. Ding and A. Sano, "Time-domain adaptive predistortion for nonlinear amplifiers," in *IEEE Int. Conf. Acoust., Speech, Signal Processing*, Vol. 3, May 2004, pp. II-865–II-868.
- [53] Y. Ding, H. Ohmori and A. Sano, "Adaptive predistortion for high power amplifier with linear dynamics," in *IEEE Midwest Symp. Circuits Syst.*, Vol. 3, July 2004, pp. III-121–III-124.

# Appendices

# Appendix A

## MATLAB Code of Multichannel

### Envelope Transient

```
%*****  
% This is a main file that simulate a circuit in multi-envelope  
% transient  
%*****  
  
clear all  
warning off;  
disp(' ');  
disp(' ');  
tt=cputime;  
  
% User inputs  
% Fundamental frequencies (Hz). f1 must be smaller than f2.  
f1 = 2E9;  
f2=2.5e9;  
  
% Maximum order of nonlinearity  
order_nonlin=3;  
  
oversample_exp=1;
```

```

% Length of a complex envelope
input_len=2000;

% Counters
cnt_fail=0;
notacc_cnt=0;

% "gen_freq_indx_2ch" is a function that generates frequency indices
% of two carriers for a given order of nonlinearity.
freq_indx=gen_freq_indx_2ch(order_nonlin);

no_of_freqs=length(freq_indx);

% Values of circuit elements in ohm, farad and henry.
R = 50;
C1 = 1e-12;
C2 = 1e-6;
L = 1e-8;

% Assign this value same as a sample time step in seconds.
time_h=1/(3.84e6*4);

% Initialize variables dependent on frequencies.
Y_C1=zeros(no_of_freqs,1); % Admittance of C1
Y_C2=zeros(no_of_freqs,1); % Admittance of C1
Z_L=zeros(no_of_freqs,1); % Impedance of L
Vd_array=zeros(no_of_freqs,1); % Drain voltages
IL=zeros(no_of_freqs,1); % Currents through the inductor
Vout=zeros(no_of_freqs,1); % Voltage at the output
V2_init=zeros(no_of_freqs,1); % Initial value of linear voltages

% Assign DC drain voltage (V) (supply voltage)
Vd_array(1)=5;

% Initial value of linear voltages is used to compute derivatives
% at the first sample time.
V2_init(1)=Vd_array(1);

% Fundamental frequencies in rads/sec.
w1 = 2*pi*f1;
w2 = 2*pi*f2;

```

```

% Calculate admittances and impedances at all frequencies.
for a = 1:no_of_freqs
    omega = w1*freq_indx(a,1)+w2*freq_indx(a,2);
    Y_C1(a) = j*omega*C1;
    Y_C2(a) = j*omega*C2;
    Z_L(a) = j*omega*L;

% Used to remove baseband(2nd intermod near DC) and 3rd intermod near
% fundamentals.
    %if(a==6|a==10|a==12)
    %   Y_C1(a)=0;
    %   Y_C2(a)=0;
    %   Z_L(a)=0;
    %end
end

% Input of WCDMA signal
load in_2p4G_n10
input=Y(1:input_len)/3;
save input input

% Linear current at the present time step and the prior time step
I2_array_hist = [zeros(no_of_freqs,1) ones(no_of_freqs,1)*1E-6];

% Harmonic balance simulations start here. This loop repeats at every
% time step.
for time_indx=1:length(input)
    s=sprintf('Time index = %0.4g', time_indx);
    disp(s);

% Initialize some arrays and variables.
    V1_array = zeros(no_of_freqs,1);
    V2_array = zeros(no_of_freqs,1);
    V2_array_old=zeros(no_of_freqs,1);
    Err = zeros(no_of_freqs,1);
    J = zeros(no_of_freqs,no_of_freqs);

% Initialize the linear current here.
    if time_indx==1 | fail_flag
        I2_array=I2_array_hist(:,2);
    else

```

```

%Initial value from the derivative by backward Euler.
    I2_array=2.*I2_array_hist(:,2)-I2_array_hist(:,1);
end
I3_array_time = [];
Vfinal_array = zeros(no_of_freqs,1);
converged = 0;

% More user inputs
% These are the final input signal levels you desire.
    Vfinal_array(1) = 0.55; %gate bias voltage
    Vfinal_array(2) = input(time_indx); % input at lower channel
    Vfinal_array(3) = input(time_indx); % input at upper channel

%Initial step size that simulator uses to step the signal levels.
%The simulator will set this automatically anyway.
    step_size = 1.0;
    tttt = cputime;

%Now we do the progressive loop that progressively increases
%the power of the harmonics.
    error_margin = 1E-4;

%~_old variables are needed for source stepping.
%They always store converged values.
    V1_array_old = V1_array;
    I2_array_old1 = I2_array;
    total_iterations = 0;
    flag2 = 1;
    percentage_old = 0;
    s = '';
    fail_flag = 0;
    step_size_old = step_size;
    while(flag2 == 1)
        V1_array = V1_array + Vfinal_array*step_size;
        x1 = sum(abs(V1_array));
        x2 = sum(abs(Vfinal_array));
        percentage = x1/x2*100;
        if(percentage >= 100)
            V1_array = Vfinal_array;
            flag2 = 0;
            percentage = 100;
        end
    end

```

```

[V1_array_time] = phasor_to_time(V1_array,freq_indx,f1,f2,...
    oversample_exp);
harmonic_balance_circuit1;
total_iterations = total_iterations + count;
if(converged ~= 1)
    V1_array = V1_array_old;
    I2_array = I2_array_old1;
    step_size = 0.5*step_size;
    I2_array=I2_array*step_size;
    if(step_size < 1E-5)
        fail_flag = 1;
        break
    end
    flag2 = 1;
else
    step_size = step_size*1.5;
    V1_array_old = V1_array;
    I2_array_old1 = I2_array;
    I2_array=I2_array*step_size;
end
if(converged)
    s = sprintf('iterations=%3i  time=%5.2f...
        step_size=%0.4e  percentage=%7.3f  convergence: PASS...
        err_sum=%4.3i', count, cpu_time, step_size_old,...
        percentage, err_sum);
    percentage_old = percentage;
else
    s = sprintf('iterations=%3i  time=%5.2f  step_size=%0.4e...
        percentage=%7.3f  convergence: FAIL err_sum=%0.3i',...
        count, cpu_time, step_size_old, percentage_old,...
        err_sum);
end
disp(s);
step_size_old = step_size;
end

if(fail_flag)
    disp(' ');
    disp('Simulation completely failed and was aborted...');
    disp('Increasing the # of harmonics may solve the problem.');
```

```

        fail_indx(cnt_fail,2)=percentage_old;
        fail_indx(cnt_fail,3)=err_sum;
    else
        I2_array=I2_array_old1;
        error_margin = 1E-11;
        notacc_flg=0;
        harmonic_balance_circuit1;
        if(notacc_flg)
            notacc_cnt=notacc_cnt+1;
            notacc(notacc_cnt,1)=time_indx;
            notacc(notacc_cnt,2)=percentage_old;
            notacc(notacc_cnt,3)=err_sum_old;
            I2_fail(:,notacc_cnt)=I2_array;
        end
    %This final run cleans up the results to relatively accurate numbers.

        total_iterations = total_iterations + count;
        disp(' ');
        s = sprintf('err_sum = %0.16e   Sum of currents = %0.16e',...
            err_sum_old,(sum(abs(I2_array))+sum(abs(I3_array))));
        disp(s);
        s = sprintf('Total expired system time %f secs',cputime-tttt);
        disp(s);
        s = sprintf('Total number of iterations is %i',...
            total_iterations);
        disp(s);
    end
    v2ET(:,time_indx)=V2_array_old;
    if time_indx==1
        Vout=(Y_C2.*V2_array_old+constC2*(V2_array_old-V2_init))./...
            (1/R+Y_C2+constC2);
    else
        Vout=(Y_C2.*V2_array_old+constC2*(V2_array_old-...
            v2ET(:,time_indx-1)+voET(:,time_indx-1)))./...
            (1/R+Y_C2+constC2);
    end
    end
    voET(:,time_indx)=Vout;
    IL=(Vd_array-V2_array_old+constL*IL)./(Z_L+constL);
    %IL(1)=0;    %for w/o derivatives only
    %IL(6)=0;    %for w/o 2nd(near baseband) only
    %IL(10)=0;   %for w/o 3rd(near fundamental) only
    %IL(12)=0;   %for w/o 3rd(near fundamental) only

```

```

    if time_indx==1
        I2_array_hist(:,2)=I2_array;
    else
        I2_array_hist(:,1)=I2_array_hist(:,2);
        I2_array_hist(:,2)=I2_array;
    end
    if fail_flag
        %disp('aaa ');
        I2_array_hist = [I2_array_hist(:,1) I2_array_hist(:,1)];
    end
    s=sprintf('Total elapsed time = %f secs', cputime-tt);
    disp(s)
    disp(' ')
    disp(' ')
end save voET_WCDMA2_2000 voET

%*****
% File name: "gen_freq_indx_2ch.m"
% This file generates indices of intermodulation and harmonic
% frequencies for 2 channels.
%*****
cnt=0;
pnt=0;
%Initial matrix of frequency indices.
freq_indices=zeros(sum(cumsum(ones(order_nonlin,1)*2))+1,2);

for ord=0:order_nonlin
    for inn=0:ord
        cnt=cnt+1;
        freq_indices(cnt,1)=inn;
        freq_indices(cnt,2)=ord-inn;
    end
end

for row_indx=1:cnt
    pnt=pnt+1;
    if freq_indices(row_indx,1)==0 | freq_indices(row_indx,2)==0
        freq_indx(pnt,:)=freq_indices(row_indx,:);
    elseif freq_indices(row_indx,1)==freq_indices(row_indx,2)
        freq_indx(pnt,:)=freq_indices(row_indx,:);
        pnt=pnt+1;
        freq_indx(pnt,1)=-freq_indices(row_indx,1);
    end
end

```

```

        freq_indx(pnt,2)=freq_indices(row_indx,2);
    elseif freq_indices(row_indx,1) < freq_indices(row_indx,2)
        freq_indx(pnt,:)=freq_indices(row_indx,:);
        pnt=pnt+1;
        freq_indx(pnt,1)=-freq_indices(row_indx,1);
        freq_indx(pnt,2)=freq_indices(row_indx,2);
    else
        freq_indx(pnt,:)=freq_indices(row_indx,:);
        pnt=pnt+1;
        freq_indx(pnt,1)=freq_indices(row_indx,1);
        freq_indx(pnt,2)=-freq_indices(row_indx,2);
    end
end
end

%*****
% File name: "harmonic_balance_circuit1.m"
% This file computes Jacobian and iterates for solutions.
%*****
flag = 0;
count = 0;
cpu_time = cputime;
dither_factor = 0.001;
calculate_error_harm; alpha = 1;

%I2_array_old2 is needed for Newton iteration.
I2_array_old2 = I2_array;
Err_old = Err; converged = 0;
err_sum_old = sum(abs(Err));
success=1;
while(~flag)
    count = count + 1;
    if success==1
% A loop for computing Jacobian. J=d(Error)/d(I2).
        for a = 1:no_of_freqs
            delta_x = I2_array(a)*dither_factor;
%we change the independent variables.
            I2_array(a) = I2_array(a)+delta_x;
%dithering each frequency component of I2_array.
%Here we are saying delta_x = V2_new - V2_old;
            calculate_error_harm;
%we now have calculated a new f2 (dependent variable)
%We compute the change in error due to this input variable we varied.

```

```

        delta_y = Err-Err_old;
%Here we are saying delta_y = Err_new - Err_old.
        J(:,a) = delta_y./delta_x;
%The derivative are then placed in the jacobian matrix.
        I2_array = I2_array_old2;
    end
end
I2_array = I2_array_old2 - inv(J)*Err_old*alpha;
calculate_error_harm;
err_sum = sum(abs(Err));
success = 0;

% When new error sum is larger than old error sum,
% reducing 'alpha' gives another I2 value for better convergence.
if(err_sum < err_sum_old)%+1E-12)
    alpha = alpha*1.1;
    if(alpha > 1)
        alpha = 0.95;
    end
    Err_old = Err;
    err_sum_old = err_sum;
    I2_array_old2 = I2_array;
    V2_array_old=V2_array;
    success = 1;
    if(count==1000)
        converged = 0;
        notacc_flg=1;
        break;
    end
else
    alpha = alpha*0.5;
    if(alpha > 1)
        alpha = alpha*0.5;
    end
    I2_array = I2_array_old2;
    success = 0;
    if(alpha < 1E-5 | count==1000)
        converged = 0;
        notacc_flg=1;
        break;
    end
end
end

```

```

        if(err_sum < error_margin)
            converged = 1;
            break;
        end
    end
end
cpu_time = cputime - cpu_time;

%*****
% File name: "calculate_error_harm.m"
% This file computes the magnitude of the error at every iteration.
%*****
constL=L/time_h; constC1=C1/time_h; constC2=C2/time_h;
%constL=0; %without derivatives
%constC1=0;
%constC2=0;
if time_indx==1
    V2_array=(Vd_array+constL*IL+(Z_L+constL).*(constC1*V2_init+...
        constC2*V2_init./(1+R*(Y_C2+constC2))-I2_array))./...
        (1+(Z_L+constL).*(Y_C1+constC1+(Y_C2+constC2))./...
        (1+R*(Y_C2+constC2))));
else
    V2_array=(Vd_array+constL*IL+(Z_L+constL).*...
        (constC1*v2ET(:,time_indx-1)+constC2*...
        (v2ET(:,time_indx-1)-voET(:,time_indx-1))./...
        (1+R*(Y_C2+constC2))-I2_array))./(1+(Z_L+constL).*...
        (Y_C1+constC1+(Y_C2+constC2))./(1+R*(Y_C2+constC2))));
end

[V2_array_time]=...
    phasor_to_time(V2_array,freq_indx,f1,f2,oversample_exp);
[I3_array_time]=ekv(V2_array_time,V1_array_time);
I3_array=...
    time_to_phasor(I3_array_time,freq_indx,f1,f2,oversample_exp);
Err=I3_array - I2_array;

%*****
% File name: "phasor_to_time.m"
% This file generates time domain signal from frequency phasors
%*****
%The frequency array must include DC and the fundamental.
function [signal_array] =...
phasor_to_time(frequency_array,freq_indx,f1,f2,oversample_exp)

```

```

%we need to pick as sampling time that is high enough to prevent
%aliasing... I will oversample. This helps prevent aliasing.
%If there is a case where the non-linear device is saturating or
%whatever such that there are really lots of high frequency harmonics,
%one will want to set this oversample rate higher to accomodate or set
%the number of harmonics higher. This is set by setting oversample_exp
%(oversample exponent) thus if oversample_exp = 5, we will be
%oversampling by a factor of  $2^5 = 32$ . Additionally, we want to include
%enough samples to get one full cycle of the fundamental. Any more
%than this will be redundant information.

%The bigger the oversample factor, the less aliasing that will
%occur, but the more time to computer stuff.
%make sure this is an even number. Also, no smaller than 2.
oversample_factor = 2^(oversample_exp);

L = length(frequency_array);
if(L < 2)
    error('There must be at least two frequencies in the frequency_array');
end

f1_indx=freq_indx(:,1);
f2_indx=freq_indx(:,2);

%Remember the first element of 'f~_indx' is DC.
f_lowest=min((f1_indx(2:L)*f1+f2_indx(2:L)*f2)./f1);
f_highest=max((f1_indx*f1+f2_indx*f2)./f1);
f_hl_ratio=f_highest/f_lowest;

%period of the fundamental frequency which is normalized to 1.
T_fund = 1;

%Sample period.
Ts = 1/(f_hl_ratio*2*oversample_factor);

%This won't quite be a period of time.. One sample less.
no_of_samples = round(T_fund/Ts);

signal_array = zeros(no_of_samples,1);

% create signal array

```

```

%This block of code is faster than using the ifft method by something
% on the order of 3.
mag_array = abs(frequency_array);
phase_array = angle(frequency_array);    %Note phase is in radians.
signal_array = zeros(no_of_samples,1);

t_array =0:1:no_of_samples-1;
t_array = t_array'*Ts;
for i = 1:L
    f = (f1_indx(i)+(f2/f1)*f2_indx(i))/f_lowest;
    mag = mag_array(i);
    phase = phase_array(i);
    signal_array = signal_array + mag*cos(2*pi*f*t_array + phase);
end

%*****
% File name: "ekv.m"
% This file computes a drain current for a given gate voltage and
% a drain voltage.
%*****
function [id] = ekv(vd,vg)
% Parameters of a transistor
type=1; l=1e-6; w=2500e-6; np=125; ns=1; cox=3.45e-3; xj=0.15e-6;
dw=0; dl=0; vto=0.7; gamma=0.7; phi=0.5; kp=150e-6; eo=200e6;
ucrit=2.3e6; theta=0; lambda=0.8; weta=0.2; leta=0.3; qo=230e-6;
lk=0.4e-6; iba=2e8; ibb=2e8; ibn=0.6; tcv=1e-3; bex=-1.5;
ucex=0.8; ibbt=9e-4; avto=0; akp=0; agamma=0; kf=0; af=1; nqs=0;
satlim=exp(4); xqc=0.4; epsilsi=104.5e-12; epsilox=34.5e-12;
q=1.602e-19; k=1.3807e-23; tref=300.15; t=300.15; vs=0; jk=1;
jkg=1;

tnom=tref;
vtt=k*t/q;
vttref=k*tref/q;
egt=1.16-0.000702*t*t/(t+1108);
egtref=1.16-0.000702*tref*tref/(tref+1108);
weff=w+dw; leff=l+dl;
vtoa=vto+avto/sqrt(np*weff*ns*leff);
kpa=kp*(1+akp/sqrt(np*weff*ns*leff));
gammaa=gamma+agamma/sqrt(np*weff*ns*leff);

cepsil=4*(22e-3).^2; ca=0.028;

```

```

xi=ca*(10*leff/lk-1);
deltavrsce=2*qo/(cox*(1+0.5*(xi+sqrt(xi.^2+cepsil))).^2);
vgprm=jkg*vg-vtoa-deltavrsce+phi+gammaa*sqrt(phi);
if vgprm>0
    vpo=vgprm-phi-gammaa*(sqrt(vgprm+(gammaa/2).^2)-gammaa/2);
else
    vpo=-phi;
end
vsprm=0.5*(vs+phi+sqrt((vs+phi).^2+16*vtt.^2));
vdprm=0.5*(jk*vd+phi+sqrt((jk*vd+phi).^2+16*vtt.^2));
gammao=gammaa-epsilsi*(leta*(sqrt(vsprm)+sqrt(vdprm))/leff-3*weta*...
    sqrt(vpo+phi)/weff)/cox;
gammapr=0.5*(gammao+sqrt(gammao.^2+0.1*vtt));
if vgprm>0
    vp=vgprm-phi-gammapr.*(sqrt(vgprm+gammapr.^2/4)-gammapr/2);
else
    vp=-phi;
end
n=1+gammaa./(2*sqrt(vp+phi+4*vtt));
arg1=(vp-vs)/vtt;
i_f=(log(1+exp(arg1/2))).^2;
vc=ucrit*ns*leff;
vdss=vc*(sqrt(0.25+vtt*sqrt(i_f)/vc)-0.5);
vdssprm=vc*(sqrt(0.25+vtt*(sqrt(i_f)-0.75*log(i_f))/vc)-0.5)+vtt*...
    (log(vc/(2*vtt))-0.6);
deltav=4*vtt*sqrt(lambda*(sqrt(i_f)-vdss/vtt)+1/64);
vds=(jk*vd-vs)/2;
vip=sqrt(vdss.^2+deltav.^2)-sqrt((vds-vdss).^2+deltav.^2);
lc=sqrt(epsilsi*xj/cox);
deltal=lambda*lc*log(1+(vds-vip)/(lc*ucrit));
lprm=ns*leff-deltal+(vds+vip)/ucrit;
lmin=ns*leff/10;
leq=0.5*(lprm+sqrt(lprm.^2+lmin.^2));
arg2=(vp-vds-vs-sqrt(vdssprm.^2+deltav.^2)+sqrt((vds-vdssprm).^2+...
    deltav.^2))/vtt;
irprm=(log(1+exp(arg2/2))).^2;
arg3=(vp-jk*vd)/vtt;
ir=(log(1+exp(arg3/2))).^2;
betao=kpa*np*weff./leq;
if type==1
    eta=0.5;
else

```

```

    eta=1/3;
end
qbo=gammaa*sqrt(phi); betaopr=betao*(1+cox*qbo/(eo*epsilsi));
nq=1+gammaa./(2*sqrt(vp+phi+1e-6)); xf=sqrt(0.25+i_f);
xr=sqrt(0.25+ir);
qd=-nq.*(4*(3*xr.^3+6*xr.^2.*xf+4*xr.*xf.^2+2*xf.^3)./(15*(xf+xr).^...
    2)-0.5);
qs=-nq.*(4*(3*xf.^3+6*xf.^2.*xr+4*xf.*xr.^2+2*xr.^3)./(15*(xf+xr).^...
    2)-0.5);
qi=qs+qd;
if vgprm>0
    qb=-gammaa.*sqrt(vp+phi+1e-6)/vtt-(nq-1).*qi./nq;
else
    qb=-vgprm/vtt;
end
qg=-qi-qb;
C_ox=cox*np*wef*ns*leff;
QI=C_ox*vtt*qi;
QB=C_ox*vtt*qb;
QD=C_ox*vtt*qd;
QS=C_ox*vtt*qs;
QG=C_ox*vtt*qg;

beta=betaopr./(1+cox*vtt*abs(qb+eta*qi)./(eo*epsilsi));
%vpprm=0.5*(vp+sqrt(vp.^2+2*vtt.^2));
%beta=betao/(1+theta*vpprm);
is=2*n.*beta*vtt.^2; ids=is.*(i_f-irprm);
vib=jk*vd-vs-2*ibn.*vdss;
if vib>0
    idb=ids.*iba.*vib.*exp(-ibb.*lc./vib)./ibb;
else
    idb=0;
end
id=ids+idb;

%*****
% File name: "time_to_phasor.m"
% This file generates frequency phasors from a time domain signal.
%*****
function [frequency_array] =...
time_to_phasor(signal_array,freq_indx,f1,f2,oversample_exp)

```

```

%Signal array is time domain row vector of the signal over one
%fundamental frequency period. no_of_freqs includes DC and the
%fundamental frequency. This number should at least be 2. The
%returned array contains the phasors of the various frequencies.
%The first element is DC, the next is fundamental phasor, the next
%is second harmonic phasor..ect. Be careful about using this function.
%You won't get the correct fourier series unless you have just the
%right number of time samples. If you generated the signal array using
%phasor_to_time, and you set no_of_freqs the same as the number of
%phasors you used at the time you made the time domain plot, you
%should get an exact representation of the fourier series.

%number of points in one fundamental cycle
no_of_samples = length(signal_array);
L=length(freq_indx);
f1_indx=freq_indx(:,1);
f2_indx=freq_indx(:,2);
f_lowest=min(f1_indx(2:L)+f2_indx(2:L)*(f2/f1));
f_highest=max(f1_indx+f2_indx*(f2/f1));
f_hl_ratio=f_highest/f_lowest;

%This rounding makes sure we get an integer.
step_size = round((no_of_samples - 1)/(f_hl_ratio*2*2^...
    (oversample_exp)));
no_of_samples = floor(no_of_samples/step_size);

sampled_signal_array = zeros(no_of_samples,1); b = 1;

for a = 1:no_of_samples
    sampled_signal_array(a) = signal_array(b);
    b = b+step_size;
end

% The DC component isn't split in two to parts like the rest
% of the dft is
f = fft(sampled_signal_array);
frequency_array = zeros(L,1);
frequency_array(1) = f(1);
for a = 1:L-1
    k=(f1_indx(a+1)+f2_indx(a+1)*f2/f1)/f_lowest;
%The factor of two is required since we are pulling off of
%one of the phasors.

```

```
        frequency_array(a+1) = 2*f(k+1);  
end  
  
%This correct for the DFT scaling.  
frequency_array = frequency_array/no_of_samples;
```

## Appendix B

# Power Amplifier Circuits Used in Section 4.5

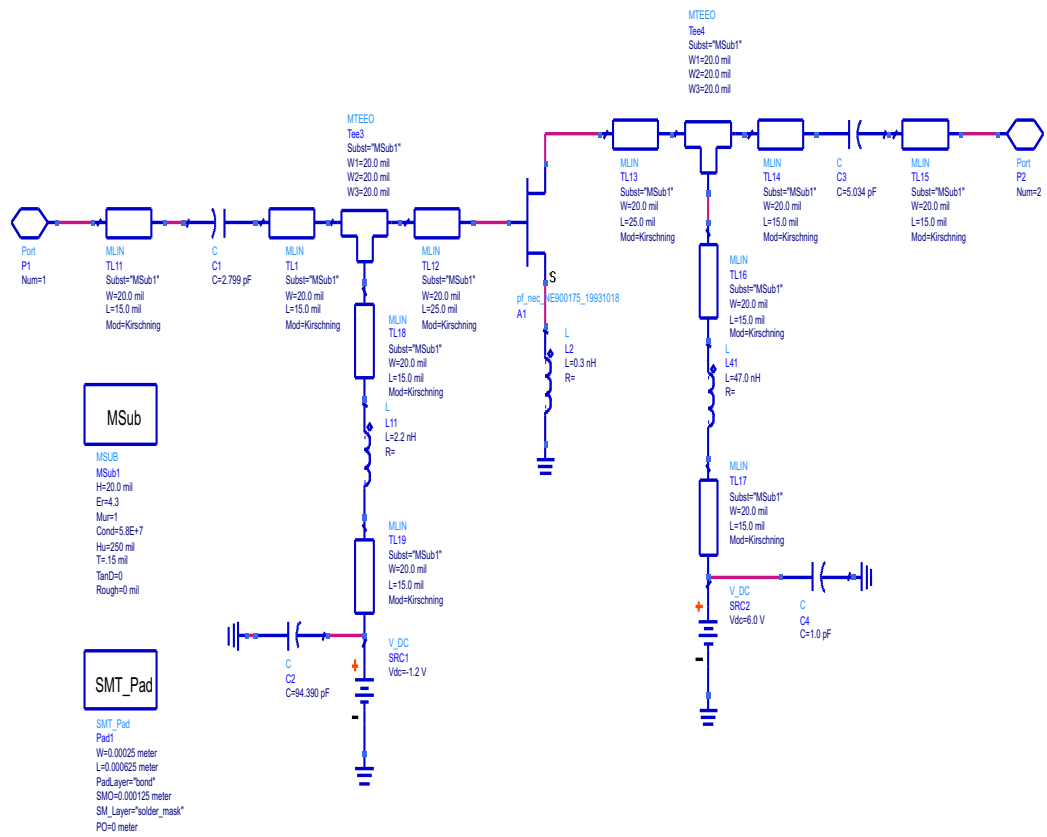


Figure B.1: The circuit of the PCS power amplifier from ADS.

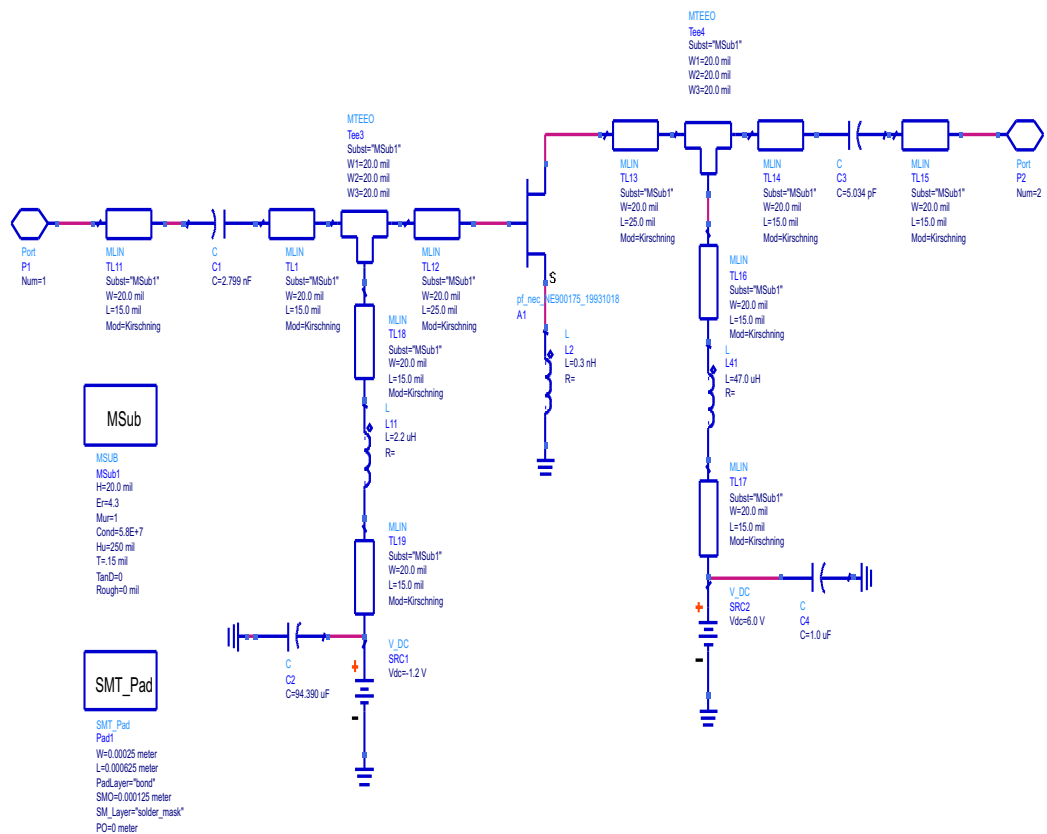


Figure B.2: The same circuit as in B.1 with modified parameters of the bias circuit elements.